# APPROVAL SHEET

**Title of Dissertation:** Adaptive Constrained Independent Vector Analysis: Application to Large-Scale fMRI Analysis

**Name of Candidate:** Suchita Bhinge
Doctor of Philosophy, 2020

**Dissertation and Abstract Approved:**

Dr. Tülay Adalı
Distinguished University Professor
Department of Computer Science and Electrical Engineering

**Date Approved:** 4/27/2020

# ABSTRACT

**Title of Dissertation:** Adaptive Constrained Independent Vector Analysis: Application to Large-Scale fMRI Analysis

Suchita Bhinge, Doctor of Philosophy, 2020

**Dissertation directed by:** Dr. Tülay Adalı, Distinguished University Professor
Department of Computer Science and
Electrical Engineering

Functional magnetic resonance imaging (fMRI) provides non-invasive indirect measures of neuronal activation in the brain. Analysis of large-scale fMRI datasets, acquired from a large pool of individuals, has become prominent in recent studies for the identification of global functional networks that summarize the population, and networks specific to individuals, groups, conditions, or modalities. Dynamic functional network connectivity (dFNC) analysis has gained popularity over recent years for extracting networks that are functionally correlated and continuously changing over the scanning period, due to their ability to identify distinct biomarkers in a variety of disorders such as schizophrenia, bipolar disorder, post-traumatic stress and in different stages of development. However, the methods used to extract dFNC patterns mostly capture the time-varying associations of the spatial networks, while assuming that the spatial network itself is stationary over the scanning period. Hence, a model that allows for the variability in both spatial and temporal domain, and jointly extracts networks specific to individuals while exploiting the dependence across a large group of individuals, provides an efficient way for analysis of fMRI data. Group independent component analysis (gICA) has been widely-used for the analysis of multi-subject fMRI data for nearly two decades, and has been applied to jointly analyze data from a large pool of subjects. However, gICA employs a significant group-level dimension reduction to estimate a common spatial subspace, which may cause loss of individual specific information making it limited in terms of preserving subject-specific information. Joint ICA, on

the other hand, assumes a common temporal domain across multiple subjects, making it a model mismatch to analysis of resting-state fMRI data.

Independent vector analysis (IVA) assumes variability in both temporal and spatial domain, and extracts subject-specific spatio-temporal patterns by jointly analyzing multi-subject fMRI data, effectively preserving subject variability in a data-driven manner. However, the performance of IVA depends on a number of key aspects of the data, namely the number of datasets, number of sources, number of samples and level of correlation across datasets. In this work we study the effect of each of these aspect, and observe that the performance of IVA degrades with increase in number of datasets and number of sources, and decrease in the level of correlation across datasets, for a fixed number of samples. In fMRI analysis, the number of samples for each subject is fixed, and the use of large number of datasets and sources is desirable, with the sources exhibiting low level of correlation across datasets. Hence, the application of IVA on large-scale fMRI data often gives undesirable results. In this work, we propose the adaptive constrained IVA (acIVA) technique that incorporates multiple reference signals into the IVA cost function and adaptively controls the effect of inaccurate and accurate references through an adaptive parameter-tuning technique. We study the performance of acIVA on high dimensional datasets, and demonstrate its superior performance in terms of its ability to meaningful patterns from large-scale fMRI datasets. We propose a sliding-window analysis technique using acIVA to extract dynamic functional network connectivity patterns that assume variability in both spatial and temporal domains. We demonstrate the significance of spatial dynamics through a classification technique, which shows an increase in prediction accuracy for spatial dynamic features, and also propose graph-theoretical metrics to quantify the variability in functional connectivity across networks and variability within each spatial network.

# Adaptive Constrained Independent Vector Analysis: Application to Large-Scale fMRI Analysis

by

Suchita Bhinge

Dissertation submitted to the Faculty of the Graduate School
of the University of Maryland in partial fulfillment
of the requirements for the degree of
Doctor of Philosophy
2020

*To my family and friends*

## ACKNOWLEDGMENTS

I would like to thank my advisor Dr. Tülay Adalı for her support, guidance and patience throughout my doctoral work. Her passion towards research, exploring new ideas and applications, gave me an opportunity to work on a number of different projects and helped me to look at problems from different angles. She has been a great mentor and helped me in developing my writing skills, presentation skills and research skills. Her encouragement on teamwork and discussions created a healthy, collaborative environment in the lab, and I am grateful to be a part of the MLSP lab.

I would like to express my gratitude to the committee members: Dr. Seung Jun Kim, Dr. Shari Waldstein, Dr. Vince D. Calhoun, Dr. Yuri Levin-Schwartz and Dr. Zois Boukouvalas, for providing insightful feedback.

I would like to thank my former and current members of the MLSP lab: Dr. Gengshen Fu, Dr. Yuri Levin-Schwartz, Dr. Zois Boukouvalas, Qunfang Long, Mohammad Abu Bak Siddique Akhonda, Ben Gabrielson and Rami Mowakeaa for providing guidance and suggestions throughout my PhD, and making this journey memorable. I would also like to thank my parents, Alka Bhinge and Vishwanath Bhinge, my brother, Akshay Bhinge, my fiancé, Suraj Vartak, and my friends who constantly supported and believed in me.

# TABLE OF CONTENTS

## LIST OF FIGURES

## LIST OF TABLES

## LIST OF ABBREVIATIONS

| | |
|---|---|
| AUD | auditory |
| ACC | anterior cingulate cortex |
| acIVA | adaptive constrained independent vector analysis |
| AG | angular gyrus |
| BOLD | blood oxygenated level dependent |
| BSS | blind source separation |
| CB | cerebellum |
| cIVA | constrained independent vector analysis |
| COBRE | Center for Biomedical Research Excellence |
| dFNC | dynamic functional network connectivity |
| dlPFC | dorsolateral prefrontal cortex |
| dmPFC | dorsal medial prefrontal cortex |
| DMN | default mode network |
| EEG | electroencephalogram |
| EBM | entropy bound minimization |
| ERBM | entropy rate bound minimization |
| fMRI | functional magnetic resonance imaging |
| FNC | functional network connectivity |
| FP | fronto-parietal |
| FRO | frontal |
| gICA | group independent component analysis |

| | |
|---|---|
| GLM | general linear model |
| HC | healthy controls |
| ICA | independent component analysis |
| ICs | independent components |
| INS | insular |
| ITC | information theoretic criteria |
| IVA | independent vector analysis |
| IVA-G | IVA with multivariate Gaussian prior |
| IVA-GGD | IVA with multivariate generalized Gaussian distribution prior |
| IVA-GL | IVA with multivariate Gaussian and Laplacian prior |
| IVA-L | IVA with multivariate Laplacian prior |
| jICA | joint ICA |
| jISI | joint inter-symbol interference |
| LTC | lateral temporal cortex |
| MCCA | multiset CCA |
| MCIC | MIND Clinical Imaging Consortium |
| mPFC | medial prefrontal cortex |
| MRN | Mind Research Network |
| PAR | parietal |
| PCA | principal component analysis |
| PCs | principal components |
| PCC | posterior cingulate cortex |
| PDF | probability density function |

| | |
|---|---|
| PPC | posterior parietal cortex |
| rst-fMRI | resting-state fMRI |
| sdFNC | spatial dynamic functional network connectivity |
| SM | sensory motor |
| SNR | signal-to-noise ratio |
| SVD | singular value decomposition |
| SZ | patients with schizophrenia |
| tdFNC | temporal dynamic functional network connectivity |
| TempP | temporal pole |
| TPJ | temporoparietal junction |
| vlPFC | ventrolateral prefrontal cortex |
| VIS | visual |

Chapter 1

# INTRODUCTION

## 1.1 Motivation

As a non-invasive technique to measure the neuronal activation in the brain, functional magnetic resonance imaging (fMRI) provides data with a high spatial resolution (typically in millimeters) and low temporal resolution (typically in seconds). FMRI detects changes in the blood oxygenation levels in certain areas of the brain when these regions are activated while performing a certain task or at rest. Functional network connectivity (FNC) analysis is a widely studied topic in fMRI analysis, which studies the connectivity between anatomically separated regions of the brain, *i.e.*, FNC identifies a network of regions that have similar activation patterns [1]. The study of differences in FNC has led to the identification of biomarkers of a number of neurological disorders such as Alzheimer's disease, post-traumatic stress disorder, bipolar disorder, autism, schizophrenia, and attention deficit hyperactivity disorder [2–6]. Joint analysis of fMRI data from a large pool of individuals has become important for identifying global functional networks that summarize the population, and networks specific to individuals, groups, conditions, or modalities. It allows for the extraction of robust features that can be used to summarize a group of disorders, and identification of networks specific to certain groups and individuals, enabling extraction of sub-group of individuals, or traits that are distinct to a certain type of disorder. In order to obtain such robust features that well describe the data, the use of methods that

preserve individual specific information, while accounting for the dependence across many individuals, is especially desirable.

A primary challenge in the analysis of FNC is the identification of separate brain regions that share a common activation pattern, *i.e.*, activated functional networks, from a large pool of individuals. A number of approaches are used for identification of brain regions, and these can be broadly classified as model-driven and data-driven techniques [7]. Model-driven techniques make use of some prior information regarding the data, such as the nature of the activation pattern or the nature of the brain regions. Although these methods are robust to noise and other artifacts, they make stronger assumptions about the data. Another class of techniques are the data-driven techniques that make weaker assumptions about the data and are more flexible in terms of estimation of the structure of the activation patterns and the brain regions. A popular type of data-driven technique for the analysis of fMRI data is independent component analysis (ICA), which is based on the assumption of statistical independence across the brain regions [8]. ICA decomposes each individual's fMRI data into a mixing matrix, whose columns correspond to the activation pattern or the time course, and a source matrix, whose rows correspond to the separated brain regions. However, the conventional ICA model can only be applied to a single subject's data.

Group ICA (gICA) is an extension of ICA to multiple subjects, which jointly analyzes multi-subject fMRI data with an assumption that these subjects share a common spatial subspace spanned by the brain regions that are similar across multiple subjects [9, 10]. Although gICA is widely-used in fMRI analysis and can be used to analyze data from a large population group, it is limited in terms of preserving subject specific information. Independent vector analysis (IVA), an extension of ICA to multiple datasets, jointly decomposes multi-subject fMRI data into subject-specific spatial maps (*i.e.* brain regions) and time courses. IVA provides a general framework for the identification of sources and

has shown better performance compared to gICA in terms of preserving individual-specific information [11–13]. However, IVA presents limitations in terms of analysis of large-scale fMRI data as the performance of IVA degrades when a higher number of subjects are decomposed jointly, for a fixed number of samples. The performance of IVA also depends on other aspects of the data, such as number of sources, and level of correlation of the sources across datasets, which has not been studied so far to the best of our knowledge.

Dynamic functional network connectivity (dFNC) analysis has emerged over the recent years due to evidence that FNC changes over the duration of the scanning period [14]. This led to the categorization of FNC analysis into stationary functional network connectivity analysis and dFNC analysis. Stationary FNC analysis groups studies that assume FNC patterns do not change over the scanning period, and measure the association between the activation patterns of different brain regions over the entire scanning period, as shown in Fig.1.1(a). This may yield an average FNC measure, limiting our understanding of the functioning of the brain. However, a number of studies have shown the presence of multiple structured patterns corresponding to different FNC in task-related and resting-state fMRI data, see *e.g.*, [15–19]. Analyzing these connectivity patterns in resting-state data has enabled the identification of distinct biomarkers in a variety of disorders such as schizophrenia [20], bipolar disorder [21], autism [22, 23], post-traumatic stress disorder [24, 25], generalized anxiety disorder [26],attention deficit hyperactivity disorder [27] and mild cognitive impairment [28]. Studies have also shown changes in functional connectivity patterns in different stages of development [29] and due to hallucinations [30]. Most dFNC analysis methods however, extract dFNC patterns with an assumption that the connectivity of the networks changes over time while the network itself is stationary, as shown in Fig.1.1(b). These methods are grouped under temporal dFNC analysis methods. However, studies have shown that changes in FNC implies changes in the spatial networks

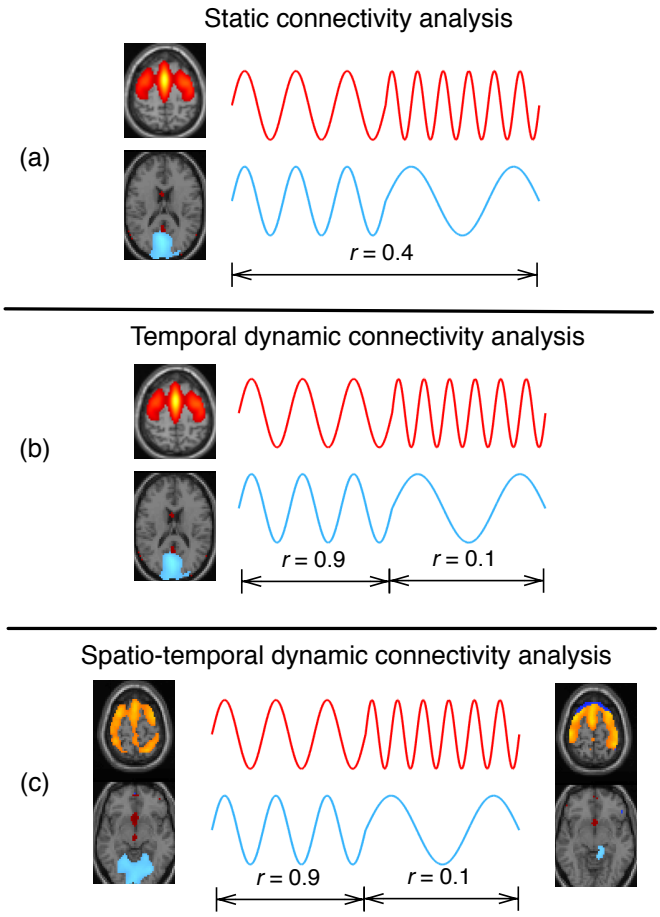


FIG. 1.1. Functional connectivity analysis studies the association among the activation pattern between different regions of the brain. (a) Static connectivity analysis assumes stationarity in both spatial and temporal domain, resulting in an average association over the scanning period. (b) Temporal dynamic connectivity analysis assumes stationarity in the spatial domain and variability in the temporal domain. (c) Spatio-temporal dynamic functional connectivity analysis assumes variability in both spatial and temporal domain enabling a better understanding on the varying functional associations.

[31–33]. Hence, a model that extracts time-varying dFNC patterns with an assumption of variability in both spatial and temporal domain is desirable for dFNC analysis, as shown in Fig.1.1(c).

Studies have shown that changes in FNC in resting-state are not random but exhibit

structured patterns that vary over time ([19, 34, 35]). This has led to the identification of the structured patterns, which are referred to as *states*, and identifying metrics such as fraction of time spend in a certain state, number of transitions from one to another, and probability of occurrence of a state within a group of subjects. Temporal dFNC analysis has identified hyperconnected or hypoconnected connectivity states associated with a number of neurological disorder such as schizophrenia, autism, post-traumatic stress disorder and Alzheimer's, and has found differences in the degree of variability of temporal FC patterns between healthy controls and patients [20, 36–39]. Although exploiting variability in the spatial domain for dFNC analysis has shown better performance in terms of classification using a model-driven analysis ([32]), which is sensitive to the networks selected, the features extracted from spatio-temporal dFNC patterns are not explored.

## 1.2 Contributions

In this dissertation, we address the challenges that we discuss above, specifically: the extraction of relevant, meaningful functional networks from large-scale fMRI data in a robust yet data-driven manner, the study of different aspects of IVA, which affect its performance in terms of estimating meaningful sources, and determination of a model for the extraction of time-varying spatio-temporal patterns from large-scale fMRI data. In order to study these challenges, we make the following contributions:

- We propose the use of prior information regarding the nature of the data in order to extract spatio-temporal patterns from large-scale fMRI data. We propose the use of a semi-blind IVA technique, that provides a desirable balance between data-driven and model-driven techniques, while benefiting from both.

- We propose the adaptive constrained IVA technique, which incorporates prior information regarding the estimated source or column of the mixing matrix, into the IVA

framework. This technique adaptively tunes the effect of the prior information on the corresponding source or the respective column of the mixing matrix. We investigate the performance of this technique using a series of simulation examples and show that the proposed technique adaptively tunes the effect of accurate and inaccurate prior information, thus significantly improving the performance of IVA.

- We study the effect of different aspects, such as number of sources, number of datasets, number of samples and level of correlation, on the performance of IVA using simulation examples. We investigate the performance of acIVA and IVA technique on high dimensional datasets through a simulation study and by applying it on a large-scale fMRI dataset. Our results indicate that the performance of acIVA is significantly better than standard IVA in terms of estimating the underlying sources from high dimensional datasets.

- We propose a technique to extract spatio-temporal dynamic patterns from fMRI data using a sliding-window acIVA framework, which assumes variability in both spatial and temporal domains. We apply this technique on fMRI data acquired from 88 healthy controls (HC) and 91 patients with schizophrenia (SZ), and estimate 17 functionally relevant components along with the time courses at different time instances.

- We analyze the variability of spatio-temporal dFNC patterns obtained using the proposed method and temporal dFNC patterns obtained using gICA. Our results show that more meaningful connections demonstrated group differences when variability in both spatial and temporal domains is considered. Our results also show higher variability among the connectivity between different networks for the SZ group, providing support for the tendency of SZs to engage more brain regions that HCs. We study the variability of spatial networks and observe a disrupted medial visual net-

work for patients with schizophrenia, along with more variability in the sensorimotor, fronto-parietal and parietal regions.

- We investigate the strength of spatial dynamic patterns through a prediction technique, where we compare the ability of temporal dynamic patterns and spatial dynamic patterns to predict if a subject is a healthy control or a patient with schizophrenia. We observe an increase sensitivity using spatial dynamic patterns, *i.e.*, spatial dynamic features are better able to identify patients with schizophrenia. We also study the structured patterns of connectivity obtained using spatial dFNC patterns and observe that patients with schizophrenia tend to stay in or switch to states corresponding to an abnormal and hyperconnected state.

## 1.3 Overview of Dissertation

The remainder of the dissertation is organized as follows.

In Chapter 2, we provide an introduction to functional magnetic resonance imaging (fMRI) data and the methods that we will use throughout this dissertation. We begin by briefly describing the acquisition of fMRI data and introduce different methods used to extract patterns from fMRI data. We then describe the general IVA model and the different types of IVA algorithms. We introduce the IVA with multivariate Laplacian sources with second-order correlation (IVA-L-SOS) algorithm, which jointly accounts for both second and higher-order statistics (SOS and HOS), followed by a discussion of a method for selecting the most consistent run using cross joint inter-symbol interference.

In Chapter 3, we study the effect of different aspects on the performance of IVA, such as number of datasets, number of sources, number of samples and level of correlation between sources across datasets. We show that the performance of IVA is affected with increase in number of datasets and sources, and decrease in the level of correlation, for a

fixed number of samples.

In Chapter 4, we describe the development of the adaptive constrained IVA (acIVA) algorithm that effectively incorporates prior information regarding the sources or the columns of the mixing matrix into the IVA cost function, by adaptively tuning the constraint parameter. We demonstrates the successful performance of acIVA over regular constrained IVA (cIVA), which makes use of a fixed constraint parameter, using simulated data. We observe that acIVA performs better than cIVA in terms of incorporating accurate and inaccurate constraints, and in terms of preserving dataset-specific information.

In Chapter 5, we discuss the application of acIVA on high dimensional datasets and study the application of acIVA and IVA on datasets with varying number of sources and varying number of datasets. We fix the number of samples and level of correlation among sources across datasets for this simulation study, as for real-world applications these aspects do not change. We apply acIVA on a large-scale fMRI data acquired from 327 healthy subjects (164 females and 163 males), and show that acIVA performs better than IVA. We also observe that acIVA is able to extract meaningful regions that share a common activation pattern.

In Chapter 6, we propose a method to extract time-varying spatio-temporal patterns from large-scale resting-state fMRI data using acIVA. The proposed implementation consists of two stages. The first stage extracts stationary representations of the resting-state networks, and in the second stage these networks are used as reference signals in a sliding-window acIVA analysis, in order to extract their time-varying representation at each time window. We propose the use of both temporal and spatial features to study dFNC and propose two graph theoretical metrics: inter-network connectivity fluctuation and component stationarity, to quantify the variability in spatial and temporal functional connectivity and spatial network variability. We also study the significance of spatial dynamic features using

a prediction technique and through analyzing the spatial dFNC states.

We conclude the dissertation with Chapter 8 and present possible directions for future research.

## Chapter 2

# BACKGROUND

This chapter provides an introduction to fMRI data and provides a brief overview of the methods applied to extract features from fMRI data. We also introduce some of the methods that we will use throughout this dissertation.

### 2.1 Introduction to fMRI data

FMRI measures the changes in the magnetic properties of the blood caused as a result of changes in the blood oxygenated level during a neuronal activation. The onset of neuronal activation is mainly followed by the brain's need for glucose that is not stored in the brain, but transported from blood. This need for glucose causes more blood to flow in the area of neuronal activation, along with oxygen. The change in the blood flow is typically localized between 2 to 3 millimeters around the neural activity. Usually the amount of oxygen brought in is more than the amount of oxygen consumed in burning glucose causing a net decrease in deoxygenated blood. Since deoxygenated blood has slightly different magnetic properties than oxygenated blood, fMRI measures neuronal activation by recording these small changes in magnetic sensitivity. The change in the magnetic signal from neuronal activity is called the haemodynamic response, which typically lasts for 10 seconds, deciding the temporal sensitivity of fMRI scanners.

Commonly used fMRI scanners have a spatial resolution of 3 millimeters and repeti-

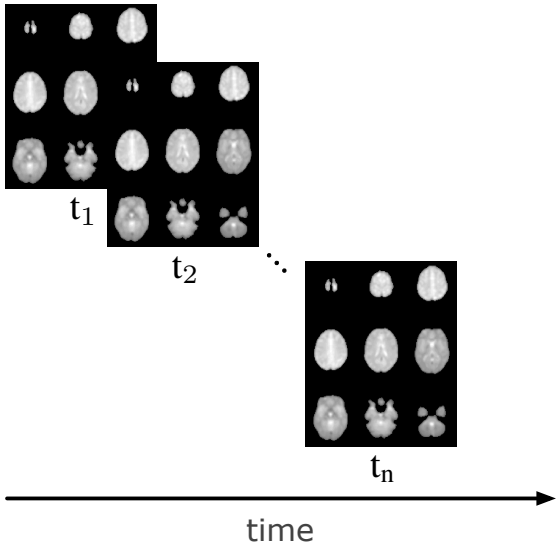


FIG. 2.1. FMRI data for each subject, data is collected as a 3D volume as a function of time. Each time point shows samples of 2D slices obtained across the transverse plane.

tion time (TR) of 1 or 2 seconds, *i.e.*, each slice along the transverse plane of the brain is scanned at a TR of 1 or 2 seconds, and a 3D volume is formed by grouping these scanned slices at a particular time instant. FMRI data is collected as a 3D volume at different time instances, as shown in Fig. 2.1. These fMRI images undergo a series of standard preprocessing steps. Images are realigned using INRIalign, and slice-timing corrected using the middle slice as the reference frame. Data are then spatially normalized into the standard Montreal Neurological Institute space, resliced to 3 mm $\times$ 3 mm $\times$ 3 mm voxels, and smoothed using a Gaussian kernel with a full-width at half-maximum of 10 mm. Masking is performed on each volume to remove the non-brain voxels and vectorized, resulting in an observation set for each subject as, $\overline{\mathbf{X}}^{[k]} \in \mathbb{R}^{T \times V},\ k = 1, \ldots, K$, where $T$ is the number of time points, $V$ is the number of voxels and $K$ is the number of subjects.

### 2.1.1 Extraction of functional networks

The haemodynamic response measured after a stimulus is applied rises at a faster rate peaking at 4-5 seconds, and then dropping at a faster rate below a standard level referred to as undershoot, before becoming stable. If the neurons keep firing, for example from a continuous stimulus, the peak stays constant for a longer duration until the neurons stay active. When a group of neurons are activated, the blood oxygenated level dependent (BOLD) response at each time instant is expected to add linearly, and can be modeled using a linear mixing model given as,

$$\overline{\mathbf{X}}^{[k]} = \overline{\mathbf{A}}^{[k]}\,\overline{\mathbf{S}}^{[k]}, k = 1, \ldots, K \tag{2.1}$$

where $\overline{\mathbf{A}}^{[k]} \in \mathbb{R}^{T\times T}$ is the mixing matrix and $\overline{\mathbf{S}}^{[k]} \in \mathbb{R}^{T\times V}$ are the latent source components/spatial maps for the $k$th dataset. The column of the mixing matrix is referred to as the time course of the corresponding spatial map. A spatial map represents a functional network that is a group of neurons that have a similar activation pattern/time course.

Brain functional networks, at a broader level, are relatively consistent across healthy subjects [40]. On the other hand, significant heterogeneity exists across different subjects within a group, modality or a condition [41]. Capturing these individual specific neural patterns can thus be used to predict individual differences [42]. Hence methods that capture the global information across subjects while preserving subject-specific information from a large-scale population are desirable in the analysis of fMRI data. FMRI analysis techniques can be broadly classified into model-driven and data-driven techniques.

**Model-driven techniques:** Model-driven methods make stronger assumptions regarding the structure of the time courses or spatial maps. These methods are robust to noise and other artifacts, however make stronger assumptions about the data. General linear model (GLM) is a type of model-driven method that specifies a user-defined mixing

matrix, commonly referred to as a design matrix, that fixes $\overline{\mathbf{A}}^{[k]}$ and estimates $\overline{\mathbf{S}}^{[k]}$ using a regression type approach. This type of approach is commonly used in task-based fMRI data, where the nature of the task paradigm or the time course is known and is used to estimate the functional networks that follow the task paradigm. Another sub-type of model-driven techniques is the region of interest (ROI)-based method that defines the structure of a spatial map using pre-defined templates of the brain regions. While GLM type methods are common to task-based fMRI data, they cannot be used to decompose resting-state fMRI data, where the true nature of the time course is not known. On the other hand, ROI-based methods make use of predefined templates of the functional networks that are defined based on the assumption that each region has a similar activation pattern. A number of atlases have been made available that divide the brain into cortical regions ranging from 70 to 333 [43–48]. These atlases are defined based on previous studies and might result in the functional connectivity dependent on the choice of ROIs.

**Data-driven techniques:** Data-driven methods are more flexible than model-driven methods since they make fewer assumptions about the nature of the solution, such as ICA, which assumes source independence, and dictionary learning (DL), which assumes sparsity. Statistical independence assumption has shown desirable performance for the analysis of fMRI data due to its ability to discover interpretable functional networks in a data-driven manner and due to minimal assumptions placed on the data [7]. We discuss the methods that exploit statistical independence and their application to fMRI data in the following sections.

### 2.1.2 Independent component analysis

The generative ICA model written as $\mathbf{x} = \mathbf{As} \in \mathbb{R}^T$, which can also be written in matrix form as $\mathbf{X} = \mathbf{AS}$, assumes that a single dataset is formed from the linear mixture of

$T$ independent sources, *i.e.*, $p(\mathbf{s}) = \prod_{t=1}^{T} p_t(s_t)$. Here $\mathbf{x} \in \mathbb{R}^T$ denotes the random vector that contains the $T$ mixtures, $x_t, 1 \leq t \leq T$. The estimates are given as $\hat{\mathbf{s}} = \mathbf{W}\mathbf{x}$, where $\mathbf{W}$ is a demixing matrix estimated minimizing the mutual information cost function,

$$\mathcal{J}_{\text{ICA}} = \sum_{t=1}^{T} \mathcal{H}(\hat{s}_t) - \log|\det \mathbf{W}| - \mathcal{H}(\mathbf{x}). \tag{2.2}$$

In (2.2) $\mathcal{H}(\hat{s}_t)$ denotes the entropy of $\hat{s}_t$, $\log|\det \mathbf{W}|$ acts as a regularization term and $\mathcal{H}(\mathbf{x})$ denotes the entropy of the observed signals, which is a constant with respect to $\mathbf{W}$ [13].

By modeling and exploiting different types of statistical diversity, such as sample dependence and higher order statistics (HOS), various ICA formulations are developed. The most commonly used diversity, HOS, is exploited by ICA implementations such as Infomax [49] and FastICA [50]. While FastICA and Infomax make use of fixed nonlinearities, algorithms like entropy bound minimization (EBM) use a flexible density model for each source estimate and hence, maximizes independence for a wider class of source distributions in an efficient manner [51]. Entropy rate bound minimization (ERBM) extends EBM by using an invertible filter and takes both higher order statistics and sample dependence into account [52, 53]. ERBM provides a better match for fMRI analysis due to ability to account for voxel-wise dependence and flexible density model of the spatial maps, and has shown superior performance compared with other widely-used ICA algorithms for the analysis of fMRI data [54, 55].

### 2.1.3 Estimation of fMRI sources based on statistical independence

The assumption of source independence has shown promising and reliable results for the analysis of fMRI data [8], and has been used widely to identify biomarkers from different population groups. The linear mixing model for ICA of fMRI data, defined in (2.1), is typically overdetermined in nature, *i.e.*, the number of spatial maps, $N$, is less than the number of observations, $T$. Hence applying dimensionality reduction techniques such as

principal component analysis (PCA) on each subject's dataset, prior to ICA is a common practice in order to obtain a signal subspace, $\mathbf{X} \in \mathbb{R}^{N \times V}$, where $N$ is the number of sources.

PCA estimates uncorrelated features in the order of highest variance, thus defining the signal subspace using the features that provide most information about the dataset. The principal component transformation is associated with the singular value decomposition of $\overline{\mathbf{X}}$, and is expressed as $\overline{\mathbf{X}}^T = \mathbf{UDF}$, where $\mathbf{D}$ is a $V \times T$ diagonal matrix consisting of the singular values of $\overline{\mathbf{X}}^T$, $\mathbf{U}$ is a $V \times V$ matrix consisting of the left singular vectors of $\overline{\mathbf{X}}$ and $\mathbf{F}$ is a $T \times T$ matrix, whose columns are $T$ orthogonal right singular vectors of $\overline{\mathbf{X}}$, also equivalent to the eigenvectors of the covariance matrix of $\overline{\mathbf{X}}$. Principal components of the observation set, $\overline{\mathbf{X}}$, are obtained by considering the $N$ right singular vectors corresponding to the first $N$ highest singular values, and are computed as $\mathbf{X} = \left(\overline{\mathbf{X}}^T \mathbf{F}_N\right)^T$, where $\mathbf{F}_N$ is a $T \times N$ matrix.

ICA is applied on the signal subspace, $\mathbf{X}$, to estimate $\mathbf{A}$ and $\mathbf{S}$, where $\mathbf{A} \in \mathbb{R}^{N \times N}$ is the mixing matrix and $\mathbf{S} \in \mathbb{R}^{N \times V}$ is the source matrix, the rows of which denote statistically independent spatial maps. The observation set, $\overline{\mathbf{X}}$, and estimated source matrix, $\mathbf{S}$, can then be approximated as $\overline{\mathbf{X}} = (\mathbf{F}_N \mathbf{A})\,\mathbf{S}$. The time courses of the $N$ sources are the columns of the matrix, $\widetilde{\mathbf{A}} \in \mathbb{R}^{T \times N}$, which can be computed as $\widetilde{\mathbf{A}} = \mathbf{F}_N \mathbf{A}$. Hence, the general model for fMRI dataset can be expressed using the estimated source matrix, $\mathbf{S}$, and time course matrix, $\widetilde{\mathbf{A}}$, as $\overline{\mathbf{X}} = \widetilde{\mathbf{A}}\mathbf{S}$, and is shown in Fig. 2.2.

ICA is originally designed for analysis of a single subject's fMRI data. Group independent component analysis (gICA) is an extension of ICA for the analysis of multi-subject fMRI data [9, 10]. It performs two levels of dimensionality reduction, where the first level involves the application of PCA on each subject's data individually in order to obtain a signal subspace for each subject. In the second level, the signal subspace for each subject are temporally concatenated to form a matrix and a group-level PCA is performed on this

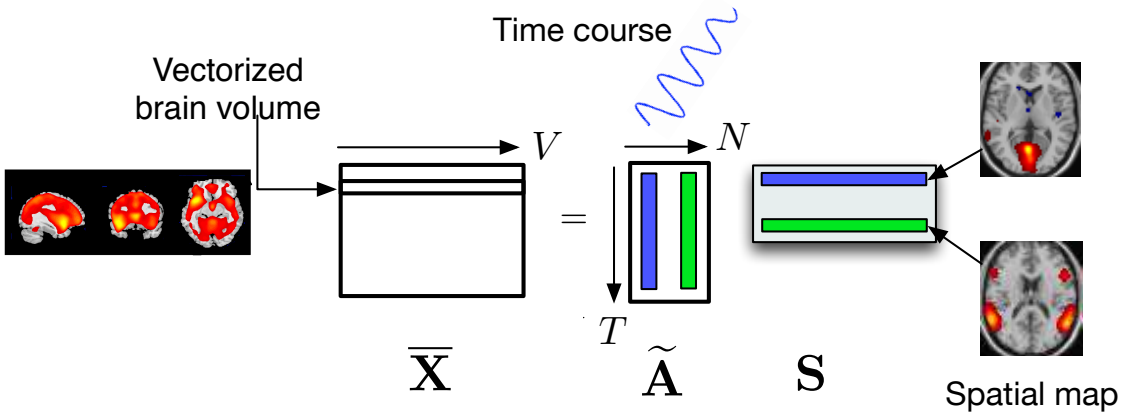


FIG. 2.2. Given an observation matrix, $\overline{\mathbf{X}}$, ICA decomposes a single subject's fMRI dataset into $\widetilde{\mathbf{A}}$ and $\mathbf{S}$, where the columns of $\widetilde{\mathbf{A}}$ are the time courses and the rows of $\mathbf{S}$ are the corresponding spatial maps.

matrix to obtain group-level principal components, which represent the features that account for most variability across subjects. Thus these components represent the subspace spanned by the features that are common across subjects. Since PCA estimates uncorrelated features, which separates the components using only second order statistics, ICA is performed on the principal components to estimate maximally independent components. The choice of ICA algorithm plays a vital role in the estimation of fMRI sources. In our work, we use the ERBM algorithm [52, 53] to account for HOS and sample dependence, which has shown better performance than the widely-used ICA algorithm, Infomax [54, 55]. The group-level ICA features are the global representation of the functional networks across all subjects, which are back-reconstructed to obtain subject-specific features and corresponding time courses, as shown in Fig. 2.3

GICA is one of the most widely used data-driven technique to analyze multi-subject fMRI data. It has shown desirable performance in terms of extracting functional networks common to a large-scale fMRI dataset [56]. However gICA is limited in terms of cap-

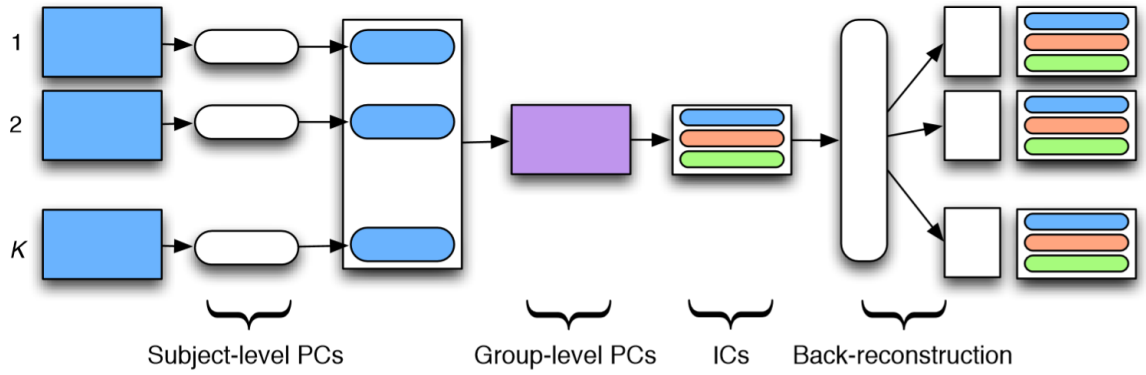


FIG. 2.3. GICA model for analysis of multi-subject fMRI data. Given $K$ datasets from $K$ subjects, GICA first performs PCA on each subject's data to obtain subject-level principal components (PCs). The subject-level PCs from all subjects are concatenated vertically and a second-level PCA is applied, in order to obtain a subspace spanned by the common components across all subjects. ICA is applied on the group-level PCs to estimate group level independent components (ICs). These ICs are then back-reconstructed in order to obtain subject-specific time courses and spatial maps.

turing subject-specific information since most of the variability is lost in the group-level dimensionality reduction step. Hence a method that jointly analyzes large-scale fMRI data while preserving subject variability is beneficial. IVA provides a flexible model to preserve subject-specific information while capturing the joint information of multiple subjects, and is discussed in Section 2.2.

### 2.1.4 Extraction of time-varying functional networks

GICA has also been widely used for temporal dFNC analysis, in which the back-reconstructed, subject-specific time courses are divided into overlapping windows and FC is obtained at each time window. This however, assumes that the spatial networks are stationary, as shown in Fig.1.1(b). Model-driven methods such as ROI-based methods, have been used to obtain time-varying spatio-temporal patterns and have shown better classification of subjects when variability in both spatial and temporal domains is considered compared with variability assumed in either spatial or temporal domain [31, 32]. Dy-

namic mode decomposition (DMD), a spatio-temporal modal decomposition technique, has demonstrated changes in the temporal activation of RSNs [33]. Although these techniques provide interesting results, the use of pre-defined ROIs causes the estimated FC to be sensitive to network selection whereas DMD requires significant dimension reduction that may restrict the method to estimation of few spatial components. Hence a more flexible model that simultaneously captures both time-varying patterns and spatial networks of the whole brain is desirable.

## 2.2 Independent vector analysis

IVA is a type of joint blind source separation algorithm that jointly estimate components that are independent within each dataset and dependent across datasets. Given $K$ datasets, each comprised of $N$ components, $\mathbf{x}^{[k]} \in \mathbb{R}^N,\ k = 1, \ldots, K$, we can write the general IVA model as,

$$\mathbf{x}^{[k]} = \mathbf{A}^{[k]}\mathbf{s}^{[k]},\ \ k = 1, \ldots, K, \tag{2.3}$$

where $\mathbf{A}^{[k]} \in \mathbb{R}^{N \times N}$ is the mixing matrix. IVA estimates $K$ demixing matrices, $\mathbf{W}^{[k]}$, to compute the source estimates, $\hat{\mathbf{s}}^{[k]} = \mathbf{W}^{[k]}\mathbf{x}^{[k]}$, by maximizing the likelihood function or equivalently minimizing the mutual information based cost function given as [13, 57],

$$\mathcal{J}_{\text{IVA}} = \sum_{n=1}^{N}\left[\sum_{k=1}^{K}\mathcal{H}\left(\hat{s}_n^{[k]}\right) - \mathcal{I}\left(\hat{\mathbf{s}}_n\right)\right] - \sum_{k=1}^{K}\log\left|\det \mathbf{W}^{[k]}\right| - C_1, \tag{2.4}$$

where $C_1$ is a constant term independent of the demixing matrices, $\mathcal{H}\left(\hat{s}_n^{[k]}\right)$ denotes the entropy of the $n$th source estimate for the $k$th dataset, and $\mathcal{I}\left(\mathbf{s}_n\right)$ denotes the mutual information of the $n$th source component vector (SCV), $\hat{\mathbf{s}}_n^T = \left[\hat{s}_n^{[1]}, \ldots, \hat{s}_n^{[K]}\right]$. An SCV takes into account the dependence across the datasets and the $n$th SCV is formed by concatenating the $n$th component from all the $K$ datasets as shown in Fig. 2.4. The covariance matrix of the $n$th SCV, $\Sigma_n \in \mathbb{R}^{K \times K}$, is a positive definite matrix. The minimization of the cost

function simultaneously weighs the independence within the dataset through the entropy term along with the log determinant term and dependence across the datasets through the mutual information term. For a given set of observations, the IVA model can be written as $\mathbf{X}^{[k]} = \mathbf{A}^{[k]}\mathbf{S}^{[k]} \in \mathbb{R}^{N\times V}$, where $\mathbf{S}^{[k]} = \left[\mathbf{s}_1^{[k]}, \ldots, \mathbf{s}_N^{[k]}\right]^T$, $\mathbf{s}_n^{[k]} \in \mathbb{R}^V, n = 1, \ldots, N$ are latent sources and $V$ is the number of samples. The estimated sources are obtained using $\hat{\mathbf{S}}^{[k]} = \mathbf{W}^{[k]}\mathbf{X}^{[k]}$ and the $n$th SCV is defined as $\mathbf{s}_n = \left[\mathbf{s}_n^{[1]}, \ldots, \mathbf{s}_n^{[K]}\right]^T \in \mathbb{R}^{K\times V}$.

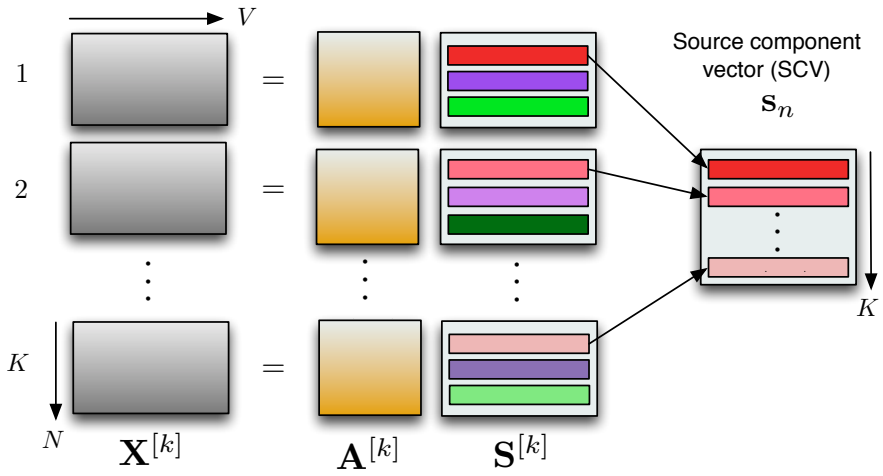


FIG. 2.4. Given a set of observations, the IVA model is given as $\mathbf{X}^{[k]} = \mathbf{A}^{[k]}\mathbf{S}^{[k]}$, $k = 1, \ldots, K$, where $\mathbf{A}^{[k]}$ is the mixing matrix and the rows in $\mathbf{S}^{[k]}$, are the latent sources that are dependent across datasets. The $n$th SCV is formed by grouping the corresponding $n$th source from each dataset together.

Recent IVA algorithms utilize the decoupling trick that allows the method to individually optimize each demixing vector in a flexible and efficient manner [57, 58]. We will now introduce the implementation of the decoupling trick in IVA. We define $\mathbf{u}_n^{[k]}$ as the $n$th decoupling vector such that $\tilde{\mathbf{W}}^{[k]}\mathbf{u}_n^{[k]} = 0$ and $\tilde{\mathbf{W}}^{[k]}$ is formed by removing the $n$th row of $\mathbf{W}^{[k]}$. It is shown that $\left|\det\left(\mathbf{W}^{[k]}\right)\right| = \left|\left(\mathbf{u}_n^{[k]}\right)^T \mathbf{w}_n^{[k]}\right| \omega_n^{[k]}$, where $\omega_n^{[k]} \triangleq \sqrt{\left|\det\left(\tilde{\mathbf{W}}^{[k]}\left(\tilde{\mathbf{W}}^{[k]}\right)^T\right)\right|}$

[58]. Following [57], the cost function in (2.4) can be rewritten as,

$$\mathcal{J}_{\text{IVA}} = \sum_{n=1}^{N}\left[\sum_{k=1}^{K}\mathcal{H}\left(\hat{s}_n^{[k]}\right) - \mathcal{I}\left(\hat{\mathbf{s}}_n\right)\right] - \sum_{k=1}^{K}\log\left|\left(\mathbf{u}_n^{[k]}\right)^T\mathbf{w}_n^{[k]}\right|\omega_n^{[k]} - C_1, \tag{2.5}$$

The terms $\omega_n^{[k]}$ and $\sum_{k=1}^{K}\mathcal{H}\left(\hat{s}_m^{[k]}\right) - \mathcal{I}\left(\hat{\mathbf{s}}_m\right)$ for $m \neq n$, are independent of $\mathbf{w}_n^{[k]}$ and are fixed with respect to changes in $\mathbf{w}_n^{[k]}$. Thus, the cost function used for individually updating $\mathbf{w}_n^{[k]}$ consist only of the following terms,

$$\mathcal{J}_{\text{IVA}}\left(\mathbf{w}_n^{[k]}\right) = \left[\sum_{k=1}^{K}\mathcal{H}\left(\hat{s}_n^{[k]}\right) - \mathcal{I}\left(\hat{\mathbf{s}}_n\right)\right] - \log\left|\left(\mathbf{u}_n^{[k]}\right)^T\mathbf{w}_n^{[k]}\right| - C_2 \tag{2.6}$$

where $C_2$ denotes the quantity containing all the fixed terms. Derivative of (2.6) with respect to each demixing vector, $\mathbf{w}_n^{[k]}$ is given by,

$$\frac{\partial\mathcal{J}_{\text{IVA}}\left(\mathbf{w}_n^{[k]}\right)}{\partial\mathbf{w}_n^{[k]}} = E\left\{\phi_n^{[k]}\mathbf{x}^{[k]}\right\} - \frac{\mathbf{u}_n^{[k]}}{\left(\mathbf{u}_n^{[k]}\right)^T\mathbf{w}_n^{[k]}}, \tag{2.7}$$

where $\phi_n^{[k]} \triangleq -\partial\log p\left(\hat{\mathbf{s}}_n\right)/\partial\hat{s}_n^{[k]}$. The gradient is used to iteratively update the demixing vector as follows,

$$\mathbf{w}_n^{[k]} = \mathbf{w}_n^{[k]} + \eta\partial\mathcal{J}_{\text{IVA}}/\partial\mathbf{w}_n^{[k]},$$

where $\eta$ is the step size.

### 2.2.1 Choice of IVA algorithm

The assumption of a different model for the latent source distribution, $p\left(\hat{\mathbf{s}}_n\right)$ has led to the development of different IVA algorithms. IVA-Gaussian (IVA-G) assumes that the underlying SCVs are multivariate Gaussian [57], and thus only takes second-order statistics (SOS) into account and estimates the covariance matrix for each SCV, $\mathbf{\Sigma_n} \in \mathbb{R}^{K\times K}$. IVA-Laplacian (IVA-L) assumes the sources are multivariate Laplacian distributed [59] and takes only higher-order statistics (HOS) into account. It assumes there is no second-order correlation within each SCV, *i.e.*, the covariance matrix is an identity matrix for all SCVs.

Although the assumption of no second-order correlation favors some applications, in many others, such as fMRI, it degrades the estimation performance since fMRI sources exhibit a moderate level of correlation across datasets [8, 10]. IVA-GL, another implementation of IVA that performs IVA-L initialized to the result of IVA-G, has shown more robust performance than using IVA-G or IVA-L alone [57] since it accounts for both SOS and HOS, although sequentially [8]. In the next section, we introduce the IVA-L-SOS algorithm that jointly accounts for SOS and HOS.

### 2.3 IVA on fMRI data

A number of studies have shown the superior performance of IVA to analyze fMRI data as compared with gICA in terms of capturing subject variability [11–13]. The IVA model applied on multi-subject fMRI data is shown in Fig.2.5. For the $k$th subject, the $t$th snapshot of the three dimensional brain scan is vectorized to form rows of the $k$th data matrix, $\overline{\mathbf{X}}^{[k]} \in \mathbb{R}^{T\times V}, k = 1,\ldots,K$, where $K$ is the number of subjects. Following the definition of ICA of fMRI data, the number of sources are less than the number of time-points. Hence PCA is typically applied on each subject's data to obtain a signal subspace, $\mathbf{X}^{[k]} \in \mathbb{R}^{N\times V}$. The IVA model is then written as $\mathbf{X}^{[k]} = \mathbf{A}^{[k]}\mathbf{S}^{[k]}$, and the $k$th mixing matrix, $\mathbf{A}^{[k]}$, is back-reconstructed to obtain the time courses for each subject as $\widetilde{\mathbf{A}}^{[k]} = \mathbf{F}^{[k]}\mathbf{A}^{[k]}$. The matrix $\mathbf{F}^{[k]}$, is the reduction matrix for the $k$th subject. The rows of source matrix represent maximally independent functional networks that are dependent across subjects. The columns of the mixing matrix correspond to the subject-specific time course of the corresponding functional network. The $n$th source from each dataset is grouped together to form a $K$-dimensional SCV, which represents subject-specific representation of a functional network, as shown in Fig.2.5. In Fig.2.5, an example of a network corresponding to the visual cortex is shown for two different subjects.

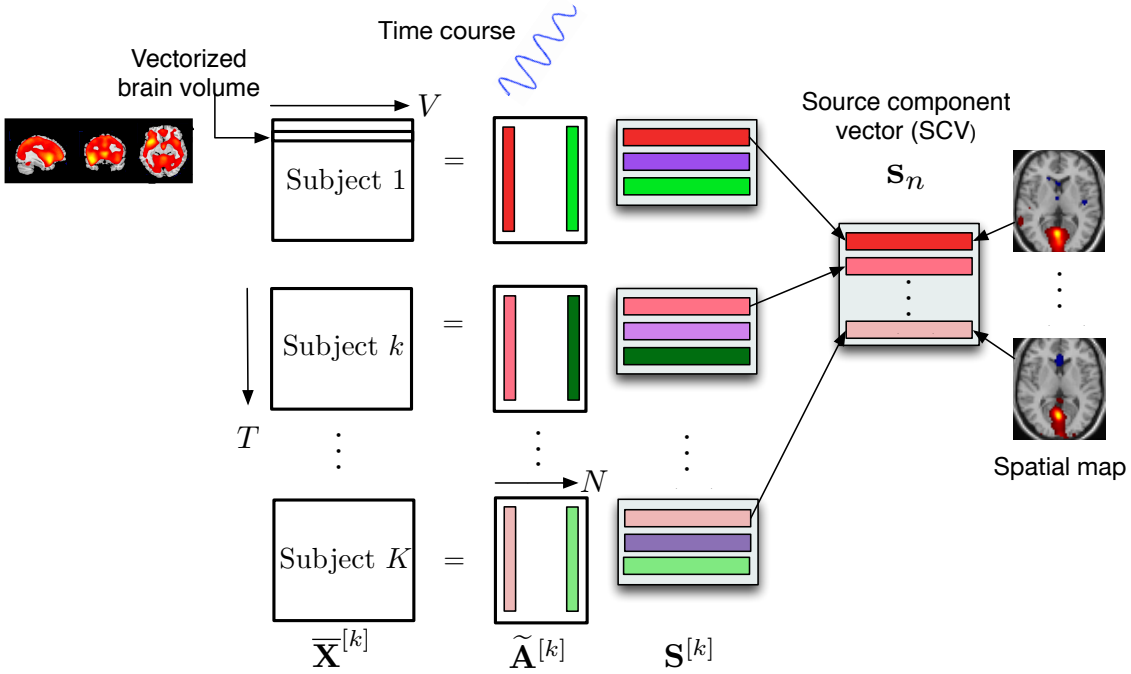


FIG. 2.5. IVA model for analysis of multi-subject fMRI data. The $t$th time snapshot of a subject's three dimensional brain scan is vectorized to form the $t$th row of the data matrix, $\overline{\mathbf{X}}^{[k]}$. IVA decomposes the $K$ datasets corresponding to $K$ subjects into subject-specific mixing matrix and source matrix. The rows of source matrix represent maximally independent functional networks that are dependent across subjects. The columns of the mixing matrix correspond to the subject-specific time course of the corresponding functional network.

## 2.4 IVA-L-SOS algorithm

In the analysis of fMRI data, it is widely known that the functionally relevant networks have a super-Gaussian distribution [8]. However, the level of correlation between a network for one subject with the same network from another subject is unknown. In order to investigate the level of correlation, we perform group ICA on three datasets: MRN-resting-state fMRI (rst-fMRI) dataset acquired from 327 subjects at the Mind Research Network (MRN) [56], Center for Biomedical Research Excellence (COBRE) dataset, which is available on the collaborative informatics and neuroimaging suite data exchange reposi-

tory (http://coins.mrn.org/dx) [60] and sensorimotor task-related fMRI dataset, which is a part of the MIND Clinical Imaging Consortium (MCIC) dataset [61]. The number of components is estimated using the entropy-rate based order selection by finite memory length model. We visually selected functionally relevant components and back-reconstructed to obtain subject-specific components. Pearson's correlation coefficient between a component from one subject and the same component from another subject is obtained for each pairs of subjects and for all selected components. The distribution of the correlation values of all unique pairs is shown in Fig. 2.6, for the three datasets. We can see that the components exhibit low-moderate levels of correlation between subjects.

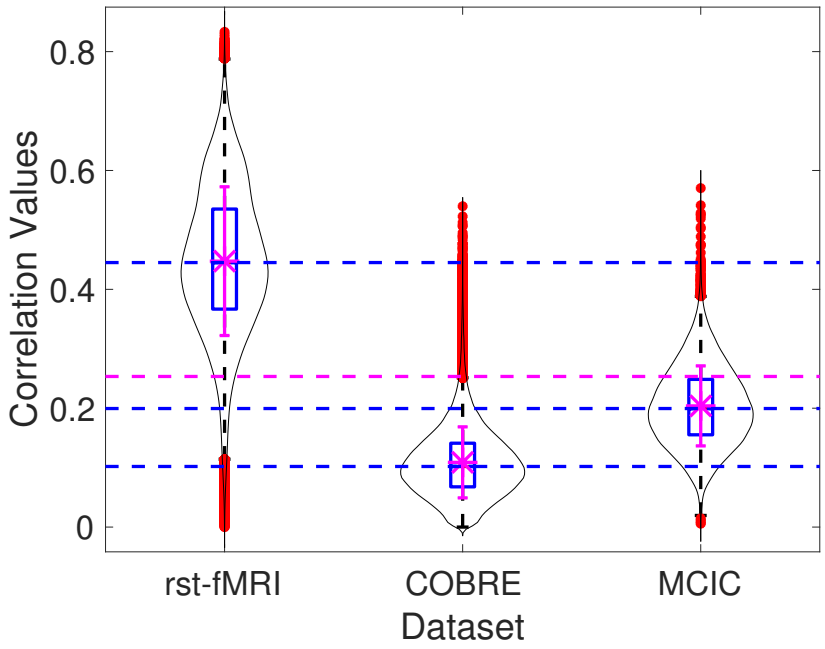


FIG. 2.6. Distribution of correlation values for all pairwise correlations between subjects computed for all functionally relevant components. The components exhibit low-moderate levels of correlation between subjects.

Since the SCVs are multivariate super-Gaussian distributed with a low to moderate level of correlation across datasets, an algorithm that simultaneously exploit the benefits

of these algorithms is preferable. In this section, we introduce the IVA-L-SOS algorithm that assumes the sources are multivariate Laplacian distributed, like IVA-L, but also takes second-order correlation of the SCVs into account, like IVA-G, for full statistical characterization of a Laplacian multivariate random vector. It jointly exploits both second and higher order statistics unlike IVA-GL, which does it sequentially.

The multivariate generalized Gaussian distribution (MGGD) covers a wide range of unimodal distributions by controlling the shape parameter, $\beta$, such as super-Gaussian ($\beta < 1$), normal ($\beta = 1$) and sub-Gaussian ($\beta > 1$), and assumes second-order correlation within an SCV [62]. The MGGD is given by,

$$p(\mathbf{s};\boldsymbol{\Sigma},\beta) = \frac{K\Gamma(K/2)\,|\boldsymbol{\Sigma}|^{-1/2}}{\pi^{[K/2]}\Gamma(1+\frac{K}{2\beta})2^{1+\frac{K}{2\beta}}}\,\mathrm{e}^{-\frac{1}{2}[\mathbf{s}^T\boldsymbol{\Sigma}^{-1}\mathbf{s}]^{\beta}}, \tag{2.8}$$

where $K$ is the dimension of the multivariate distribution, $\boldsymbol{\Sigma}$ is a covariance matrix and $\Gamma(\cdot)$ is the Gamma function. By setting the shape parameter $\beta$ to 0.5, the MGGD distribution is equivalent to a multivariate Laplacian distribution that accounts for second-order correlation through $\boldsymbol{\Sigma}$ and is expressed as,

$$p(\mathbf{s};\boldsymbol{\Sigma}) = \frac{\Gamma(K/2)\,|\boldsymbol{\Sigma}|^{-1/2}}{2^{K+1}\pi^{[K/2]}\Gamma(K)}\exp\left\{-\frac{1}{2}\sqrt{\mathbf{s}^T\boldsymbol{\Sigma}^{-1}\mathbf{s}}\right\}, \tag{2.9}$$

where $\boldsymbol{\Sigma}$ estimated at each iteration. Since fMRI sources are in general expected to have a super-Gaussian distribution, like Laplacian [8], and are dependent across subjects/windows, the IVA-L-SOS model is a good match for fMRI data.

The score function, $\phi_n^{[k]}$, for MGGD is given by,

$$\phi(\mathbf{s}) = \left\{\frac{\Gamma\left(\frac{K+2}{2\beta}\right)}{K\Gamma\left(\frac{K}{2\beta}\right)}\right\}^{\beta}\beta\boldsymbol{\Sigma}^{-1}\mathbf{s}\left(\mathbf{s}^T\boldsymbol{\Sigma}^{-1}\mathbf{s}\right)^{\beta-1}, \tag{2.10}$$

where the Gamma functions, $\Gamma(\frac{K+2}{2\beta})$ and $\Gamma\left(\frac{K}{2\beta}\right)$ grow at a rate faster than the exponential function towards infinity as $M$ increases, leading the score function to be undefined. Since

$\beta = 0.5$ provides a better match for fMRI sources [8], by direct substitution of $\beta = 0.5$, which corresponds to multivariate Laplacian distribution, in (2.10), we obtain

$$\phi(\mathbf{s}) = (K+1)^{0.5} \frac{\boldsymbol{\Sigma}^{-1}\mathbf{s}}{\sqrt{\mathbf{s}^T\boldsymbol{\Sigma}^{-1}\mathbf{s}}},$$

which enables a stable version for large $K$.

The successful performance of IVA algorithms that account for SOS, such as IVA-G and IVA-L-SOS, depends on the structure of the covariance matrix, $\boldsymbol{\Sigma}$, which is a positive definite matrix. Throughout the dissertation, we assume that the sources are normalized, and hence the covariance matrix and the correlation matrix are equivalent. In Appendix A1, we talk about three different structures for the generation of the correlation matrix and discuss the bounds for these matrices to be positive definite.

## 2.5 Consistent Run Selection using cross joint ISI

IVA is an iterative algorithm and there is a need to determine a best reproducible solution for a given set of the data. In order to identify the most consistent solution we perform IVA on the same set of observations for multiple runs, with each run initialized randomly, and apply the consistent run selection using cross joint inter-symbol interference (jISI) method, which is an extension of the method proposed in [63] to multiple datasets. The jISI metric measures the performance of IVA algorithm when the groundtruth is available. If the demixing matrix is perfectly estimated, the matrix $\mathbf{G}^{[k]} = \mathbf{W}^{[k]}\mathbf{A}^{[k]}$ is identity subject to scaling and permutation ambiguities. The jISI metric computes the distance of $\mathbf{G}^{[k]}$ from the identity matrix and is computed as,

$$\text{jISI} = \frac{1}{2N(N-1)}\left[\sum_{n=1}^{N}\left(\sum_{m=1}^{N}\frac{\bar{g}_{n,m}}{\max_p \bar{g}_{n,p}} - 1\right) + \sum_{m=1}^{N}\left(\sum_{n=1}^{N}\frac{\bar{g}_{n,m}}{\max_p \bar{g}_{p,m}} - 1\right)\right], \tag{2.11}$$

where $\bar{g}_{n,m} = \sum_{k=1}^{K} \left| g_{n,m}^{[k]} \right|$ and $0 \leq \text{jISI} \leq 1$, where 0 indicates ideal separation. The cross jISI run selection method defines the cross jISI (cjISI), which measures the distance between the estimated demixing matrices across runs. Let $R$ denote the number of runs and $\mathbf{W}^{[k],(r)}$ denote the $k$th estimated demixing matrix obtained from the $r$th run. For two runs that are close to each other, the matrix $\mathbf{D}^{[k],(r_1 r_2)} = \mathbf{W}^{[k],(r_1)} \left( \mathbf{W}^{[k],(r_2)} \right)^{-1}$ is close to identity subject to scaling and permutation ambiguities, hence the cross jISI can defined as,

$$\text{cjISI}^{(r_1 r_2)} = \frac{1}{2N(N-1)} \left[ \sum_{n=1}^{N} \left( \sum_{m=1}^{N} \frac{\bar{d}_{n,m}}{\max_p \bar{d}_{n,p}} - 1 \right) + \sum_{m=1}^{N} \left( \sum_{n=1}^{N} \frac{\bar{d}_{n,m}}{\max_p \bar{d}_{p,m}} - 1 \right) \right],$$

where $\bar{d}_{n,m} = \sum_{k=1}^{K} \left| d_{n,m}^{[k]} \right|$. For each run, the cross jISI is computed between that run and all other runs and average distance is obtained as, $\overline{\text{cjISI}}^{(r)} = 1/R \sum_{r_1=1}^{R-1} \text{cjISI}^{(r_1 r)}$, $r \neq r_1$. The most consistent run, $r_{\text{consistent}}$, is obtained as the run that has the least average distance from all the runs, *i.e.*, $r_{\text{consistent}} = \text{argmin}_r \, \overline{\text{cjISI}}^{(r)}$, $r = 1, \ldots, R$.

### 2.6 Permutation test for identifying significant differences between two groups

The identification of features that demonstrate differences between two groups of subjects is one of the primary goals for the analysis of fMRI data. In this work, we use the permutation test on the metric of interest to evaluate differences between groups under study, which is a non-parametric statistical test which controls the false alarm rate under the null hypothesis [64, 65]. The idea of a permutation test is to determine whether the difference between the two groups is large enough to reject the null hypothesis that two groups have identical distributions. The test first obtains the observed difference between the two groups using the true labels of the subjects. The labels for the subjects from the two groups are randomly pooled and a difference statistic using the new labels is obtained for every permutation of the labels. A distribution of the calculated differences is the exact distribution of possible differences under the null hypothesis. If the observed difference is

within 95% of the exact distribution, then we do not reject the null hypothesis. This test hence assumes that there are no differences between the two groups and tests if this hypothesis is true or not. We use the $t$-statistic obtained from a two-sample $t$-test to measure the difference between the two groups and identify whether a particular group has higher intensity using the sign of the $t$-statistic.

## 2.7 Summary

In this chapter, we briefly introduced two broader classes of techniques used to extract features from fMRI data, namely model-driven and data-driven techniques. We emphasized the need for a flexible method that estimates functional networks from multi-subject fMRI data while preserving subject-specific information from a large-scale fMRI data. We discussed the general IVA model and that it provides a flexible framework for the analysis of fMRI data. Since we typically obtain multiple IVA solutions, we discussed a technique to select the most consistent solution using a cross-joint ISI run selection technique. We ended the section by introducing a statistical test for identifying significant differences between two groups under study.

Although IVA provides a flexible framework for estimating sources of different nature, its performance is affected by a number of factors. In the next chapter, we discuss these factors in further detail and provide simulation examples to demonstrate the effect of *high dimensionality* in IVA.

Chapter 3

# KEY ASPECTS OF INDEPENDENT VECTOR ANALYSIS

In this chapter, we discuss the key factors that affect the performance of IVA, namely, number of sources, number of datasets, number of samples and level of correlation among sources across datasets. We study the performance of IVA with respect to number of datasets and level of correlation, for a fixed number of samples and sources, and with respect to number of datasets and sources, for a fixed number of samples and level of correlation, using simulated data.

## 3.1 Introduction

ICA is a popular data-driven approach used to extract subject-specific time courses and spatial maps under the assumption of statistical independence, however it is limited to the analysis of a single dataset. Two extensions of ICA, namely joint ICA and gICA, are proposed to analyze multiple datasets that perform ICA on a matrix constructed by concatenating multiple datasets either along the temporal dimension or spatial dimension. However, joint ICA assumes a common mixing matrix or time courses across multiple datasets, while capturing spatial variability across multiple datasets. GICA jointly analyzes the data from multiple subjects and estimates a common, global representation of the functional networks across subjects, however it might be limited in terms of preserving sub-

ject variability. IVA is an extension of ICA to multiple datasets that jointly decomposes the multi-subject data into subject-specific time courses and spatial maps. It has been shown in various studies that IVA is better in capturing subject variability [11–13] compared with gICA and provides automatic source alignment across subjects by exploiting the source dependence across datasets. It presents a wide range of algorithms depending on the assumption of the latent multivariate source distribution and provides general identification conditions that allow for flexibility in the estimation of the underlying sources [13]. Although IVA provides a general framework for the analysis of multi-subject fMRI data, its performance depends on a number of factors such as number of samples [66], number of datasets [67], number of sources and the level of correlation between the marginals of the multivariate sources.

As with maximum likelihood based estimators, the performance of IVA improves when the sample size increases [66]. On the other hand, with more datasets available to exploit the dependence structure in IVA, the performance of IVA is expected to improve with an increase in the number of datasets, due to the availability of more cross-dataset information [57]. However, this effect depends on the number of samples available. Given an infinite number of samples, the performance of IVA will keep on improving with increasing number of datasets. However, in real world applications, there is a limitation to the number of available samples, and the trend of improvement in performance with increasing number of datasets is expected to stop after a certain limit, after which the performance degrades with a further increase in number of datasets [67]. We refer to this decrease in performance trend as the effect of high dimensionality in IVA. This trade-off between high dimensionality and utilization of maximal cross-dataset information depends not only on the number of samples, but also is a function of the number of sources and the level of correlation exhibited among the sources of an SCV. The performance of IVA is a joint effect of all these

factors and is not explored to the best of our knowledge.

In this chapter, we study how these factors affect the performance of IVA through simulations, and discuss the potential strengths and weaknesses of IVA.

## 3.2 Simulation study

### 3.2.1 Effect of number of datasets and level of correlation

In order to demonstrate the effect of the number of datasets and the level of correlation on IVA, for fixed $V$ and $N$, we generate $K$ datasets, $\mathbf{x}^{[k]} \in \mathbb{R}^N$, such that $\mathbf{x}^{[k]} = \mathbf{A}^{[k]}\mathbf{s}^{[k]}$. The elements in the mixing matrices, $\mathbf{A}^{[k]}, k = 1, \ldots, K$ are randomly generated from a uniform distribution. The $N$ SCVs are generated from a $K$-dimensional multivariate Laplacian distribution with a covariance structure $\mathbf{\Sigma}_n = \mathbf{Q}\mathbf{Q}^T$, where $\mathbf{Q} \in \mathbb{R}^{K\times K}$ is a randomly generated matrix. We vary the level of correlation within an SCV through the generation of the matrix $\mathbf{Q}$, where the elements in $\mathbf{Q}$ denoted as $q_{ij}$, are generated randomly from a normal distribution, $\mathcal{N}(0, 1)$ for Case 1, $\mathcal{N}(0.1, 0.3)$ for Case 2, a uniform distribution, $\mathcal{U}(-0.2, 0.8)$ for Case 3, $\mathcal{U}(0, 1)$ for Case 4, and $\mathcal{U}(0.1, 0.3)$ for Case 5. The resulting distribution of correlation values in $\mathbf{\Sigma}_n$ for $K = 10$ is shown in Fig. 3.1. We can see that the correlation values demonstrate an increasing trend from Case 1 to Case 5 corresponding to increase in the level of correlation within an SCV.

After obtaining the SCVs, the sources for the $k$th dataset are obtained by grouping together the $k$th row from all the $N$ SCVs, $\mathbf{s}^{[k]} = \left[s_1^{[k]}, \ldots, s_N^{[k]}\right]$. We generate $V = 1000$ samples and vary the number of datasets from 2 to 40. We obtain three independent observation sets of the datasets, $\mathbf{X}^{[k]}$, by randomly generating the mixing matrices and sources for each set. IVA using the IVA-L-SOS algorithm is performed for five runs on each set, and the performance of both methods is measured in terms of joint inter-symbol interference (jISI) [57]. The jISI metric measures the performance of the methods in terms of its ability to separate the sources ($0 \leq \text{jISI} \leq 1$), where 0 indicates better separation of underlying SCVs,

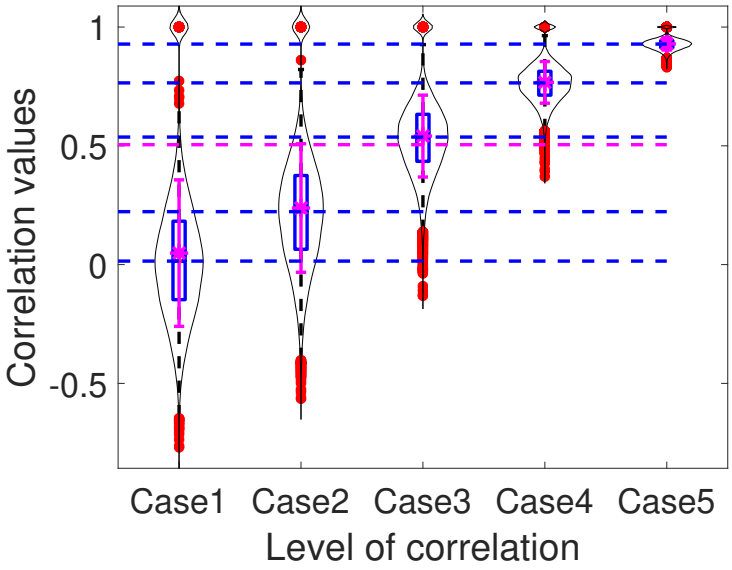


FIG. 3.1. Distribution of correlation values in $\mathbf{\Sigma}_n = \mathbf{Q}\mathbf{Q}^T$ for Cases 1-5.

*i.e.*, $\mathbf{W}^{[k]}\mathbf{A}^{[k]} = I$, $\forall k \in \{1, \ldots, K\}$. IVA-L-SOS simultaneously accounts for second and higher order statistics, and assumes the sources are correlated multivariate Laplacian distributed [67]. This assumption is a good model match for fMRI analysis since the sources tend to have a super-Gaussian distribution with correlation across subjects [8, 10]. The average of the jISI metric across all converged runs for IVA is shown in Fig. 3.2.

When there are sufficient samples available, the advantage of exploiting source dependence across datasets in IVA is observed in Fig. 3.2. The performance improves with increase in number of datasets for a fixed number of sources and samples. However, this increasing trend is observed upto a certain limit, after which IVA is affected by high dimensionality after $K = 20$. The effect of dimensionality in IVA is observed when there is insufficient statistical power to provide reliable and meaningful estimates of the high dimensional multivariate probability distribution functions, due to the availability of limited samples. Additionally the high dimensional effect is more prominent in Cases 1 and 2, *i.e.*,

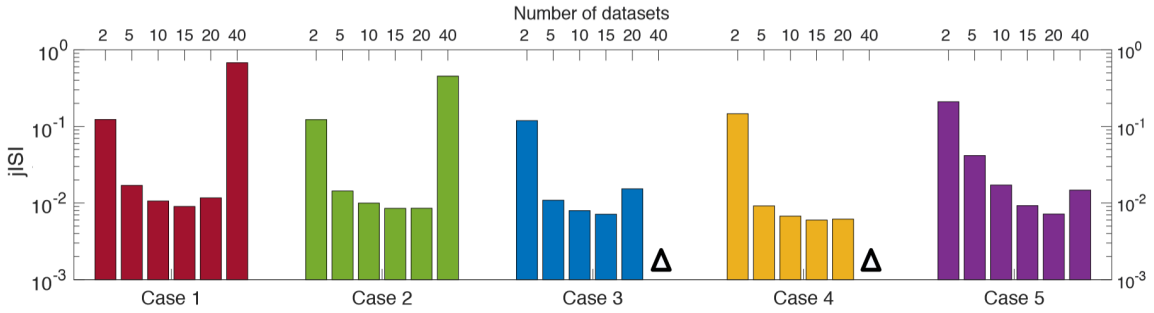


FIG. 3.2. Performance of IVA in terms of jISI with respect to number of datasets, $K$, for each case. The jISI metric is the average jISI computed across all converged runs. The level of correlation increases from Case 1 to Case 5 with Case 1 corresponding to low correlation within an SCV whereas Case 5 corresponds to high correlated SCVs. The number of sources and number of samples is fixed to $N = 85$ and $V = 1000$, respectively. For Case 3 and Case 4 at $K = 40$ no run converged in 1024 iterations, which is indicated by '$\triangle$', however with an increase in $K$ we start observing an increasing trend.

for the low correlated SCVs, since Cases 3 to 5 take advantage of the dependence structure in IVA, as compared to Cases 1 and 2. The low correlation structure of the SCVs for these cases have higher distances between the marginals resulting in the data points to be sparsely located in the multidimensional space, hence the estimation of such SCVs becomes even more difficult in high dimensional scenarios. For highly correlated SCVs, as in Case 5, the marginals are more densely located, which aids the estimation of these sources and yields a more efficient estimator in the maximum likelihood sense.

There has been a debate regarding the additional diversity of IVA, namely, source dependence across datasets, and that is IVA requires or forces the sources across datasets to be dependent and hence does not allow for variability across datasets. Cases 1 through 3 address this scenario where the distribution of the correlation values have high variability and low to moderate correlation across datasets. Note that for these cases, the jISI is similar to that of Cases 4 to 5 when the number of datasets is less than 20, which indicates that the performance of IVA is similar across different levels of correlation. Hence, IVA does

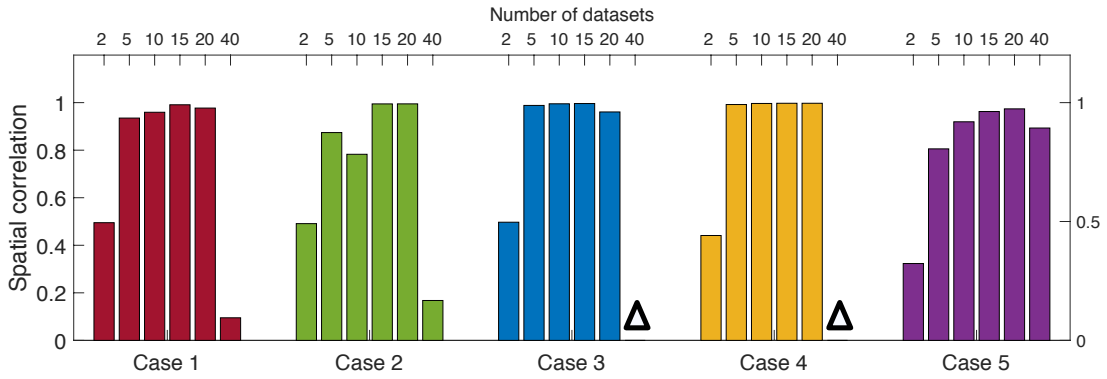


FIG. 3.3. Performance of IVA in terms of spatial correlation between estimated sources and ground truth, with respect to number of datasets, $K$, for each case. The level of correlation increases from Case 1 to Case 5 with Case 1 corresponding to low correlation within an SCV whereas Case 5 corresponds to high correlated SCVs. The number of sources and number of samples is fixed to $N = 85$ and $V = 1000$, respectively. For Case 3 and Case 4 at $K = 40$ no run converged in 1024 iterations, which is indicated by '$\triangle$', however with an increase in $K$ we start observing an decreasing trend.

not require or enforce the sources across datasets to be highly correlated. We also compute the spatial correlation of the estimated sources and ground truth in order to verify if IVA preserves variability across datasets, and observe similar trend, see Fig. 3.3. Spatial correlation between the estimated source at each dataset and the corresponding ground truth increases with increase in $K$ until $K = 20$, after which the correlation value drops. For number of datasets less than 20, the spatial correlation is high for all cases, indicating that IVA does not require or force the sources to be dependent and preserves dataset-specific information.

In the analysis of fMRI datasets, the $n$th SCV typically corresponds to a functional network activated across multiple subjects. The structure of the multivariate distributions of these SCVs show high activations in a smaller group of voxels and lower activation values for a larger group of voxels. This results in fMRI sources to have low correlations

across datasets, affecting their estimation significantly in high dimensional scenarios, see Appendix A3 for more details.

### 3.2.2 Effect of number of datasets and number of sources

In order to study the performance of IVA with respect to increase in number of datasets and sources, we generate simulated datasets similar to the set-up described in Section 3.2.1. We vary the number of datasets, $K$, from 2 to 60, and the number of sources, $N$, from 40 to 85, with a fixed sample size $V = 1000$. The SCVs are generated from a multivariate Laplacian distribution with a covariance structure, $\mathbf{\Sigma} = \mathbf{Q}\mathbf{Q}^T$, $q_{ij} = \mathcal{N}(0.1, 0.3)$. This structure results in low to moderately correlated sources that is a good match to the fMRI sources, since the fMRI sources are known to have a super-Gaussian distribution [8] with low to moderate level of correlation, see Appendix A3. The sources are linearly mixed using a randomly generated mixing matrix for each dataset to obtain the observation set, $\mathbf{X}^{[k]}$. We generate three different observation sets by randomly generating the mixing matrices and sources for each set. We obtain 20 runs of IVA using the IVA-L-SOS algorithm. We measure the performance of IVA using jISI, which measures the estimation of the whole demixing matrices. The estimated sources are aligned with respect to the original sources using correlation metric. The average of the jISI metric of the constrained sources across 20 runs and three observation sets for IVA is shown in Fig. 3.4.

From Fig. 5.1, we observe that IVA performance improves with an increase in number of datasets upto a certain limit for different numbers of sources. This range can be defined as the best range in which there are sufficient samples available for IVA to accurately estimate the underlying parameters. Although the increase in number of sources for a fixed number of datasets does not significantly affect the performance, it does determine the limit for better performance. The range of better performance becomes tighter as we increase the number of sources, after which we observe a degradation in performance due to the effect

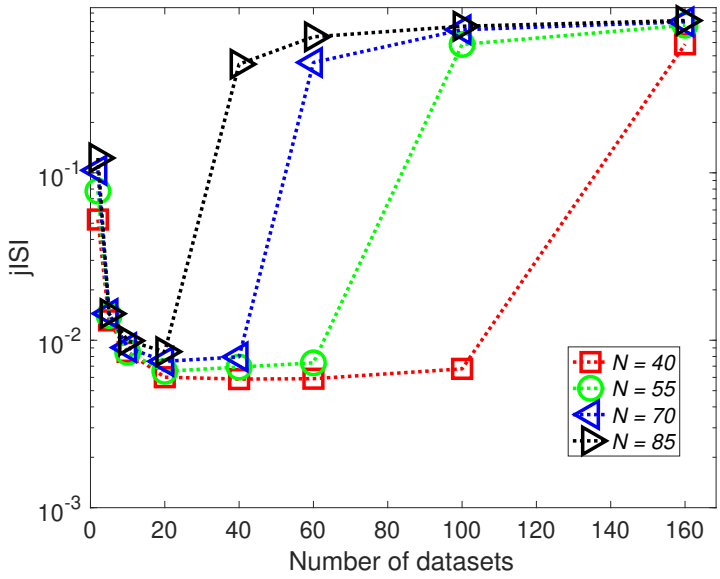


FIG. 3.4. Performance of IVA in terms of jISI with respect to number of datasets, $K$, and number of sources, $N$. For each $N$, the performance of IVA improves at first with increase in number of datasets, until a certain limit, after which the performance degrades with increase in $K$. The limit at which the performance changes depends on the number of sources, for a fixed number of samples.

of high dimensionality.

### 3.3 Summary

In this chapter, we demonstrate that the performance of IVA depends on a number of factors such as number of samples, number of datasets, number of sources and the level of correlation between the marginals of the multivariate sources. To summarize, the IVA performance degrades with decrease in number of samples and the level of correlation within the SCVs, and with an increase in datasets and number of sources. For a fixed number of samples and number of sources, the performance first improves with increase in number of datasets until a certain limit, after which the performance drops with further increase in number of datasets. The limit of is determined by the number of sources and

number of samples. For a higher number of sources, the limit is observed at a lower value of number of datasets. Since in real-world applications, such as in fMRI data, the number of samples is fixed, joint analysis of a large sample of subjects becomes a challenging problem. Additionally the use of a higher model order, *i.e.*, number of sources, is of interest in fMRI analysis in order to extract more functionally relevant networks [68, 69], which further increases the complexity in fMRI analysis.

In this work, we propose the use of prior information regarding the decomposition in order to address the effect of high dimensionality in IVA. In the next chapter, we talk about the proposed method to incorporate prior information into the IVA framework, using an adaptive tuning technique, and demonstrate its potential strength through simulations with respect to incorporating accurate and inaccurate reference signals.

Chapter 4

# ADAPTIVE CONSTRAINED INDEPENDENT VECTOR ANALYSIS

This chapter talks about the design of the adaptive constrained IVA (acIVA) algorithm that effectively incorporates prior information regarding the sources or the columns of the mixing matrix into the IVA cost function, by adaptively tuning the constraint parameter. We demonstrates the successful performance of acIVA over the regular constrained IVA (cIVA), which makes use of a fixed constraint parameter, using simulated data.

## 4.1 Introduction

The success of IVA is due to its use of a simple generative model that enables flexibility while minimizing the assumptions placed on the data. However, as discussed in Chapter 3, the performance of IVA suffers in high dimensional scenarios, *i.e.*, when the number of datasets or the number of sources is large for a fixed, smaller set of samples, and is more prominent in cases of low level of dependence across the datasets. In many applications, important prior information about the data is available and incorporating this information into the IVA framework is expected to improve the estimation of the true latent sources by providing a better model match. By incorporating prior information into the optimization process can provide a guidance for the search for a better solution in high dimensional scenarios, provided that the information is accurate. Acquiring accurate information about the

data is equally important in order to obtain meaningful results. This can be challenging is many applications since prior information extracted from one dataset may not be desirable for another dataset. In the case of fMRI analysis, information regarding functional networks varies across different groups of subjects. Hence using a fixed network structure extracted from one group of subjects to obtain the networks for a different group of subjects results in loss of subject-specific information. Hence an algorithm that provides a flexible way of incorporating prior information is desirable in order to capture variability across a large group of subjects.

In Chapter 2, we discussed two broader classes of feature extraction techniques for fMRI analysis, namely, model-driven and data-driven techniques. Model-driven techniques make stronger assumptions about the data and are robust to noise and other artifacts provided that the model is correct. However the performance of these methods depends on the model assumptions, which cannot be generalized to different datasets, limiting their usage. On the other hand, data-driven techniques make fewer/weaker assumptions about the data and enable the discovery of functional networks in a data-driven manner. However the performance of these methods depends on the model order, where the use of a higher model order results in splitting of functional networks, whereas the use of a lower model order results in functional networks getting merged with artifact and noise components. A technique that provides a balance between model-driven and data-driven techniques, and takes advantage of both is desirable. Incorporating prior information into a data-driven framework, such as in ICA, relaxes the independence assumption, and yields robust results [70]. With a fair amount of interest to benefit from the known information [71–76], a number of methods have been proposed to incorporate prior knowledge into the optimization framework [74, 77–80]. However, these methods do not make use of the decoupling trick that relaxes the assumption of orthogonality of the demixing matrices and make use of an

user-defined threshold to fix the effect of the prior information on the source estimation. Additionally, these methods are proposed for incorporating reference information regarding sources from one dataset, and cannot be used to exploit common prior information regarding multiple datasets.

A method was developed in [81] that takes advantage of this diversity, however, the mathematical framework is limited by the application, speech processing, and requires the demixing matrices to be orthogonal. Constrained IVA is an effective method that incorporates prior information regarding the sources or the columns of the mixing matrix into the IVA cost function [82]. It employs the decoupling trick that assumes the demixing matrices are non-orthogonal and relaxes the independence assumption by enabling a desirable balance between data-driven, which minimize the assumptions placed on the data and model driven methods, which make use of the prior information, which if correct yield them robust to noise and artifacts.

However, cIVA makes use of a user-defined constraint parameter that fixes the degree of correspondence between reference signal and the estimated component. The successful performance of cIVA depends on the selection of prior information and the user-defined constraint parameter, *i.e.*, when the prior information is incorrect a lower constraint parameter must be used such that the prior information is not enforced on the decomposition [67, 82]. On the other hand, when the prior information is correct, a higher constraint parameter must be used such that the components are deterred from effect of noise and artifacts. However, in most practical applications, the selection of a constraint parameter becomes difficult since it is unknown whether the information is accurate or inaccurate and becomes more complicated when information regarding multiple signals need to be incorporated. The use of a fixed constrained parameter also affects the estimation of dataset-specific information, and hampers one of the main objectives of analyzing fMRI data, *i.e.*,

preserving subject-specific information.

In this chapter, we introduce the proposed acIVA technique that adaptively tunes the constrained parameter and relaxes the orthogonality assumption by using the decoupling trick. We demonstrate the superior performance of cIVA and acIVA in terms of incorporating multiple reference signals into the IVA framework and in terms of their ability to preserve dataset-specific information, using simulated examples.

## 4.2 Adaptive constrained IVA

We will now introduce the formulation for acIVA. Let $d_l,\ l = 1, \ldots, L$, denote the $l$th reference sample belonging to a known vector $\mathbf{d}_l$ and $L$ denote the number of references. Note that the number of constraints, $L$, is less than or equal to $N$, and the index $n$ and $l$ can be used interchangeably for constrained sources or mixing vectors. In the following text we will use index $l$ to refer to constrained sources and $n$ to refer to the unconstrained sources. Given an inequality constraint function, $g\left(\hat{s}_l^{[k]}, d_l\right)$, the mutual information based cost function in (2.5) is optimized subject to the inequality constraint,

$$g(\hat{s}_l^{[k]}, d_l) = \rho_l^{[k]} \leq \epsilon(\hat{s}_l^{[k]}, d_l), \tag{4.1}$$

where $\hat{s}_l^{[k]} = \left(\mathbf{w}_l^{[k]}\right)^T \mathbf{x}^{[k]}$ is the estimated component, $\epsilon(\cdot, \cdot)$ is a function that defines the measure of similarity between the estimated source and reference sample, and $\rho_l^{[k]}$ is the constraint parameter. A simple dot product as the distance metric in (4.1) results the constraint function to be of the form $\mathbf{a}^T\mathbf{x} \geq b$, where $b$ acts as a lower bound on the product . Hence (4.1) provides a more general formulation for the constraint function allowing the use of different distance functions such as the Euclidean distance, square error and mutual information. In this work, we use Pearson's correlation coefficient as the distance function,

$$\epsilon(\hat{s}_l^{[k]}, d_l) = \left|\text{corr}\left(\hat{s}_l^{[k]}, d_l\right)\right|. \tag{4.2}$$

The distance function is hence normalized to be between $0 \leq \epsilon(\hat{s}_l^{[k]}, d_l) \leq 1$, and from (4.1) we have $0 \leq \rho_l \leq 1$. The constraint parameter, $\rho_l^{[k]}$, controls the degree of correspondence between reference signal and the estimated factor. The regular cIVA model proposed in [82] uses a fixed value for the constraint parameter and requires the user to define this value. However, in most application the effect of the prior information is not known making the selection of the constraint parameter a difficult task, and may introduce bias. Due to the presence of variability across datasets, the use of a fixed value for the constraint parameter does not effectively estimate the underlying components. Naturally, the selection of constraint parameter plays an important role in the effective estimation of the sources and leads to the need for an adaptive way for the method to select the constraint parameter. Hence we propose to adaptively tune the constraint parameter in order to effectively incorporate the prior information into the IVA decomposition.

We start by defining a set of possible values for $\rho$, denoted as $\mathcal{P}$. Following the definition in (4.1) and (4.2), we define the set $\mathcal{P}$ consisting of values between 0 and 1. The adaptive tuning technique selects a highest lower bound from this set using the following criterion,

$$\hat{\rho}_l^{[k]} = \arg\min_{\rho \in \mathcal{P}} \left[ \left| \rho - \left| \epsilon(\hat{s}_l^{[k]}, d_l) \right| \right| \right] \tag{4.3}$$

This updates computes $g(\hat{s}_l^{[k]}, d_k)$ for all $k$ and for each value in set $\mathcal{P}$ and selects the highest value of $\rho_n$ from set $\mathcal{P}$ that satisfies the condition in (4.1) for all datasets. A value for $\hat{\rho}_l^{[k]}$ is obtained using (4.3), at each iteration for all constrained sources, and is further used in the optimization of the constrained cost function.

In order to integrate the constraint into the IVA cost function, we use the decoupled version defined in (2.6), which allows the method to individually update each demixing vector. The constrained cost function defined using the augmented Lagrangian optimization

function is as follows,

$$\mathcal{J}\left(\mathbf{w}_l^{[k]}\right) = \mathcal{J}_{\text{IVA}}\left(\mathbf{w}_l^{[k]}\right) - \frac{1}{2\gamma_l}\left\{\left[\max\{0, \mu_l^{[k]} + \gamma_l g(\hat{s}_l^{[k]}, d_l)\}\right]^2 - (\mu_l^{[k]})^2\right\},$$

where $\gamma_l$ is the penalty parameter and $\mu_l^{[k]}$ is the Lagrange multiplier. The gradient of this function with respect to each demixing vector is given as,

$$\frac{\partial \mathcal{J}\left(\mathbf{w}_l^{[k]}\right)}{\partial \mathbf{w}_l^{[k]}} = \frac{\partial \mathcal{J}_{\text{IVA}}\left(\mathbf{w}_l^{[k]}\right)}{\partial \mathbf{w}_l^{[k]}} - g'\left(\hat{s}_l^{[k]}, d_l\right)\mu_l^{[k]}(d_l), \tag{4.4}$$

where $g'\left(\hat{s}_l^{[k]}, d_l\right)$ is the derivative of $g\left(\hat{s}_l^{[k]}, d_l\right)$ with respect to $\mathbf{w}_l^{[k]}$ and $\frac{\partial \mathcal{J}_{\text{IVA}}\left(\mathbf{w}_l^{[k]}\right)}{\partial \mathbf{w}_l^{[k]}}$ is computed using (2.7). The Lagrange multiplier is updated using gradient ascent,

$$\mu_l^{[k]} \leftarrow \max\left\{0, \gamma_l g\left(\hat{s}_l^{[k]}, d_l\right) + \mu_l^{[k]}\right\} \tag{4.5}$$

Algorithm 4.1 describes the acIVA technique. We randomly initialize the demixing matrices, $\mathbf{W}^{[k]}$, set $\mu_l^{[k]} = 0$ and $\gamma_l$ to a positive scalar value. At each iteration, we obtain an estimate of the sources, $\hat{s}_l^{[k]},\ k = 1, \ldots, K,\ l = 1, \ldots, L$ and estimate $\hat{\rho}_l$ and $\mu_l^{[k]}$ as given in line 8 and 9 of Algorithm 4.1, respectively. The update given in line 9 computes $g(\hat{s}_l^{[k]}, d_l)$ for all $k$ and for each value in set $\mathcal{P}$ and selects the highest value of $\rho$ from set $\mathcal{P}$ that satisfies the condition in (4.1) for all datasets. The new value of the constraint parameter, $\hat{\rho}_l$, is then used to compute the gradient, $\partial\mathcal{J}/\partial\mathbf{w}_l^{[k]}$, and update the demixing matrix as in line 9 followed by obtaining a new estimate of the sources. The process is repeated until the convergence criterion, following the one proposed in [82], is met. The adaptive tuning technique improves the estimation of the constraint source at every iteration providing a better solution as compared with using a fixed $\rho_l$ at every iteration.

**Algorithm 4.1** Adaptive constrained IVA (acIVA)

1: Define set $\mathcal{P}$ as possible values for $\rho_n^{[k]}$
2: Randomly initialize demixing matrices, $\left[\mathbf{W}^{[1]}, \ldots, \mathbf{W}^{[K]}\right]$ and set $\mu_n^{[k]} = 0, \gamma_n$ to be a positive scalar value
**for** $n = 1, \ldots, N$ **do**
  **for** $k = 1, \ldots, K$ **do**
3: Compute $\hat{\mathbf{s}}^{[k]} = \mathbf{W}^{[k]}\mathbf{x}^{[k]},\ k = 1, \ldots, K$
    **if** $n \in \{1, \ldots, L\}$ **then**
4: $\hat{\rho}_l^{[k]} = \arg\min_{\rho \in \mathcal{P}} \left[\left|\rho - \left|\epsilon(\hat{s}_l^{[k]}, d_l)\right|\right|\right]$
5: $\mu_l^{[k]} = \max\left\{0, \gamma_l g\left(\hat{s}_l^{[k]}, d_l\right) + \mu_l^{[k]}\right\}$
6: Compute $\partial\mathcal{J}\left(\mathbf{w}_l^{[k]}\right)/\partial\mathbf{w}_l^{[k]}$ using (4.4)
7: Update $\mathbf{w}_l^{[k]} = \mathbf{w}_l^{[k]} + \eta\partial\mathcal{J}\left(\mathbf{w}_l^{[k]}\right)/\partial\mathbf{w}_l^{[k]}$
    **else**
8: Compute $\partial\mathcal{J}_{\text{IVA}}/\partial\mathbf{w}_n^{[k]}$ using (2.7)
9: Update $\mathbf{w}_n^{[k]} = \mathbf{w}_n^{[k]} + \eta\partial\mathcal{J}\left(\mathbf{w}_n^{[k]}\right)/\partial\mathbf{w}_n^{[k]}$
    **end**
  **end**
**end**
10: Repeat 3 to 13 until convergence

### 4.3 Simulation results

In this section we study the performance of cIVA and acIVA in terms of incorporating multiple reference signals into the IVA framework. For this study, we vary the level of similarity measure between the groundtruth and the reference signal, $\epsilon(s_l^{[k]}, d_l)$, in order to account for choice of accurate and inaccurate reference signals, and in the variability in the choice of the reference signals. We also study the ability of cIVA and acIVA in terms of their ability to capture dataset-specific information.

### 4.3.1 Comparison of cIVA and acIVA in terms of accurate and inaccurate constraints

The goal of this experiment is to study the effect of accurate and inaccurate reference signals, and also to study the effect of varying the level of similarity between the ground truth and the reference signal, $\epsilon(s_l^{[k]}, d_l)$. In order to vary the level of similarity between the groundtruth and the reference signal, we vary the correlation between the true source, $s_l^{[k]}$ and the reference signal, $d_l$. We consider three different scenarios for this experiment,

Scenario A : The correlation between the reference signal and ground truth is high for all sources

Scenario B : The correlation between the reference signal and ground truth is high for some sources and low for remaining sources

Scenario C : The correlation between the reference signal and ground truth is high for some sources, low for some sources and zero for remaining sources

The datasets are generated as follows for each of the scenarios. We generate $M = 5$ datasets such that $\mathbf{x}^{[k]} = \mathbf{A}^{[k]}\mathbf{s}^{[k]},\ k = 1, \ldots, K$, where the mixing matrix for each dataset, $\mathbf{A}^{[k]} \in \mathbb{R}^{N \times N}$, is randomly generated with elements drawn from a normal distribution with zero mean and unit variance. The $N = 5$ SCVs are formed from $K$-dimensional SCVs of $V = 10^4$ samples. Each SCV is generated from a multivariate Laplacian distribution where the scatter matrix, $\mathbf{\Sigma}$, has a uniform-type correlation structure, as discussed in Appendix A1. For this experiment, we generate a high correlation parameter, $\psi \sim \mathcal{U}(0.7, 0.9)$, such that the sources within an SCV do not deviate much from its mean. We constrain $N = L = 5$ SCVs and the reference signal for each SCV is generated such that it is $\epsilon(s_n^{[k]}, d_n)$ correlated with the mean of the SCV. The values for $\epsilon(\cdot, \cdot)$ for each scenario are as follows,

Scenario A : $\epsilon(s_n^{[k]}, d_n) = 0.8,\ n = 1, \ldots, 5$

Scenario B : $\epsilon(s_n^{[k]}, d_n) = 0.8,\ n = 1, 2$ and $\epsilon(s_n^{[k]}, d_n) = 0.4,\ n = 3, 4, 5$

Scenario C : $\epsilon(s_n^{[k]}, d_n) = 0.8,\ n = 1$, $\epsilon(s_n^{[k]}, d_n) = 0.4,\ n = 2, 3$ and $\epsilon(s_n^{[k]}, d_n) = 0.4,\ n = 4, 5$.

We measure the performance of cIVA and acIVA in terms of jISI computed over 50 runs. The statistics of the jISI metric over 50 runs for each method is shown in Fig. 4.1. The red line indicates the median value, the bottom and top edges of the box indicate the 25th and 75th percentiles respectively, and the whiskers indicate the 99.3 percent coverage of the data. The '+' markers indicate outliers.

Fig. 4.1(a) shows the results for Scenario A, when the correlation between all the sources and corresponding reference signals is equal. The results indicate that for cIVA, jISI is higher and more variable for a lower value of the constraint parameter, indicating a weaker constraint. As we increase the value of the constraint parameter, to increase the effect of the reference signal the jISI value decreases and the result is less variable for 50 runs. The jISI is low and less varying for acIVA indicating its superior performance to estimate the true sources.

Fig. 4.1(b) shows the results for Scenario B, when the correlation between two sources and corresponding reference signals is 0.8 and for remaining three sources, it is 0.4. We observe a comparatively high median value and high variability when a constraint parameter of 0.1 is used. For a constraint parameter greater than 0.3, the median value is high and variability is less, indicating thing that cIVA starts to enforce the reference signal for the sources with $\epsilon(s_n^{[k]}, d_n) = 0.4$. The median and variability of jISI metric for acIVA is less for this scenario indicating that acIVA efficiently incorporates multiple reference signals with varying levels of correlation.

Fig. 4.1(c) shows the results for Scenario C, when the correlation between one source and corresponding reference signal is 0.8, for remaining two sources it is 0.4 and remain-

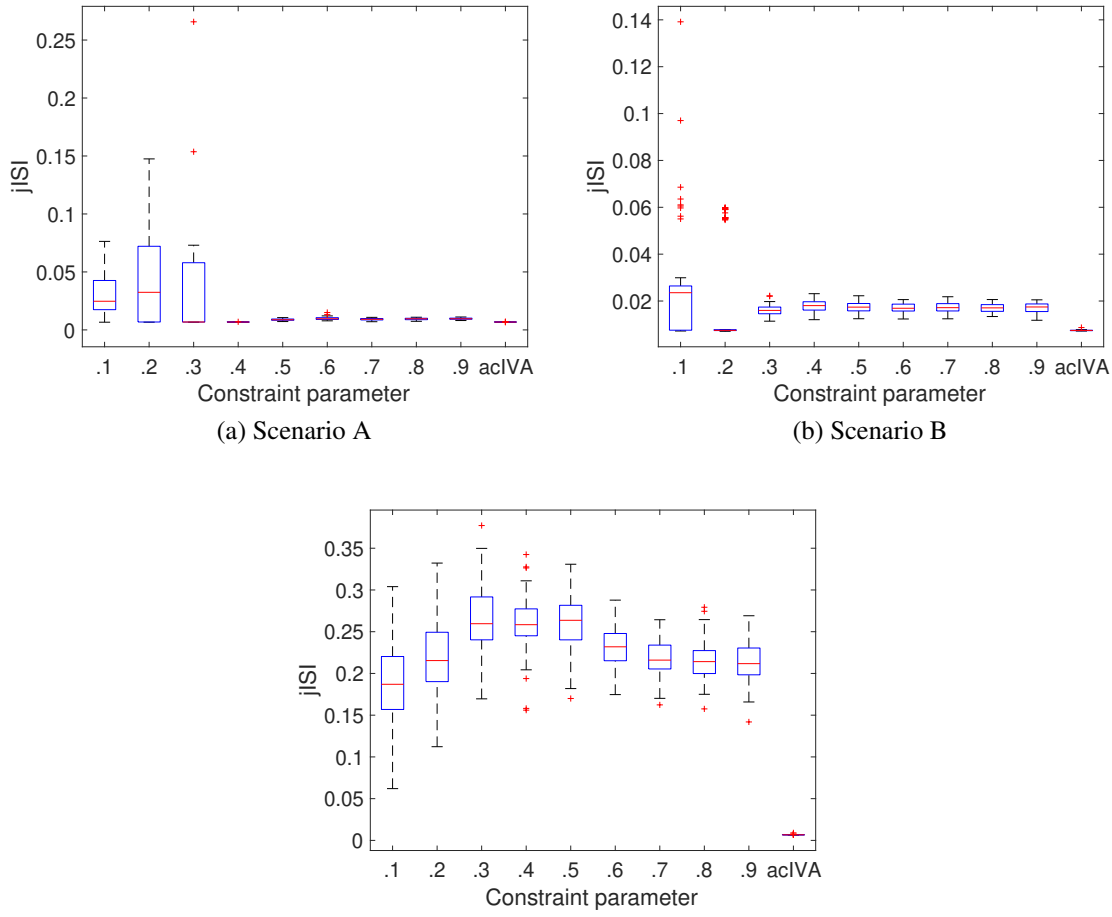


(a) Scenario A

(b) Scenario B

(c) Scenario C

FIG. 4.1. Effect of multiple reference signals with varying $\epsilon(s_l^{[k]}, d_l)$. (a) Scenario A : $\epsilon(s_n^{[k]}, d_n) = 0.8,\ n = 1, \ldots, 5$. (b) Scenario B : $\epsilon(s_n^{[k]}, d_n) = 0.8,\ n = 1, 2$ and $\epsilon(s_n^{[k]}, d_n) = 0.4,\ n = 3, 4, 5$. (c) Scenario C : $\epsilon(s_n^{[k]}, d_n) = 0.8,\ n = 1$, $\epsilon(s_n^{[k]}, d_n) = 0.4,\ n = 2, 3$ and $\epsilon(s_n^{[k]}, d_n) = 0.4,\ n = 4, 5$. The performance of acIVA is better than cIVA for all Scenarios, indicating that acIVA is not affected by the use of inaccurate constraints and efficiently incorporates a range of accurate constraints into the decomposition.

ing two sources it is 0. This scenario is a better match to real-world application where the choice of reference signals is not known, and covers a range of accurate and inaccurate constraints. For this Scenario, the jISI for cIVA is high compared to acIVA and the jISI value for cIVA obtained for Scenarios A and B. This indicates that cIVA enforces inaccurate

constraints on the decomposition, and this affects the estimation of sources corresponding to the accurate constraints as well. On the other hand, acIVA has low jISI for this scenario, indicating that it effectively incorporates inaccurate and accurate constraints into the decomposition.

### 4.3.2 Comparison of cIVA and acIVA in terms of capturing dataset-specific information

We generate $M = 5$ datasets such that $\mathbf{x}^{[k]} = \mathbf{A}^{[k]}\mathbf{s}^{[k]},\ k = 1, \ldots, K$, where the mixing matrix for each dataset, $\mathbf{A}^{[k]} \in \mathbb{R}^{N \times N}$, is randomly generated with elements drawn from a normal distribution with zero mean and unit variance. The $N = 10$ SCVs are formed from $M$-dimensional SCVs of $V = 10^4$ samples. Each SCV is generated from a multivariate Laplacian distribution where the scatter matrix, $\mathbf{\Sigma}$, has an AR-type correlation structure, as discussed in Appendix A1. We use the AR-type correlation structure in order to incorporate variability across datasets, such as in dynamic analysis of fMRI data. Among the 10 SCVs, first five are generated with medium to high second-order correlation, $\psi \sim \mathcal{U}(0.5, 0.9)$, and the remaining five with lower second-order correlation, $\psi \sim \mathcal{U}(0.2, 0.5)$. A reference signal is generated such that it has $\epsilon(s_l^{[k]}, d_l)$ correlation with the mean component of the first SCV. We consider three scenarios to test the performance of acIVA to cover the range of possibilities,

Scenario A: The correlation between the reference signal and ground truth is high, $\epsilon(s_1^{[k]}, d_1) = 0.6$

Scenario B: The correlation between the reference signal and ground truth is low, $\epsilon(s_1^{[k]}, d_1) = 0.3$

Scenario C: The correlation between the reference signal and ground truth is zero, $\epsilon(s_1^{[k]}, d_1) = 0$. This scenario accounts for use of inaccurate constraints.

For each scenario, acIVA is applied with the set $\mathcal{P}$ defined as $0.001, \ldots, 0.9$, $\gamma_n = 3$ and cIVA with fixed constraint parameter for 50 runs using the IVA-L-SOS algorithm. We tested the performance of the acIVA approach using different values of $\gamma_l$ between 1 and 1000, and observed no change in the performance. In this work, we set $\gamma_l = 3$ following [82]. For cIVA with a fixed constraint parameter, we vary $\rho$ from 0.001 to 0.9, where $\rho = 0.9$ corresponds to stronger influence of the constraint and $\rho = 0.001$ corresponds to weaker influence.

We measure the performance of the methods in terms of jISI, and dissimilarity between the constrained estimated source and ground truth. The average of the jISI metric computed over 50 runs for each method is shown in Figure. 4.2. For each scenario in Figure. 4.2, jISI obtained using regular cIVA increases when the constraint parameter is fixed to a value above the true parameter value indicating poor separation of the sources. On the other hand, acIVA demonstrates lower jISI for all three scenarios indicating good separation performance. The constraint parameter selected at each IVA iteration for the three scenarios for all 50 runs is shown in Figure 4.3. We can see that the parameter converges to the true value (indicated by '$*$') for all the scenarios. The true value is computed by plugging in the true constrained sources, $\mathbf{s}_l^{[m]}$, into the equation in line 9 of Algorithm 1. Hence, it is lower than $\rho_{true}$ for scenarios A and B. In order to verify if the proposed method accurately estimates the constrained source across time windows, we measure the dissimilarity factor, $\alpha$, between the constrained estimated source, $\hat{\mathbf{s}}_l^{[m]}$, and corresponding ground truth, $\mathbf{s}_l^{[m]}$, computed as, $\alpha = 1 - 1/M \sum_{m=1}^{M} \left|\text{corr}\left(\hat{\mathbf{s}}_l^{[m]}, \mathbf{s}_l^{[m]}\right)\right|$. A higher value of this metric indicates poor estimation of the sources. Figure. 4.4 shows the dissimilarity factor obtained using regular cIVA and acIVA for the three scenarios. The estimation of the constrained component degrades using regular cIVA when a higher constraint parameter is used whereas the proposed method has low dissimilarity factor for scenarios A and B.

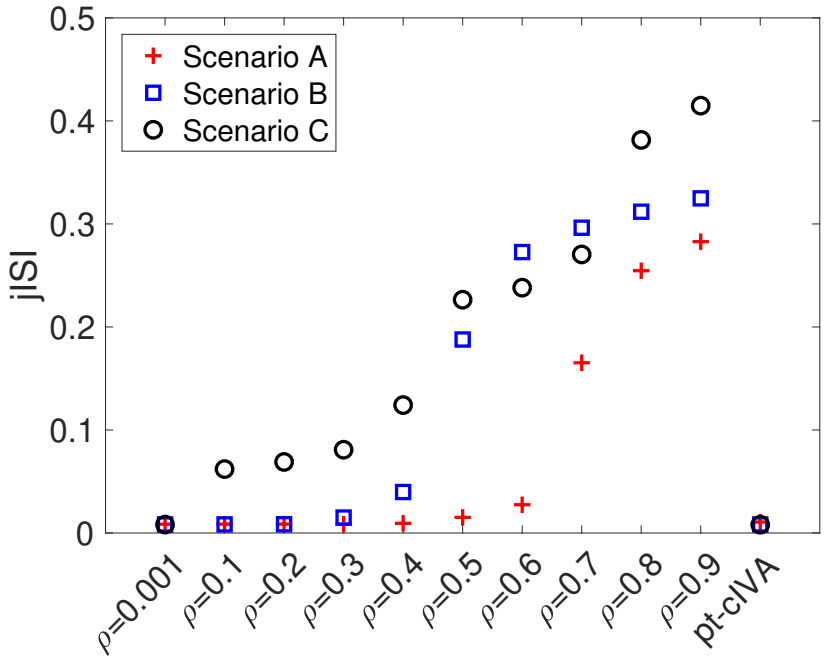


FIG. 4.2. Performance of cIVA with fixed constraint parameter varied from $\rho = 0.001, \ldots, 0.9$ and acIVA with $\mathcal{P} \in \{0.001, \ldots, 0.9\}$ in terms of jISI for the three scenarios. The performance of cIVA with fixed constraint parameter degrades if the parameter is fixed to value higher than the true constraint parameter whereas acIVA has low jISI for all three scenarios.

Noting the lower jISI and dissimilarity factor metric for lower values of $\rho$ in regular cIVA, it might be initially thought that cIVA might be preferable rather than acIVA . However, since in real world applications, one does not know the true value of the constraint parameter and whether the constraint is present or not, setting a lower value for $\rho$ might adversely affect the performance of the estimation. For scenario C, i.e., when the constraint is not present, acIVA demonstrates better performance than regular cIVA for lower values of $\rho$. At $\rho = 0.001$, which is equivalent to performing unconstrained IVA, the jISI value is similar to that of acIVA, however the dissimilarity factor is high for all scenarios, indicating a weaker influence of the constraints on the source. For scenario C the estimated constraint parameter, $\hat{\rho}_n$, is 0.001, imposing a weaker constraint on the IVA decomposition. This is

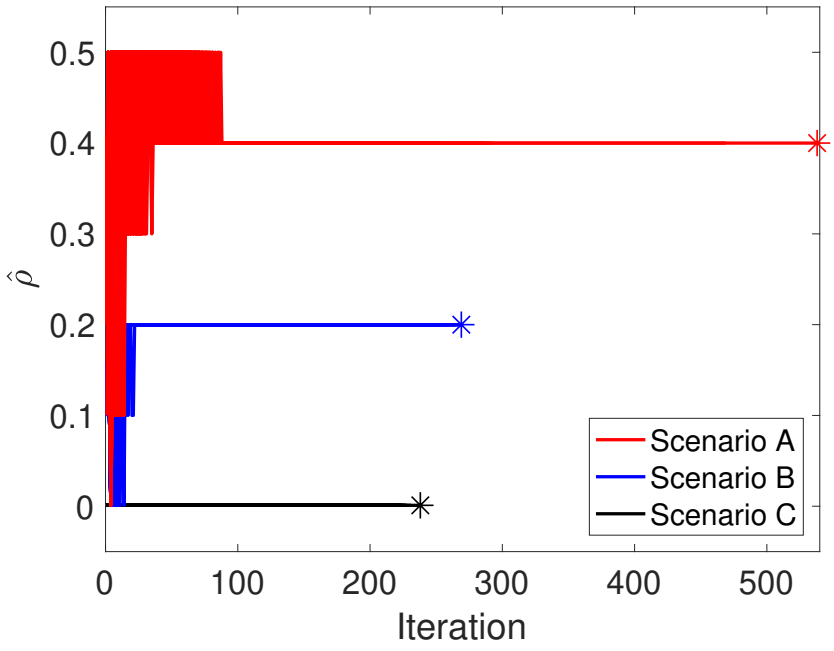


FIG. 4.3. Constraint parameter selected at every IVA iteration for all 50 runs for scenarios A, B and C. The marker '$*$' indicates the corresponding true value of $\rho$. The estimated constraint parameter using acIVA converges to the true value for all scenarios.

equivalent to performing regular IVA that holds permutation ambiguity. Thus the dissimilarity factor between the estimated source and constraint source is high even though the jISI value is low.

## 4.4 Summary

In this chapter, we describe the proposed acIVA technique, that adaptively tunes the constraint parameter to control the effect of accurate and inaccurate constraints on the decomposition. We demonstrate the performance of cIVA, which makes use of a fixed value for the constrained parameter, and acIVA in terms of varying the level of correlation between the true sources and the reference signals, and in terms of their ability to capture dataset-specific information. Our results indicate that acIVA performs better than cIVA for a range of scenarios, increasing our confidence to use it on the analysis of large-scale fMRI

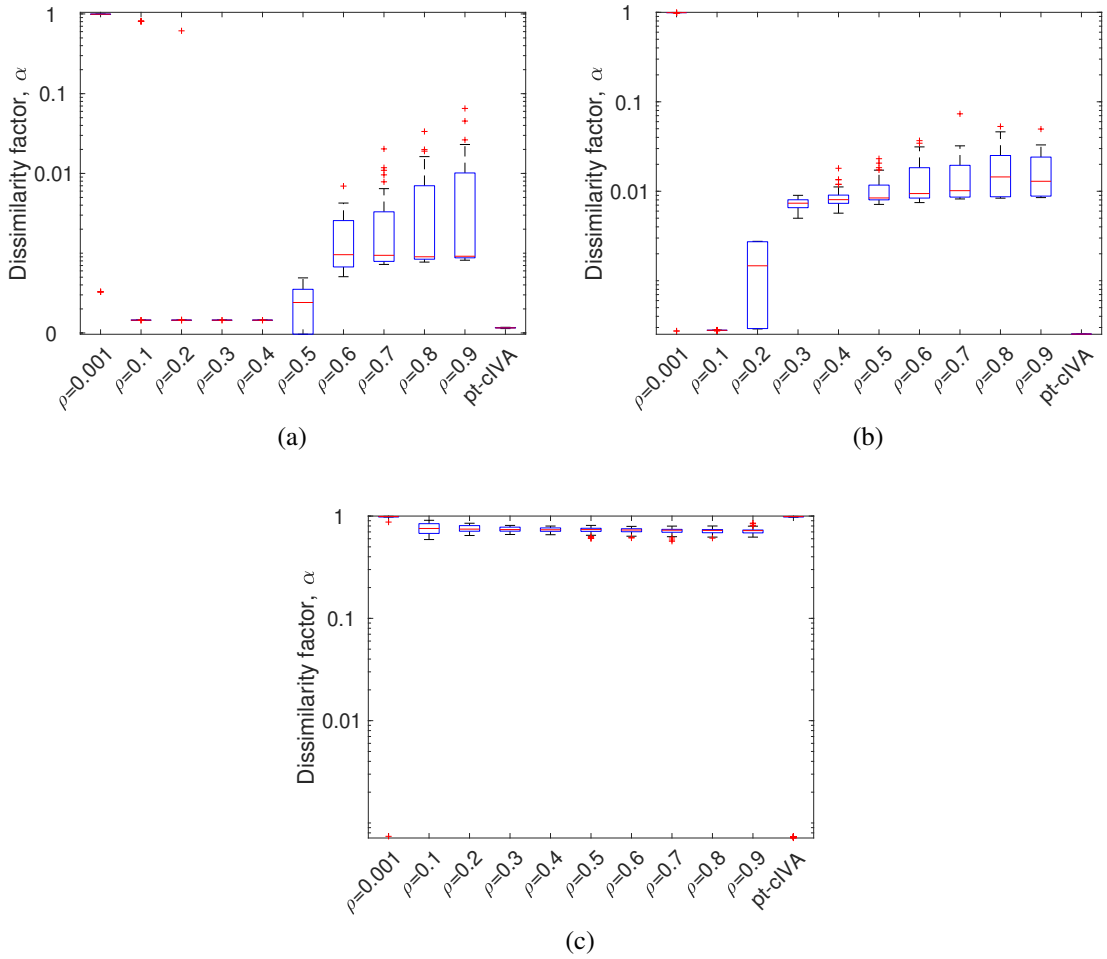


FIG. 4.4. Performance of cIVA with fixed constraint parameter varied from $\rho = 0.001, \ldots, 0.9$ and acIVA with $\mathcal{P} \in \{0.001, \ldots, 0.9\}$ in terms of dissimilarity factor for (a) Scenario A, (b) Scenario B and (c) Scenario C. For each box, the horizontal red line indicates the median, the top and bottom edges indicate the 75th and 25th percentiles, respectively, the whiskers show the extreme points not considered as outliers and the '+' symbol indicate outliers. The dissimilarity factor of the constrained component is low for acIVA whereas it increases using regular cIVA when a higher constraint parameter is used.

data and to extract time-varying spatio-temporal patterns from fMRI data.

In the next chapter, we investigate the performance of acIVA on high dimensional datasets using a simulation data and real-world resting state fMRI dataset.

Chapter 5

# EXTRACTION OF FUNCTIONAL NETWORKS FROM LARGE SCALE FMRI DATA

In this chapter we discuss the potential use of applying acIVA on high dimensional datasets. We study the performance of acIVA and standard IVA using simulated and real-world resting-state fMRI dataset.

## 5.1 Introduction

Neuroimaging analysis has allowed for the identification of distinguishing characteristics of the human brain based on gender, age, addiction, and different brain disorders. Neuroimaging modalities such as functional magnetic resonance imaging (fMRI), structural MRI, magnetoencephalography, and positron imaging tomography, have proven to be effective in capturing different properties of the brain at a wide range of spatial and temporal resolutions. With the availability of such effective tools for capturing brain activity, the use of datasets acquired from more number of subjects has increased in order to obtain robust and reliable estimates. Most joint blind source separation methods become increasingly complex when the dimensionality of the model increases, causing estimation of unreliable solutions [67, 83]. Few approaches to mitigate the high dimensionality issue involves extraction of per subject features summarizing the overall temporal activity as in [84, 85], transformation of high-dimensional datasets to a lower dimensional feature space

such as in group independent component analysis (gICA) [9, 10], multisubject dictionary learning [86], tensor decompositions [83], or using prior information such as regions-of-interest (ROI) or a task paradigm in a regression type analysis to analyze a single subject at a time. Some approaches adopt on a divide-and-conquer approach that divide the high dimensional problem into a series of smaller dimensional problems and carefully combine the results [87, 88]. Although these approaches have successfully identified relevant biomarkers, they are prone to loss of information, sensitive to ROI selection and do not exploit the complimentary information across multiple subjects.

In this chapter, we study the potential use of acIVA to overcome the high dimensionality issue for the case when the sources have low correlations across datasets. We consider this case, as it is a better match to the fMRI sources.

## 5.2 Application to simulated data

In order to study the performance of acIVA over regular IVA on high dimensional datasets, we generate simulated datasets similar to the set-up described in Section **??**. We vary the number of datasets, $K$, from 2 to 60, and number of sources, $N$, from 40 to 85, with fixed sample size $V = 1000$. The SCVs are generated from a multivariate Laplacian distribution with a covariance structure, $\mathbf{\Sigma} = \mathbf{Q}\mathbf{Q}^T$, $q_{ij} = \mathcal{N}(0.1, 0.3)$. This structure results in moderately low correlated sources that is a good match to the fMRI sources. The fMRI sources are known to have a super-Gaussian distribution [8], such as the multivariate Laplacian distribution, and these sources demonstrate low to moderate level of correlation across datasets, see Appendix A3. The sources are linearly mixed using a randomly generated mixing matrix for each dataset to obtain the observation set, $\mathbf{X}^{[k]}$. We generate three different observation sets by randomly generating the mixing matrices and sources for each set. We obtain 20 runs of regular IVA and acIVA using the IVA-L-SOS algorithm. For

acIVA half of the total number of sources are used as constraints, $L = N/2$, $\gamma_n = 3$ and the set $\mathcal{P}$ is defined as $0.1, \ldots, 0.9$. The reference signal for the constraint source is obtained by computing the mean of the SCV. We measure the performance of the two methods using jISI, which measures the estimation of the whole demixing matrices, and spatial correlation, which measures the estimation of the individual sources of interest. For regular IVA we align the estimated sources with respect to the original sources, whereas for acIVA no additional alignment step is required to align the constrained sources. The average of the jISI metric and spatial correlation of the constrained sources across 20 runs and three observation sets for IVA and acIVA is shown in Fig. 5.1(a) and Fig. 5.1(b) respectively.

From Fig. 5.1 we observe that IVA performance improves with increase in number of datasets upto a certain limit for different numbers of sources. This range can be defined as the optimal range in which there are sufficient samples available for IVA to accurately estimate the underlying parameters. In this range, however, the application of acIVA does not improve the performance compared with IVA, indicating that it is the lower bound on performance for the fixed choice of algorithm and number of samples. The range of optimal performance, however, becomes tighter as we increase the number of sources, after which we observe a degradation in performance due to the effect of high dimensionality. The application of acIVA in this high dimensional range however shows a significant improvement in performance, indicating that the use of prior information is providing reference to the search for an optimal solution in IVA.

### 5.3 Application to real fMRI data

We use a large-scale resting-state fMRI dataset acquired from 327 subjects (164 female and 163 male) at the Mind Research Network [56]. All images were collected on a 3-Tesla Siemens Trio scanner with a 12-channel radio frequency coil. T2*-weighted func-

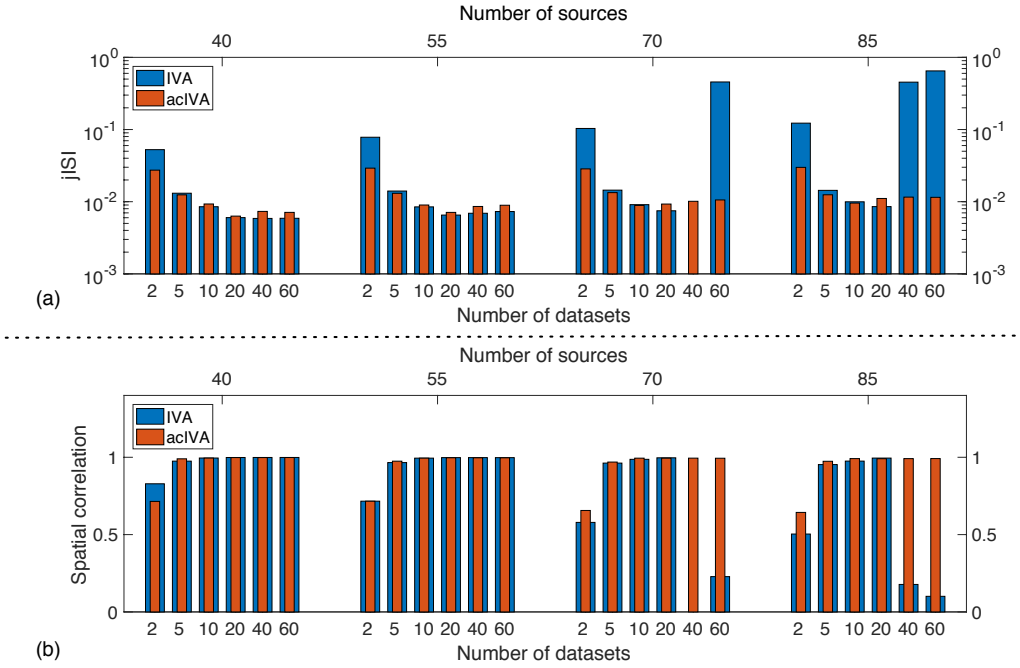


FIG. 5.1. Performance of IVA and acIVA in terms of jISI (a) and spatial correlation (b), with respect to number of sources, $N$ and number of datasets, $K$. The number of sources, $N$, is varied from 40 to 85, the number of datasets, $K$, is varied from 2 to 60, and the number of samples ,$V$, is fixed at 1000. For acIVA, half of the components are constrained, *i.e.*, $L = N/2$. For $K = 40$ and $N = 40$ none of the IVA runs converged in 1024 iterations. (a) The jISI is averaged across all converged runs for both acIVA and IVA. We observe degradation in performance of IVA for higher number of datasets, across different values of $N$ whereas acIVA provides improvement in performance compared to IVA. (b) The spatial correlation of the constrained sources with groundtruth is averaged across all converged runs. We see that acIVA was able to recover the constrained sources in high-dimensional scenarios, however IVA showed poor performance.

tional images were acquired using a gradient-echo EPI sequence with TE = 29 milliseconds, TR = 2 seconds, flip angle = 75°, slice gap = 1.05 millimeters (mm), slice thickness = 3.5 mm, field of view = 240 mm, matrix size = 64 × 64, voxel size = 3.75 mm × 3.75 mm × 4.55 mm. The participants were asked to keep their eyes open during the scan and stare passively at a fixation point for 5 minutes, 4 seconds (152 volumes). Any additional volumes were discarded to match data quantity across participants. Images were realigned

using INRIalign, and slice-timing corrected using the middle slice as the reference frame. Data are then spatially normalized into the standard Montreal Neurological Institute (MNI) space, resliced to 3 mm $\times$ 3 mm $\times$ 3 mm voxels, and smoothed using a Gaussian kernel with a full-width at half-maximum (FWHM) of 10 mm. Masking using the group ICA for fMRI toolbox (GIFT) was performed on each volume to remove the non-brain voxels and vectorized, resulting in an observation set for the $k$th subject as, $\bar{\mathbf{X}}^{[k]} \in \mathbb{R}^{152\times 58541}$.

The knowledge of the desired outcome is available is most applications and in fMRI analysis, the desired outcome could be the structure of the functional networks, the nature of the time course, or subject class information to enhance the estimation of group-differentiating features [82]. In resting-state fMRI data, the nature of the time course is not known, and using subject class information is a complicated task for the IVA model in Fig.2.5, hence in this work we incorporate the structure of functional networks as reference signals.

The reference signals for acIVA are extracted using the group ICA for fMRI toolbox (GIFT). The model order, that determines the dimension of the signal subspace, is obtained as the mean plus one standard deviation of the orders computed across all subjects. The mean and standard deviation of the orders estimated using the entropy rate based order selection by finite memory length model (ER-FM) [89], which incorporates sample dependence into the information theoretic criteria, is 79.56 and 8.98 respectively. We select the final order as 90. ICA using the entropy-rate bound minimization algorithm [52, 53] is applied on the subject datasets to estimate 90 components. We select $L = 42$ group-level independent components corresponding to functionally relevant resting-state networks by visual inspection and these components are used as reference signals in acIVA.

We perform acIVA on male and female group separately using the group ICA components as reference signals. Each subject's data is dimension reduced using principal

component analysis in order to remove noise from the data and $N = 55$ uncorrelated components are used to form a dimension reduced dataset, $\mathbf{X}^{[k]} \in \mathbb{R}^{55\times 58541}$ for each subject. Five runs of acIVA using the IVA-L-SOS algorithm are obtained with different initializations and the best run is selected using the cross jISI method, which is an extension of the method proposed in [63] to multiple datasets. The estimated demixing matrices of the selected run are used to compute the sources. The estimated sources from the selected run and the corresponding reference components are shown in Appendix A2.

### 5.3.1 Identification of associated networks

The use of reference signals enables the identification of functionally associated networks due to the adaptive nature of acIVA that allows for flexible estimation of the sources. It naturally groups the regions that have correlated and anti-correlated relationship with the reference signal. The default mode network (DMN) is a large-scale brain network of interconnected brain regions that form hubs and subsystems. It is commonly known to be activated when the person is in the resting-state with thoughts pertaining to oneself, others, the past and future, and hence is one of the widely explored network in various disorders. The core functional hubs of DMN are located in the medial prefrontal cortex (mPFC), posterior cingulate cortex (PCC), Precuneus and angular gyrus (AG). The acIVA method identified the core default mode network in IC 21, when only mPFC is used as the reference signal, as shown in Fig. 5.2. This IC also shows activation in the regions of the central executive network namely the dorsolateral prefrontal cortex (dlPFC) and the posterior parietal cortex (PPC), which has shown anti-correlation with the default mode network [90]. Similarly for IC 22, the ventrolateral prefrontal cortex (vlPFC) is extracted along with posterior DMN (PCC+AG) using acIVA for a corresponding reference signal showing activation in the AG. For IC 23, the anterior cingulate cortex (ACC) and regions are extracted along Precuneus. The ACC and INS regions form the salience network that

plays a critical role in switching between DMN and CEN [90, 91]. The reference signal in IC 24 consists of the regions associated with the dorsal medial subsystem [92], namely the temporoparietal junction (TPJ), lateral temporal cortex (LTC), temporal pole (TempP). The dorsal medial subsystem also consists of dmPFC which is extracted using acIVA alongwith the reference signal. Precuneus and anterior mPFC (amPFC) have shown strong association with the dorsal medial subsystem and act as functional hubs for information transfer across the subsystem [92].

### 5.3.2 Performance of acIVA and gICA in terms of preserving subject-variability

In this section, we study the performance of acIVA in terms of its ability to preserve subject-specific information using two techniques, namely, 'variability maps' and capturing gender differences in spectral power, and compare its performance with the widely-used gICA technique for fMRI analysis [9, 10]. The acIVA technique computes subject-specific spatial maps and time courses, where the dependent components are grouped together to form an SCV. In order to obtain subject-specific spatial maps and time courses for gICA, the group level ICs/reference signals are back-reconstructed using PCA-based back-reconstruction [8].

The variability map for each component is obtained as the standard deviation at each voxel computed across subjects. The results for the variability maps for the components associated with the DMN are shown in Fig. 5.3. The maps from acIVA demonstrate high standard deviation across subjects, at voxels corresponding to meaningful regions in the DMN and dorsal medial subsystem, whereas gICA demonstrates lower standard deviation at these voxels. This suggest that since gICA performs a significant dimensionality reduction step in the group-level PCA stage, most of the variability associated with individual subjects is lost. Hence, the subject-specific components from gICA are mostly centered around the group ICs with a low standard deviation. However, since acIVA does not per-

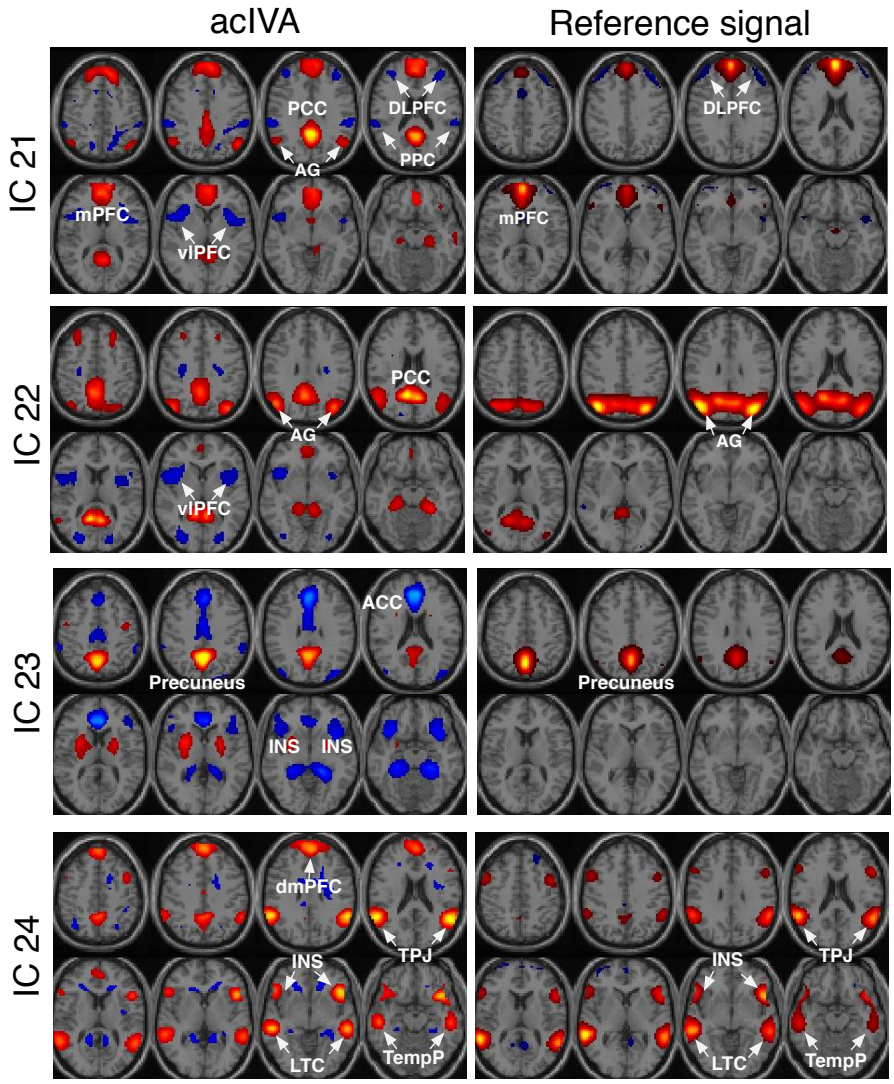


FIG. 5.2. Components estimated using acIVA and corresponding reference signal, which are the group-level components of GICA. Our results indicate that the proposed acIVA technique naturally groups together associated networks, *e.g.*, acIVA identified the whole default mode network (PCC, mPFC, AG) when only the anterior DMN (mPFC) was used as the reference signal. (Abbreviations: medial prefrontal cortex (mPFC), anterior cingulate cortex (ACC), posterior cingulate cortex (PCC), angular gyrus (AG), dorsolateral prefrontal cortex (dlPFC), posterior parietal cortex (PPC), ventrolateral prefrontal cortex (vlPFC), insular (INS), dorsal medial prefrontal cortex (dmPFC), temporoparietal junction (TPJ), lateral temporal cortex (LTC), temporal pole (TempP).

form the group-level dimensionality reduction step, it is able to capture the variability associated with each subject resulting in a higher standard deviation.

We compare the performance of acIVA and gICA in terms of capturing gender differences in spectral power. We obtain the component power spectra for all subjects using the time courses from acIVA and gICA, and identify differences using a two-sample $t$-test between male and female group at each frequency level. The components showing significant difference ($p < 0.05$, corrected) are shown in Fig. 5.4. Significantly higher spectral power is observed in the male group at low frequencies (< 0.05 Hz) in few motor (ICs 5), frontal (IC 22) and DMN (IC 33) components. High spectral power in the motor (IC 5) and frontal component (IC 22) is also observed in a similar study [56]. Significantly higher spectral power is observed in the female group at higher frequencies (0.05 to 0.15 Hz) in the frontal component (IC 22) and visual component (IC 30). In general, our results show high spectral power in the female group in the frequency range 0.05 to 0.15 Hz across the motor, parietal, frontal, visual, DMN and cerebellum components, although not significant.

## 5.4 Discussion

In this work, we present the acIVA algorithm that efficiently incorporates prior information regarding the sources or the columns of the mixing matrix, into the IVA decomposition and demonstrate its potential use in the analysis of large-scale datasets. Our results from Fig. 5.1 indicate that acIVA provides reliable and meaningful estimation of the underlying sources when there are insufficient samples available with respect to the number of sources and datasets. Although acIVA demonstrated superior performance than regular IVA for higher number of datasets, it is not impervious to the effect of high dimensionality. As the number of dimensions approaches the number of samples or in the sample-poor regime, where the number of samples are less than the number of dimensions,

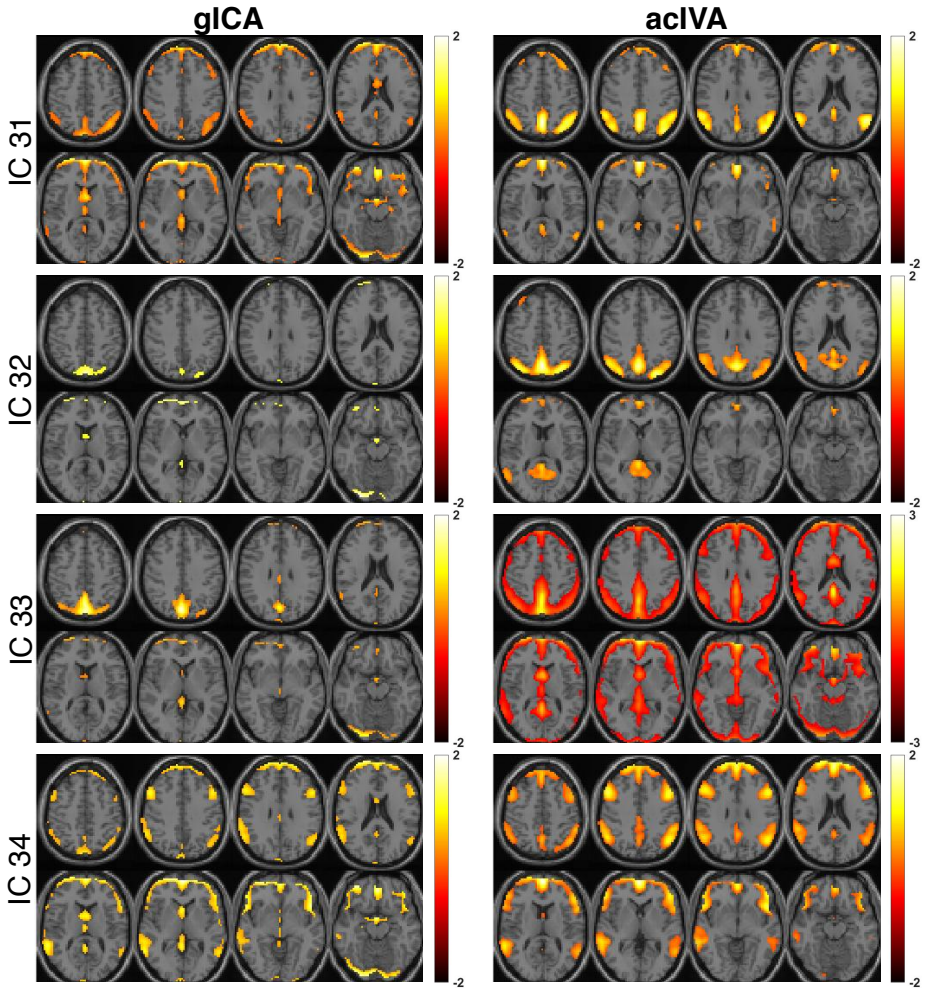


FIG. 5.3. Variability maps (threshold at 1) for acIVA and gICA. High standard deviation is observed at voxels corresponding to the DMN and dorsal medial subsystem for acIVA as compared to gICA.

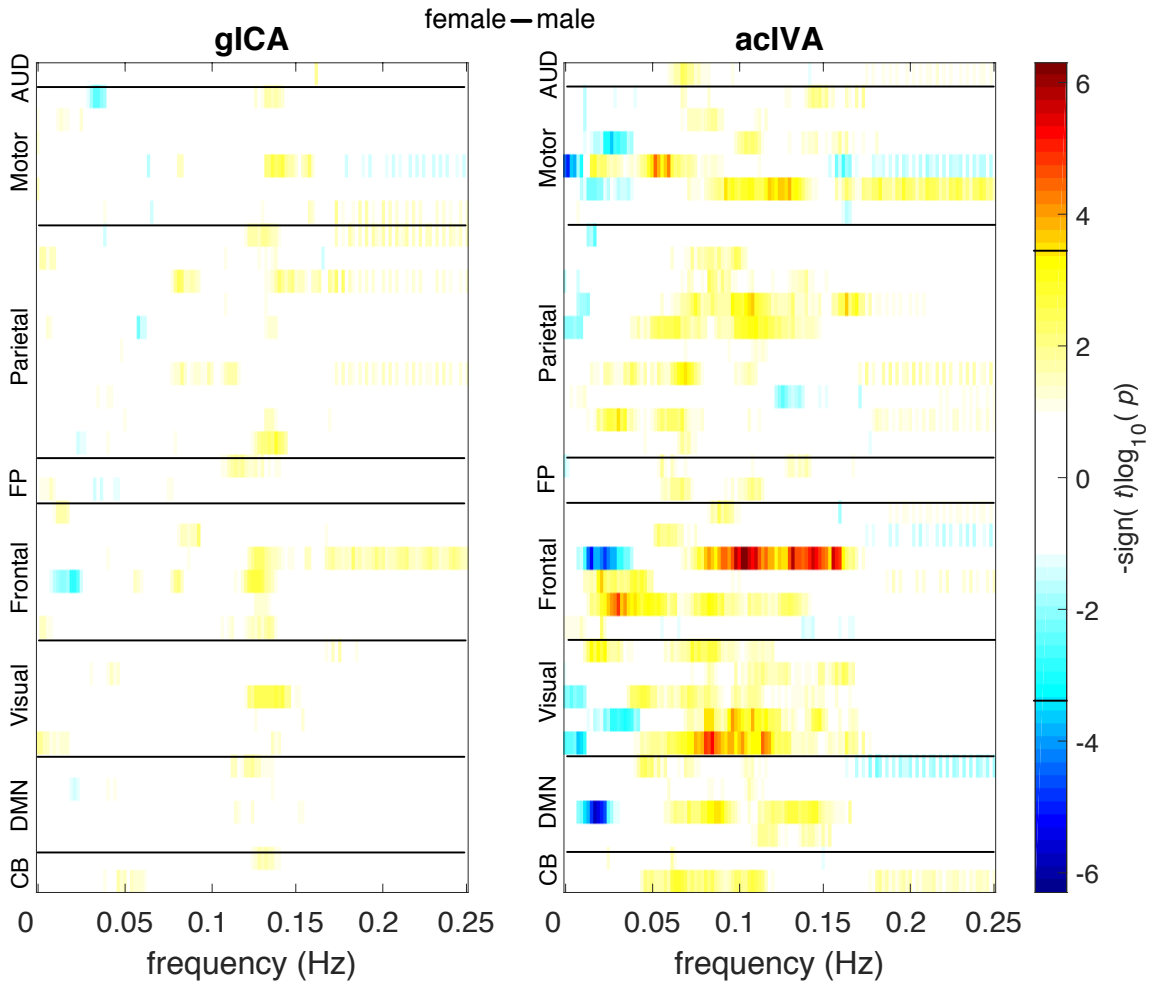


FIG. 5.4. Frequency range that demonstrates significant ($p < 0.05$) difference between male and female group, displayed as $-\text{sign}(t)\log_{10}(p)$. Hot colors demonstrate higher spectral power in female group whereas cold colors indicate high spectral power in male group. The line on the colorbar indicates the FDR-corrected threshold ($p = 0.05$) for significance. Higher spectral power is observed in the male group at low frequencies (< 0.05 Hz) for the motor, frontal, visual and DMN components, whereas females show higher spectral power at high frequencies (0.05 to 0.15 Hz). The acIVA technique better captures gender differences than gICA technique, indicating its ability to preserve subject variability.

the performance of acIVA is expected to drop, as observed in Fig. 5.1 at $N = 85$ and $K = 160$. However, this drop in acIVA performance is observed at a more extreme case as compared with regular IVA. Additionally, the jISI results from Fig. 5.1(a) show that the performance of acIVA is slightly affected in the sufficient sample regime for some cases, *e.g.*, $N = \{40, 55\}$, $K = \{40, 60\}$. The spatial correlation of the constrained sources for the corresponding points demonstrates similar performance as IVA, indicating that the estimation of the unconstrained sources is penalized to some degree. This effect can be reduced by incorporating prior information regarding the remaining sources. It should also be noted that the performance of acIVA depends on the number of constraints, i.e., acIVA performance might improve further if prior information regarding all the sources is incorporated.

Data-driven techniques are most popular in the analysis of fMRI data due to its flexible nature that allows for identification of natural relationships that were not derived a-priori [7, 8]. On the other hand model-driven methods such as region-of-interest based methods make stronger assumptions regarding the nature of the decomposition, and are robust to noise and other artifacts. Typically model-driven methods extract associated regions from resting-state fMRI data by identifying voxels that have correlated activation patterns with a pre-defined region-of-interest or a seed voxel. These methods usually outperform the data-driven techniques only when prior information is accurate [74]. Data-driven methods, on the other hand, are flexible, but might result in splitting of the correlated regions into multiple components for a high model order as seen in Fig. 5.2. A comparison of data-driven, model-driven and semi-BSS method on task-related fMRI data demonstrated robust performance of semi-blind ICA in the presence of noise and when the prior information is not completely accurate [74]. The acIVA technique provides a balance between data-driven and model-driven techniques, and takes advantage of the robustness properties of model-driven methods and flexible nature of data-driven techniques. The use of adaptive

parameter tuning technique allows for flexibility for the associated regions to interact and does not enforce the sources to be exactly similar to the reference component, as shown in Fig. 5.2.

## 5.5 Summary

In this chapter, we demonstrated the potential use of acIVA on high dimensional datasets using simulated example. We showed that acIVA demonstrates superior performance than IVA in terms of jISI for higher number of datasets and sources, for a fixed set of samples. We measured the performance of acIVA and IVA in terms of spatial correlation between the estimated source and ground truth and observe that acIVA results in high correlation values. This indicates that incorporating reference signals into the IVA framework significantly improves the estimation of the underlying sources, in high dimensional scenarios. We also applied acIVA on a large scale fMRI data to extract functionally relevant networks. Our results indicate that the acIVA extracts meaningful functional networks from large-scale fMRI data while successfully preserving subject variability, while standard IVA did not converge on this dataset. It identified the default mode network when only parts of the network are used as reference signals. It also identified hubs within the default mode network when regions of the dorsal medial subsystem are used as reference signals. The acIVA technique also captures gender differences in spectral power, where higher spectral power is observed in males at low frequencies, and higher spectral power is observed in females at high frequencies in the motor, attention, visual and default mode networks.

In the next chapter, we talk about our proposed method to extract time-varying spatio-temporal patterns from large-scale fMRI data. The proposed method exploits variability in both spatial and temporal domains using a sliding-window based acIVA framework.

Chapter 6

# EXTRACTION OF TIME-VARYING SPATIO-TEMPORAL PATTERNS FROM LARGE-SCALE FMRI DATA

## 6.1 Introduction

Dynamic functional network connectivity (dFNC) analyzes the time-varying associations among different regions of the brain and has been widely studied in order to identify correlations between functional changes and cognitive abilities ([15, 93, 94]). In order to identify these functional patterns of different brain regions, conventional methods identify groups of temporally coherent voxels, referred to as spatial maps, and their corresponding activation patterns, referred to as time courses ([95]). Followed by the estimation of time courses, a sliding window is applied on the time courses that divides it into consecutive windows and an analysis on the time points within each window is performed ([19]). The analysis of dFNC patterns depends on the length of the window, where the use of a longer window length increases the risk of averaging the temporal fluctuations of interest resulting in false negatives ([96]), and the use of a shorter window length has too few samples for a reliable computation of correlation ([97]), resulting in the temporal variations to capture spurious fluctuations and increasing the risk of false positives ([15, 98, 99]). Previous studies have shown that a window length between 30-60 seconds successfully estimates temporal fluctuations in resting-state functional magnetic resonance imaging (fMRI) data ([96]),

and for most cases higher window lengths do not alter the results significantly ([100–102]). However, there is a lower bound in being able to capture fluctuations due to the limited number of samples, limiting the use of dFNC analysis in the temporal domain.

Conventional methods also estimate the time-varying FNC patterns of the spatial networks while assuming that the spatial network itself is stationary. However, studies have shown that changes in the FNC patterns imply changes in the spatial networks ([103]). Hence, spatio-temporal dFNC analysis relaxes the assumption of stationarity in both the spatial and temporal domain, and provides a more general framework for capturing time-varying FNC patterns ([32, 33, 104]). The availability of higher number of samples in the spatial domain also guarantees reliable estimation of functional correlations ([97]), thus providing a promising direction for the use of spatial domain for dFNC analysis. However, the methods used to extract time-varying spatio-temporal patterns face few challenges. Region of interest based methods use pre-defined resting-state networks causing the estimated functional connectivity to be sensitive to network selection. Dynamic mode decomposition, a spatio-temporal modal decomposition technique, requires significant dimension reduction that may restrict the method to estimate fewer dynamic components ([33]). In this work, we propose the use of IVA for capturing time-varying spatio-temporal patterns.

## 6.2 IVA for capturing dynamic spatio-temporal patterns

Independent vector analysis (IVA) provides a general and flexible framework to spatio-temporal dFNC analysis and estimates window-specific time courses and spatial maps. Due to its flexible nature, it has been successfully applied to fMRI data to captue variability in spatial networks of patients with schizophrenia and healthy controls [104]. The method proposed in [104] divides each subject's data is divided into $M$ overlapping windows of length $L$ resulting in a total of $KM$ datasets, where $K$ is the number of subjects,

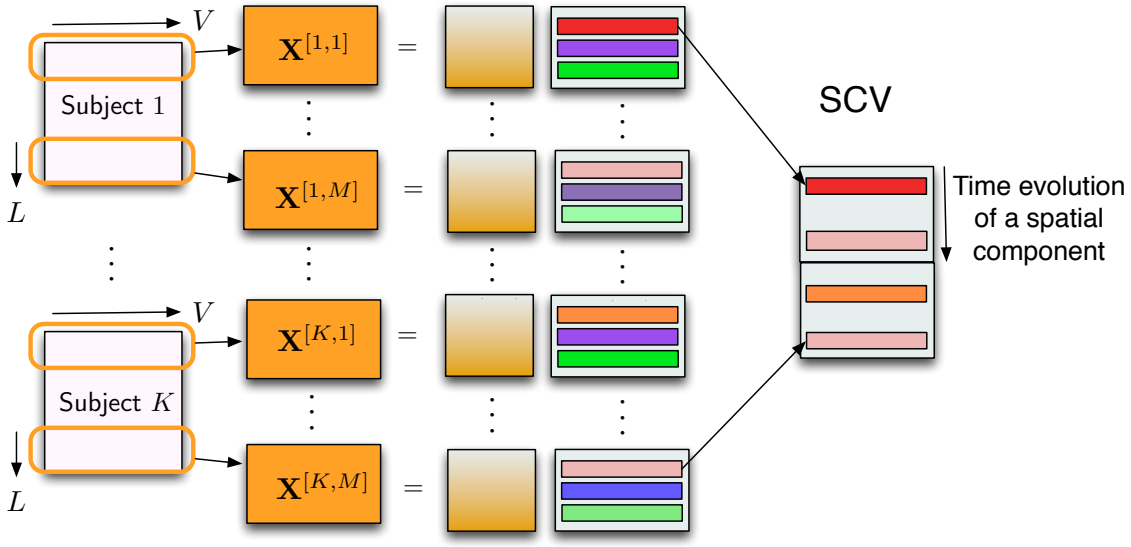


FIG. 6.1. Sliding-window based IVA technique for capturing time-varying spatio-temporal patterns from fMRI data. Each subject's data is divided into $M$ windows of length $L$ resulting in a total of $KM$ datasets, where $K$ is the number of subjects. Performing IVA on these $KM$ datasets, results in window-specific time-courses and spatial maps, which are maximally independent within each window and dependent across windows and subjects. An SCV groups the dependent sources from $KM$ datasets together and represent the temporal evolution of a spatial region for each subject.

as shown in Fig 6.1. Performing IVA on these $KM$ datasets, results in window-specific time-courses and spatial maps, which are maximally independent within each window and dependent across windows and subjects. An SCV groups the dependent sources from $KM$ datasets together and represent the temporal evolution of a spatial region for each subject.

While this approach assumes variability in both spatial and temporal domain, and successfully captures the dynamics of the spatial networks, it is limited to a small number of subjects (20 subjects analyzed in [104]) due to effect of high dimensionality to which IVA is susceptible. The flexibility of IVA comes at a cost that for a fixed number of samples, its performance degrades with the increase in number of datasets and number of sources since it requires estimation of high-dimensional probability density functions, as discussed in Chapter 3.

In this work, we develop a two-stage procedure while addressing two important points: (1) use of a flexible model, like IVA, that captures variability in both spatial and temporal domain, and (2) address the performance degradation with high dimensionality in IVA, while preserving the variability in both domains for application to large scale fMRI data. One way to reduce the effect of high dimensionality in IVA is through the use of reference signals to limit the size of the solution space, using acIVA. The two-stage procedure includes extraction of a common stationary representation of the spatial maps and using these as reference signals in acIVA to capture their variation in the temporal and spatial domain. The use of acIVA preserves variability across time windows and reduces the undesirable effects of high dimensionality by enabling analysis of each subject at a time.

## 6.3 Implementation

In this section, we present the methodology to capture time-varying spatial and temporal components using acIVA. This method extracts steady-state representation of functionally relevant components from all subjects using gICA followed by performing acIVA on each subject to obtain the time-varying representations of these components as shown in Figure 6.2.

### 6.3.1 Extraction of reference signals

The proposed implementation provides flexibility in the choice of the method used to extract the exemplar components. The two most predominant methods used to extract RSNs are seed-based techniques and spatial ICA. Seed-based methods extract voxels that exhibit temporal dependencies with respect to a user-defined seed voxel or region of interest (ROI) [105–111]. Spatial ICA is a data-driven technique that decomposes the observed data into maximally independent spatial maps that correspond to regions with similar time courses [112–114]. Matrix decomposition techniques such as multiset canonical correla-

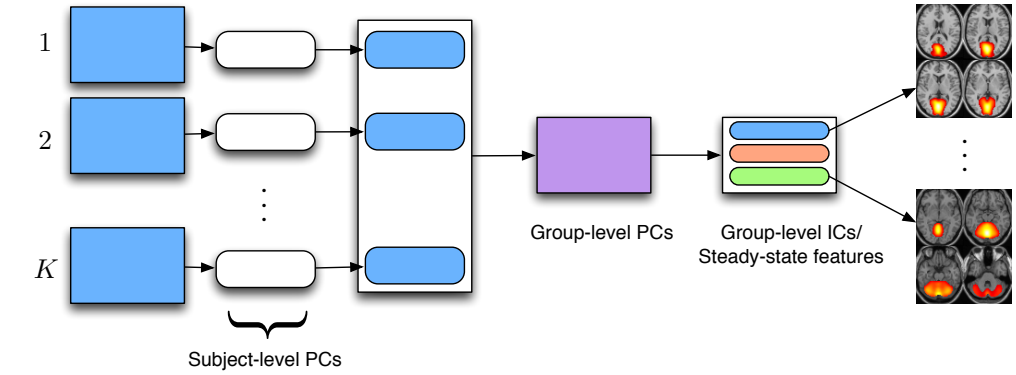


(a) Extraction of reference signals: Group ICA

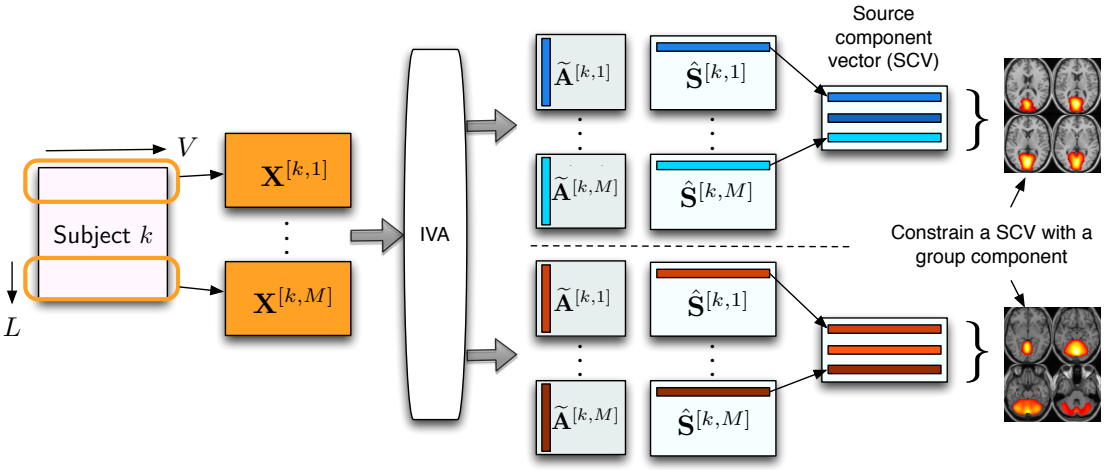


(b) Capture dynamic spatio-temporal patterns of reference signals: acIVA

FIG. 6.2. The two-stage method for obtaining time-varying spatial networks and corresponding time courses. (a) Reference signals are obtained using gICA from all subjects. These signals represent the stationary representation of the brain regions. (b) Each subject data is divided into windows and acIVA is applied on the windowed datasets with features extracted from gICA used as reference. The sliding-window acIVA framework extracts the time-varying representation of the reference signals, which is reflected in an SCV.

tion analysis (MCCA) [115], population value decomposition [116], nonnegative common feature extraction (NCFE) [117], shared dictionary learning [118], joint and individual variation explained (JIVE) [119] and common orthogonal basis extraction (COBE) [120] extracts common and individual features from multiple subjects. Templates of resting-state networks of interest that are pre-defined based on extensive studies of resting-state

fMRI data can be used as exemplars. Sparsity-learning methods such as dictionary learning ([86]) or sparse ICA ([121]) can be used to extract more focal spatial components. One of the widely used methods for extraction of components from multiple subjects is group independent component analysis (gICA) that estimates a common subspace consisting of the most informative components across all subjects ([9, 10]). In this work, we perform gICA on all subjects to extract exemplars of resting-state networks using the group ICA for fMRI toolbox (GIFT). gICA performs a subject-level principal component analysis (PCA) to extract the signal subspace for each subject followed by a group-level PCA on the principal components (PCs) from all the subjects. In order to exploit higher order statistics, it performs independent component analysis (ICA) on the group-level PCs. The details of gICA are described in Section 2.1.3.

### 6.3.2 Sliding-window based acIVA

In the second stage, we divide each subject's data into $M$ windows of length $L$ with an 50% overlap yielding a total of $MK$ windows. Considering all the $MK$ windows in the analysis results in IVA to model $MK$-dimensional SCVs from the fixed $V$ samples. However, as discussed, the performance of IVA degrades with a large number of datasets and sources for a fixed number of samples. Thus, we perform a subject-level analysis to mitigate the high dimensionality issue by modeling a $M$-dimensional SCV instead of a $MK$-dimensional SCV by performing a subject-level IVA, where the windowed data from each subject defines a dataset. Using this setup, IVA also takes advantage of source dependence across windows since the spatial maps are expected to change smoothly across windows, thus aligning the components across windows. The $N$ reference signals, $\mathbf{d}_n,\ n = 1, \ldots, N$, obtained from gICA are used as constraints in acIVA to constrain the first SCVs for each subject. The acIVA technique we introduced in Chapter 4 enables each window to have a different level of correlation with the constraint and setting a fixed value for the constraint

parameter can deteriorate the estimation of the SCVs as shown in the simulation examples in Chapter 4.

### 6.4 Identification of resting-state dynamics

We use a large-scale resting-state fMRI data obtained from the Center for Biomedical Research Excellence (COBRE), which is available on the collaborative informatics and neuroimaging suite data exchange repository (http://coins.mrn.org/dx) [60], to capture the variability using the proposed pipeline. This resting-state fMRI data includes $K = 179$ subjects: 91 healthy controls (HCs) (average age: $38 \pm 12$) and 88 patients with schizophrenia (SZs) (average age: $37 \pm 14$). For this study, the participants were asked to keep their eyes open during the entire scanning period. The resting fMRI data were obtained using a 3-Tesla TIM Trio Siemens scanner with TE = 29 ms, TR = 2 s, flip angle = 75°, slice thickness = 3.5 mm, voxel size = $3.75 \times 3.75 \times 4.55$ mm$^3$ and slice gap = 1.05 mm. Image scans were obtained over five minutes with a sampling period of 2 seconds yielding 150 timepoints per subject. We removed the first 6 timepoints to address T1-effect and each subject's image data was pre-processed including motion correction, slice-time correction, spatial normalization and slightly re-sampled to $3 \times 3 \times 3$mm$^3$ yielding $53 \times 63 \times 46$ voxels. We perform masking on each image volume to remove the non-brain voxels and flatten the result to form an observation vector of $V = 58604$ voxels, giving $T = 144$ time evolving observations for each subject. Each subject's data is normalized to zero mean per time point and whitened.

In order to extract the reference signals using a data-driven approach, we perform gICA using the Group ICA for fMRI (GIFT) toolbox (http://mialab.mrn.org/software/gift) on the resting-state fMRI data. We estimate the model order for each subject using the minimum description length criterion that accounts for sample dependence ([122]) and

the final order is selected as the mean (30) plus one standard deviation (5) across all subject's model orders. The dimension of the signal subspace in the subject-level PCA stage is set as 53 and the order for the group-level PCA stage is set as 35. By default, GIFT selects the subject-level PCA order (53) to be 1.5 times the final order (35). ICA using the entropy rate bound minimization algorithm (ERBM) [52, 53] is used to estimate 35 components/networks. ERBM is a flexible ICA algorithm that exploits multiple statistical properties of the sources such as sample dependence and higher order statistics, and provides a better estimation of fMRI sources ([**?**, 54]). The ICA algorithm is run 10 times and the best run is selected using the minimum spanning tree approach ([123]). Among the 35 group-level components, we visually select $N = 17$ components as exemplars, denoted as $\mathbf{d}_n,\ n = 1, \ldots, 17$, and these components are used as reference signals in the second stage.

The 17 networks are categorized into 8 domains: auditory (AUD), sensorimotor (SM), frontal (FRO), fronto-parietal (FP), parietal (PAR), visual (VIS), default mode network (DMN) and cerebellum (CB). The PAR domain comprise three networks: PAR1, PAR2 and PAR3, corresponding to their peak activation located in the primary somatosensory cortex, supramarginal gyrus and somatosensory association cortex, respectively. The DMN domain consists of one component corresponding to posterior DMN, one component corresponding to anterior DMN (ADMN), one DIC network and one insular (INS) component. The DIC component shows a network of a de-activated posterior DMN component and an activated central executive network and right fronto-insular (INS) network. The VIS domain comprise two networks: VIS1 and VIS2, corresponding to their peak activation situated in the lateral and medial visual cortex, respectively. The FRO domain comprise two networks: FRO1 and FRO2 corresponding to their peak activation in the frontal cortex located anterior to the premotor cortex and dorsolateral prefrontal cortex, respectively.

Each of these $N = 17$ components is used as a reference signal in the acIVA model

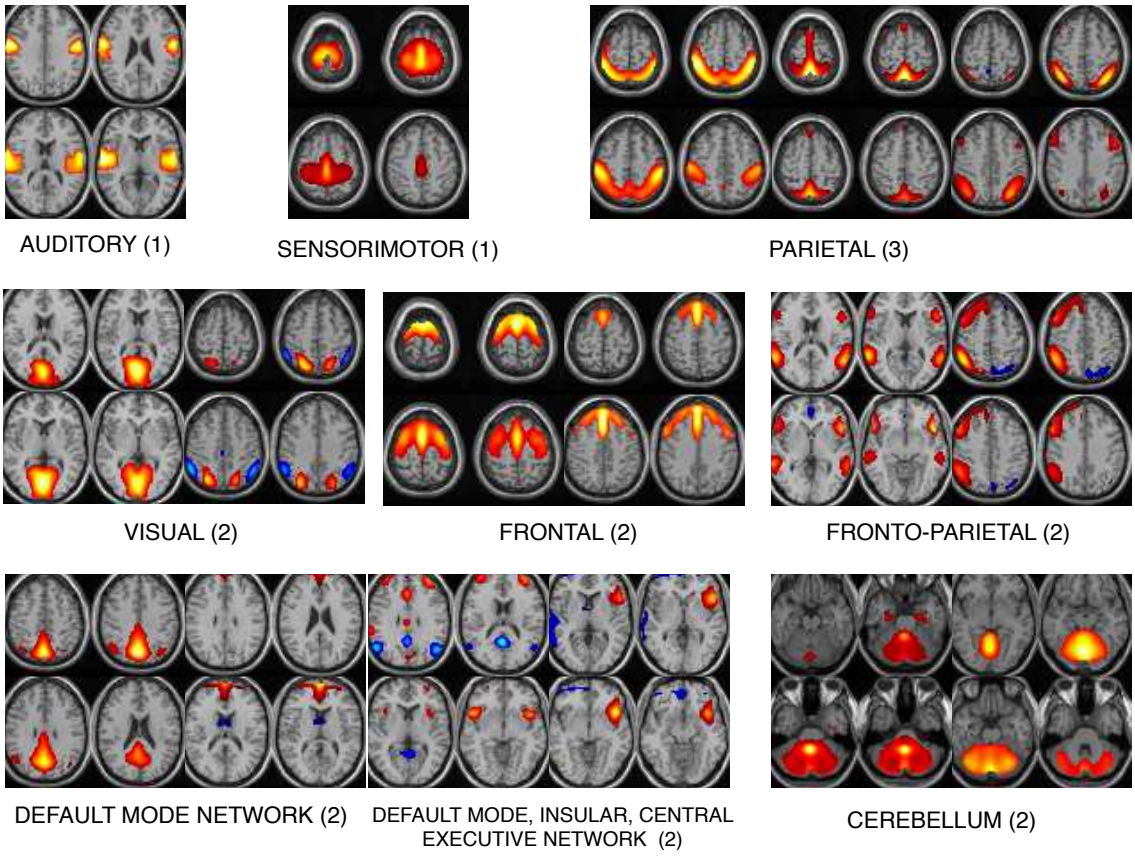


FIG. 6.3. The 17 components selected are divided into 8 domains: auditory (AUD), sensorimotor (SM), frontal (FRO), fronto-parietal (FP), parietal (PAR), visual (VIS), default mode network (DMN) and cerebellum (CB). The DMN domain includes spatial maps consisting the anterior, posterior DMN, central executive network and insular (INS) components. The number indicated next to each domain name is number of components belonging to that domain.

in order to capture their variation in both the spatial and temporal domain. For the acIVA model, we divide each subject's data into $M = 17$ windows of length $L = 16$ with a 50% overlap, resulting in a total of $MK = 3043$ windows. By performing acIVA on each subject's data, we reduce the dimensionality of the SCV from 3043 to 17. The first SCV is constrained to be correlated with one of the 17 group components. The acIVA method using IVA-L-SOS algorithm, with the set $\mathcal{P}$ defined as $0.001, \ldots, 0.9$ and $\gamma_n = 3$, is ap-

plied on the windowed datasets of each subject to estimate 10 solutions. Since IVA is an iterative algorithm, optimization of IVA results in different solutions depending on the initialization. Hence, in order to select the most representative run, we perform the cross jISI run selection method, as described in Section 2.5. Along with addressing the issue of high dimensionality by limiting the size of the solution space, the use of references in IVA also results in components that are ordered across multiple subject-level IVA decomposition, thus yielding SCVs that are aligned across subjects. In order to verify that the estimated constrained SCVs are ordered across subjects, we visually inspected the estimated components and observed that these components were similar to the reference signal. We also inspected the final constraint parameter for all reference signals and for all subjects and the range of these values was between 0.4 to 0.9, indicating that the components are ordered as per the reference signal. The estimated source corresponding to $n$th constraint for the $k$th subject at $m$th window from the consistent run is denoted as $\hat{\mathbf{s}}_n^{[m,k]}$. The corresponding time courses at each window are further processed to correct for quadratic, linear and cubic trends, and low-pass filtered with a cutoff of 0.15 Hz [19].

## 6.5 Identification of spatial dFNC and temporal dFNC patterns

As discussed in Chapter 1, FC measures the association between activation patterns of different regions of brain. We use Pearson's correlation coefficient to measure the connectivity between the time courses and spatial maps at each time window. We obtain $M$ graphs for each subject, $\mathbf{R}^{[k,m]}, k = 1, \ldots, K, \ , m = 1, \ldots, M$, using $N$ nodes and $N(N-1)$ edges, denoted as $r_{n_1 n_2}^{[k,m]}$. The $N$ nodes represent spatial maps or time courses and an edge defines the Pearson's correlation coefficient between the $n_1$th and $n_2$th nodes, $n_1, n_2 = 1, \ldots, N$. Thus, we obtain $M$ temporal dFNC (tdFNC) and spatial dFNC (sdFNC) graphs of dimension $N \times N$ from time courses and spatial nodes respectively for each subject, as shown

in Fig 6.4. These graphs are further analyzed in the next chapter to measure the degree of

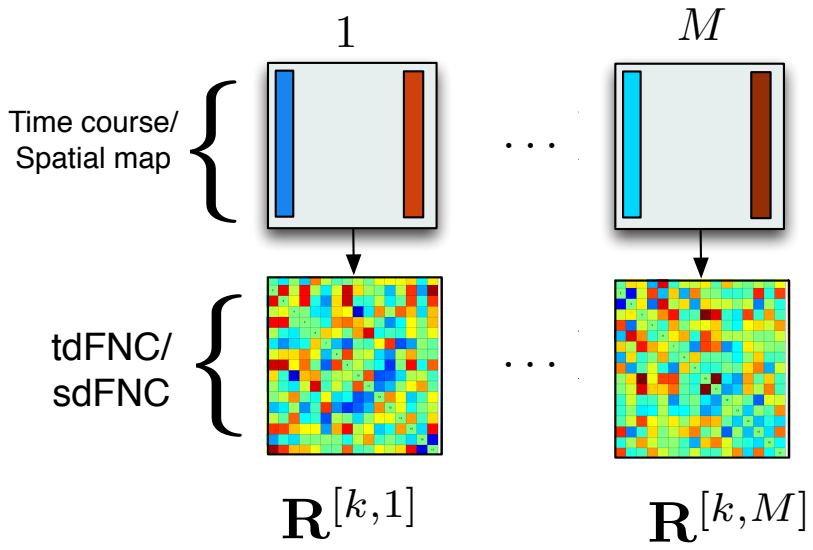


FIG. 6.4. sdFNC and tdFNC graphs are obtained by computing the Pearson's correlation coefficient between each pair of time courses and spatial maps.

fluctuation of connectivity, for prediction of subject class and for identification structures FC patterns, referred to as states.

## 6.6 Summary

In this chapter, we proposed a technique that assumes variability in both spatial and temporal domains to extract time-varying spatio-temporal patterns from large-scale fMRI data. We propose the use of acIVA to mitigate the effect of high dimensionality, where the reference signals are efficiently incorporated in an sliding-window based framework, and to avoid an additional source alignment step. The reference signals are extracted using gICA applied on all subjects and correspond to the stationary representations of the fluctuating components. In the sliding-window based acIVA framework, the time-varying representations of these stationary components is extracted through an adaptive tuning technique. We

apply the proposed technique on COBRE dataset that consists of 179 subjects (91 healthy controls and 88 patients with schizophrenia), and estimate 17 functionally relevant components at each of the 17 time windows. We describe about a technique to compute dFNC graphs from time courses and spatial maps at each time window. In the next chapter, we propose metrics to quantify the variability of FC and spatial network, and demonstrate the benefits of spatial dynamic features using a prediction technique and through the analysis of states.

In the next chapter, we explore the benefits of exploiting variability in the spatial domain, and propose metrics to quantify the variability of dFNC patterns and spatial networks. We also propose a prediction technique to study the features obtained using sdFNC and tdFNC graphs, and perform a state-based analysis on sdFNC graphs.

Chapter 7

# SPATIAL DYNAMIC FUNCTIONAL NETWORK CONNECTIVITY ANALYSIS

In the previous chapter, we discussed the proposed technique to extract time-varying spatio-temporal patterns from fMRI data using a sliding-window based acIVA framework. In this chapter, we explore the use of spatial domain for dFNC analysis in order to demonstrate the benefits of exploiting variability in the spatial domain and taking advantage of the large sample size in this domain, using a data-driven approach.

## 7.1 Introduction

The emergence of dFNC analysis has allowed for the study of temporal behavior of the brain and how it changes over the period of time. Studies have shown that changes in FC are not random, but exhibit structured patterns of connectivity, referred to as states, [19, 34, 35]. State-based analysis using temporal dFNC patterns includes identification of these structured patterns, commonly using a *k*-means clustering framework, followed by computing metrics such as number of transitions from one state to another, mean dwell time in a state and probability of occurrence of a state. These metrics are further analyzed to study differences between two groups of subjects in order to identify distinct biomarkers of disease, condition or modalities [19, 20, 104, 124, 125]. Studying the differences in the degree of variability of FC across different brain regions is also of interest, and has

identified differences in various disorders [16, 38, 104, 126].

In this work, we perform post-analysis of the time-varying spatio-temporal patterns in order to identify distinct patterns that show differences between HC and SZ. We propose two graph-theoretical metrics to quantify the degree of variability of the functional connections and spatial networks, and perform permutation tests to identify differences between HC and SZ. We perform a prediction technique to compare the ability of temporal dFNC (tdFNC) patterns and sdFNC patterns to predict if a subject is a patient or a control. We also perform a joint analysis by combining the sdFNC and tdFNC patterns together in order to explore the contribution of each towards prediction and observe that the use of sdFNC patterns alone provides higher prediction accuracy than using tdFNC patterns, or a combined feature set. This shows that exploiting the variability and taking advantage of large sample size in the spatial domain provides meaningful discriminative features. We also obtain structured patterns of connectivity/states from sdFNC patterns and identify differences between patients and controls in terms of dwell time, transition matrix and fraction of time spent in each state. To the best of our knowledge, no study has been performed to identify these properties from sdFNC patterns. Our results indicate that patients tend to stay in or transition between states associated with hyperconnected brain network. We also find significant associations between the resulting functional connectivity and signs of paranoia in the patient group using sdFNC patterns.

## 7.2 Quantification of dynamics

A number of studies have focused on identifying biomarkers that show differences in the HC and SZ groups [127–129]. We were interested in determining if any of the estimated spatio-temporal component features would be sensitive to mental illness. One feature that is of interest is variability of functional connectivity and spatial maps [104, 130]. In this

work, we define two metrics: component similarity and functional connectivity fluctuation, to identify the spatial components and functional connections that are variable.

### 7.2.1 Functional connectivity fluctuation

The functional connectivity fluctuation, $\sigma^{[k]}_{n_1 n_2}$, for each subject using tdFNC and sdFNC graphs is computed as follows,

$$\sigma^{[k]}_{n_1 n_2} = \sqrt{\frac{1}{M-1}\sum_{m=1}^{M}\left(r^{[m,k]}_{n_1 n_2} - \bar{c}^{[k]}_{n_1 n_2}\right)^2}, \tag{7.1}$$

where $\bar{c}^{[k]}_{n_1 n_2} = \frac{1}{M}\sum_{m=1}^{M}\left|r^{[m,k]}_{n_1 n_2}\right|$ is the mean of the connectivity metric, $r^{[m,k]}_{n_1 n_2}$, computed across M windows for nodes $n_1$ and $n_2$, and $r^{[m,k]}_{n_1 n_2}$ denotes the Pearson's correlation coefficient between the nodes $n_1$ and $n_2$. Each node represents a spatial map/time course obtained using acIVA. We also compute this metric on the tdFNC graphs obtained from gICA, which estimates time courses while assuming the spatial networks are stationary. The estimated reference signals are back-reconstructed to estimate subject specific time courses, and a sliding window of length $L = 16$ is applied with a 50% overlap yielding $M = 17$ windows. For each subject, tdFNC graphs are obtained as mentioned above.

The permutation test results on the functional connectivity fluctuation metric identifies a number of distinct and relevant connections. Fig. 7.1 shows the connections identified as significantly different using tdFNC: acIVA (Fig. 7.1(a)) and sdFNC: acIVA (Fig. 7.1(b)). The combined result using tdFNC and sdFNC graphs computed from our method suggests lower variability within the cognitive control network and within the default mode network for the SZ group. Studies have reported descreased hemodynamic response in the insula region in the SZ group causing low variability in this region [131]. Higher variability is observed across components in different clusters, namely, the visual and cognitive control cluster, visual and DMN cluster, visual and frontal component, and fronto-parietal and sen-

sorimotor component for the SZ group. This variability across brain regions may be due to dysfunction in the working memory, attention and visual learning [132] and the tendency of patients with schizophrenia to engage more brain regions than healthy controls [133]. Fig. 7.2 shows the connections identified as significantly different using gICA. The analysis on the tdFNC matrices from gICA identifies higher temporal variability in HC group between DMN and the frontal component of the cognitive network and higher variability in the SZ group between visual and auditory component, and between auditory and sensorimotor component. These results suggest that the use of tdFNC graphs alone does not fully characterize the dynamic functional connectivity and assuming variability in both spatial and temporal domains results in identification of more distinct biomarkers.

### 7.2.2 Component similarity

In order to quantify the variability of the $n$th feature for each subject $k$, we compute the absolute value of the Pearson's correlation coefficient between the $n$th component at window $m$, $\hat{\mathbf{s}}_n^{[m,k]}$, and the $n$th component at window $m+1$, $\mathbf{y}_n^{[m+1,k]}$. Component similarity is then obtained by computing the mean across all adjacent windows. A higher value of this metric suggests that the spatial network is less variable. Figure. 7.3 shows the results for the components that demonstrated significant differences ($p < 0.05$, corrected) using a permutation test between healthy controls and schizophrenia patients. The medial visual (VIS2), SM, FP and primary somatosensory cortex (PAR1) components exhibited less variability within the HC group whereas the supramarginal gyrus (PAR2) component exhibited less variability in schizophrenia. These components were also identified as less variable among healthy individuals in a previous dynamic study [104]. Deficits in visual perception, attention and motor regions have been previously shown in schizophrenia, which may lead to variability in these components. Figure. 7.4 shows an example of the changes in the visual component of one subject for whom the stationarity is estimated as the highest within the HC and SZ

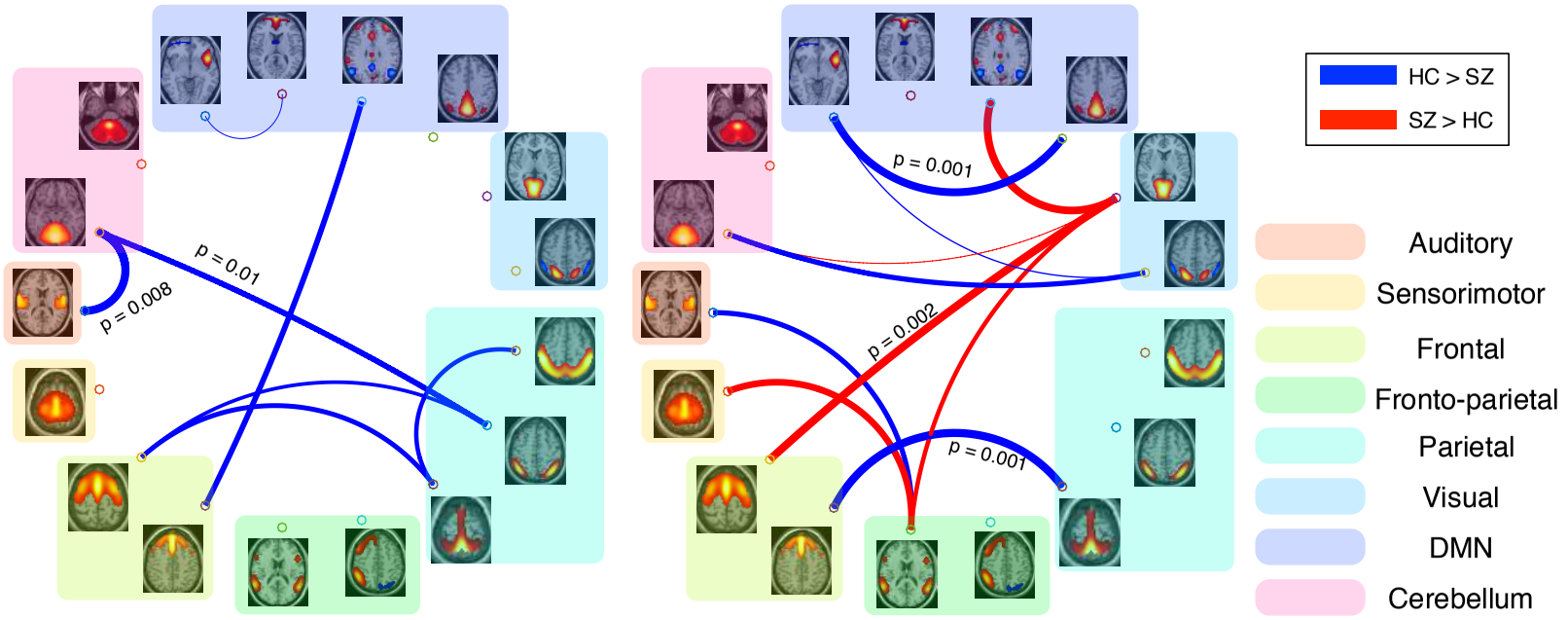


(a) acIVA: tdFNC (b) acIVA: sdFNC

FIG. 7.1. Associations that demonstrate significant difference ($p < 0.05$, corrected) between HC and SZ group. Blue connections indicate higher measures in controls whereas red indicates higher measure in patients. Thickness of the connection indicates a more significant difference (lower $p$-value) between HCs and SZs.

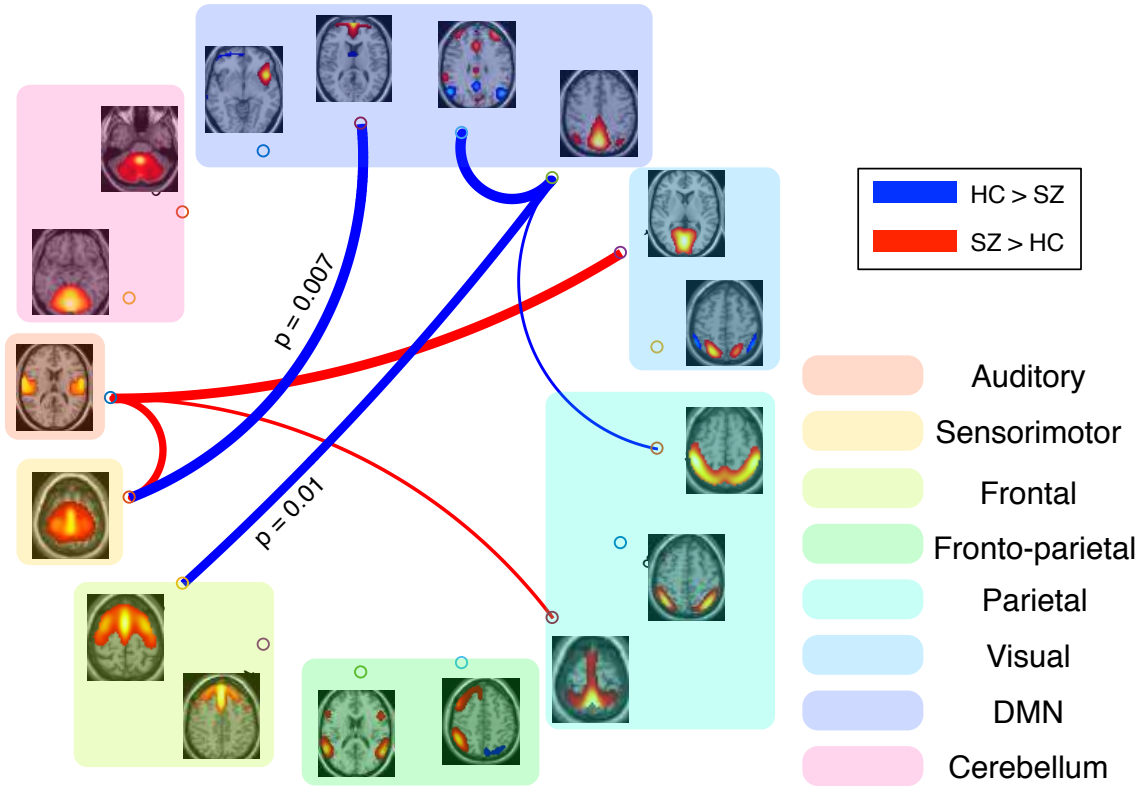


FIG. 7.2. Associations that demonstrate significant difference ($p < 0.05$, corrected) between HC and SZ group, using gICA. Blue connections indicate higher measures in controls whereas red indicates higher measure in patients. Thickness of the connection indicates a more significant difference (lower $p$-value) between HCs and SZs. More group differentiating and relevant connections with significantly lower $p$-values are obtained using the proposed method as compared with gICA.

groups. The activated voxels corresponding to the visual component also shows disrupted activation patterns across time for the SZ subject. This is consistent with previous work showing disruptions in the perceptual functions in SZ subjects including abnormalities of smooth pursuit in this group of subjects [134].

## 7.3 Prediction technique

A primary goal in a dFNC state-based analysis is the identification of states that are distinctively associated to healthy controls and patients with schizophrenia. A natural way

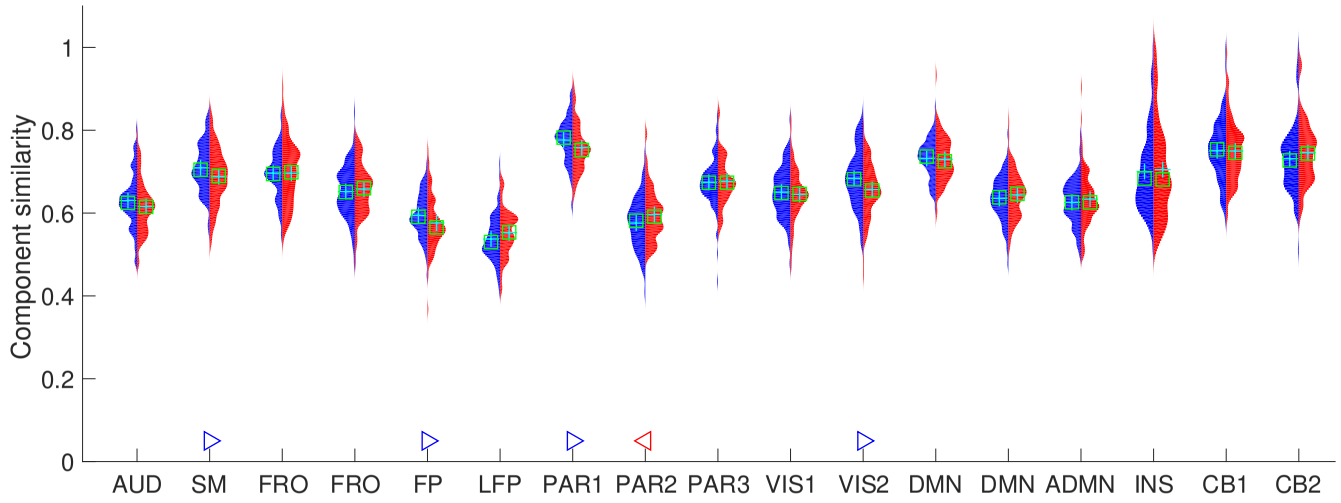


(a)

FIG. 7.3. Component similarity of all components. Red indicates the distribution of this metric for the SZ group and blue indicates the distribution of this metric across HC group. Components that demonstrate significant difference ($p < 0.05$, corrected) between HC and SZ group are indicated by a triangle. A blue '▷' denotes the corresponding component is less variable in the HC group whereas a red '◁' denotes the corresponding component is less variable in the SZ group. The results indicate that SM, FP, PAR1, and VIS components are less variable in HC whereas PAR2 is less variable in SZ group.

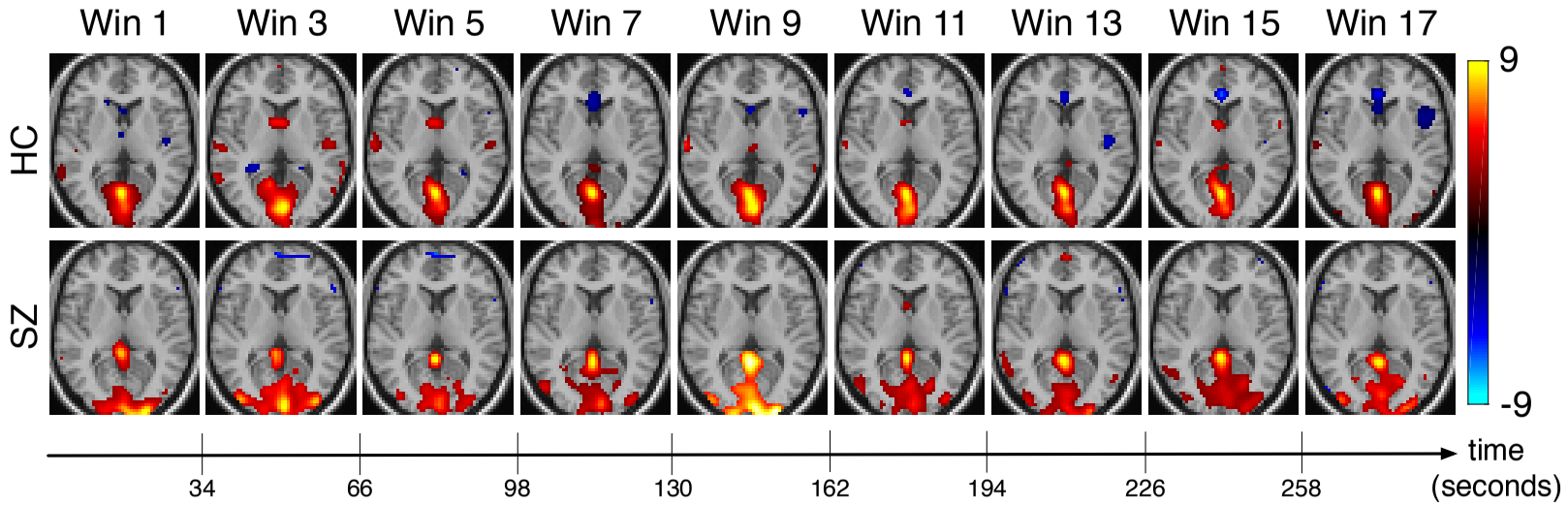


(a)

FIG. 7.4. Changes in the visual component (VIS1) for one subject corresponding to lowest variability within the HC group and SZ group. The visual component shows disrupted activation pattern for the SZ subject as compared with the HC subject.

to identify such states, is to measure the probability of occurrence of a state for each group separately. In this work, we propose a technique to predict if a subject is a HC or SZ, based on the occurrence of a state within each group over the entire scanning period. In order to study how informative the spatial and temporal dFNC features are, we obtain the probability of occurrence of states using the sdFNC and tdFNC graphs computed as described in Section 6.5. Note that the aim of this experiment is to observe potential advantages of sdFNC features and not the actual prediction accuracy, hence we use a simpler Naive Bayes classifier that does not require tuning of parameters. The flowchart for the prediction technique is shown in Figure 7.5. We obtain 1000 independent Monte-Carlo subsamplings of the data. In each subsampling, subjects from HC and SZ group are divided into training and testing sets, where each training group consists of 75 randomly sampled subjects from the HC and the SZ group ($K_{\text{train}} = 150$). The remaining subjects form the testing set ($K_{\text{test}} = 29$). We then obtain $K_{\text{train}} \times M$ observations of $N(N-1)/2$ dimensional features from the tdFNC/sdFNC matrices. In order to select the distinguishing features from the $N(N-1)/2$ features, we perform a two-sample $t$-test on the features from the HC and SZ group as shown in Figure 7.5(B). Features that demonstrate significant difference ($p < 0.05$) are used in further stages. The indices of the significant features are recorded and used in the testing stage. This feature selection is done separately for tdFNC and sdFNC matrices. The selected features are clustered into $C$ clusters, where in this experiment we vary the number of clusters from 3 to 30. For training the Naïve Bayes classifier, we obtain the probability of each state for the HC group and SZ group, $p^g(C_i),\ g = \{\text{HC, SZ}\}$. In the testing stage, the features that indicated significant difference in the training stage were selected and each observation from a test subject is assigned a state with maximum Pearson's correlation between the observation and the cluster centroid. We then obtain the probability of each state using $p^{[k]}(C_i) = n_i^{[k]}/M,\ i = 1, ..., C$ and use the test feature vector

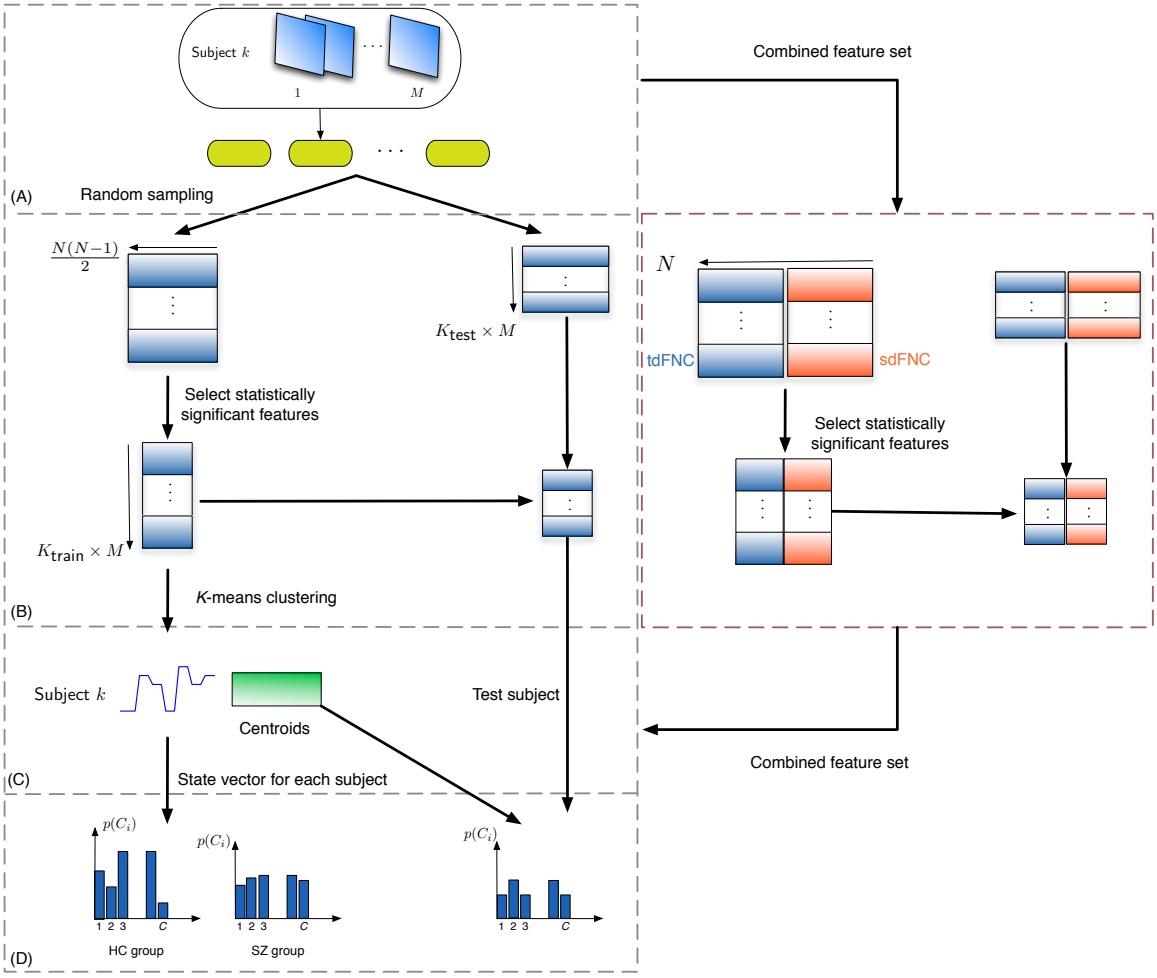


FIG. 7.5. Flowchart to obtain the features for prediction. (A) The subjects are divided into training and testing set, where the training set consists of 150 subjects, 75 from the HC and SZ group each. The remaining 29 subjects form the testing set. (B) Each tdFNC/sdFNC matrix is flattened to a row and the distinguishing features are extracted using a two-sample $t$-test. The indices of the distinguishing features are recorded and used to select the corresponding features in the testing stage. In the combined feature set for joint analysis, the flattened features from both domains are concatenated in the feature dimension and similar steps are performed. (C) The selected features from the training set are clustered into $C$ clusters using $K$-means clustering to obtain the centroids and the state vector for each subject. (D) The probability of occurrence of each state is computed for the HC and SZ group separately. For the testing stage the state vector for each subject is obtained using the centroids from the training stage and probability of occurrence for each state is computed.

to predict the class of the subject. A test subject is assigned to HC or SZ group using the following rule,

$$\hat{y} = \arg \max_{g=\{\text{HC,SZ}\}} p(g) \prod_{i=1}^{C} [p^g(C_i)]^{n_i} \tag{7.2}$$

where $n_i$ denotes the number of occurrences of state $i$ in the test subject. Steps (B-D) from Figure 7.5 are performed for each sub-sampling of the data.

For the joint analysis of spatio-temporal features, the sdFNC and tdFNC features selected after the two-sample $t$-test on these feature sets separately, are concatenated in the feature dimension to study the effect of combining the two feature sets on prediction accuracy. We compare the results from the combined feature set with the results from using sdFNC and tdFNC feature set alone. Table 7.1 provides some inferences regarding the comparison results. Let $Q_{\text{S}}$ denote the prediction accuracy obtained using sdFNC matrices, $Q_{\text{T}}$ denote the prediction accuracy obtained using tdFNC matrices and $Q_{\text{ST}}$ denote the prediction accuracy obtained using the combined feature set. We can say that if the prediction accuracy increases after combining the sdFNC and tdFNC features, both feature sets provide unique discriminative features, whereas if the prediction accuracy using sdFNC features is greater than $Q_{\text{ST}}$, then tdFNC provide non-discriminative features, hindering the classification performance.

### 7.3.1 Comparison of sdFNC and tdFNC features with joint feature set

The average prediction accuracies computed across 1000 Monte Carlo subsamplings, using the sdFNC, tdFNC and combined feature set for different number of clusters is shown in Figure 7.6. Figure 7.6(A) shows the result for the HC group and Figure 7.6(B) shows the result for the SZ group. In order to test if the prediction accuracies computed using sdFNC and tdFNC features are significantly different from the combined feature set, we perform a permutation test using a two-sample $t$-test as the hypothesis test. The results indicate that

| | |
|---|---|
| $Q_{ST} > Q_S, Q_T$ | sdFNC and tdFNC yield unique discriminative features jointly contributing to classify subjects |
| $Q_{ST} < Q_S, Q_T$ | sdFNC and tdFNC both yield non-discriminative features that are unable to classify subjects |
| $Q_S$ or $Q_T > Q_{ST} > Q_T$ or $Q_S$ | tdFNC or sdFNC yield non-discriminative features affecting the prediction |
| $Q_{ST} = Q_S$ or $Q_T$ | tdFNC or sdFNC are not providing additional information to classify subjects |

Table 7.1. Inferences about predictability of sdFNC, tdFNC and combined feature set. $Q_S$ denotes the prediction accuracy obtained using sdFNC matrices, $Q_T$ denotes the prediction accuracy obtained using tdFNC matrices and $Q_{ST}$ denotes the prediction accuracy obtained using the combined feature set.

the prediction accuracy computed using sdFNC features is significantly higher than the one computed using tdFNC and the combined feature set for the SZ group for different number of clusters. This suggests the use of tdFNC features yield non-discriminative features that degrade the prediction performance for the SZ group. For the HC group, the prediction accuracy computed using sdFNC features is higher than the one computed using tdFNC features and equal to the combined feature set for the SZ group for different number of clusters. This suggests that the tdFNC features are not providing additional information to classify subjects as controls.

### 7.3.2 Comparison of sdFNC and tdFNC features

In order to test for differences between the prediction accuracies using sdFNC and tdFNC features, and between the HC group and the SZ group, we perform a permutation test between these groups using a two-sample *t*-test as a hypothesis test. The distribution plots of the accuracies and the permutation test results are shown in Figure 7.7. The permutation test result indicates that the sdFNC features yield a significantly higher prediction

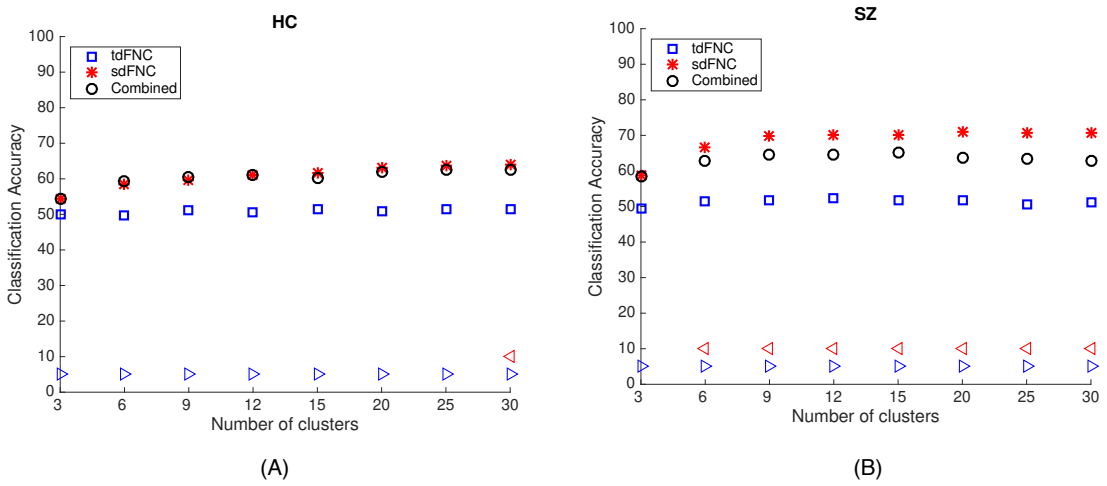


FIG. 7.6. Average prediction accuracy computed over 1000 independent Monte-Carlo samplings using tdFNC, sdFNC and combined features for (A) HC group and (B) SZ group. A blue triangle denotes significant difference between tdFNC result and combined feature set result, whereas a read triangle denotes significant difference between sdFNC result and combined feature set result. A triangle pointing left, '◃', indicates the prediction accuracy of tdFNC/sdFNC is greater than the combined feature set result, whereas a triangle pointing right, '▹', indicates the prediction accuracy of tdFNC/sdFNC is less than the combined feature set result.

accuracy when compared with tdFNC features, providing evidence that exploiting variability in the spatial domain yields meaningful distinguishing information. The average prediction accuracy using tdFNC features is around 50%, which is equivalent to providing random guesses regarding the class of a subject. This provides additional evidence that tdFNC features are not providing any additional information as compared to a random classifier. The permutation test result between the HC and the SZ group indicates a significantly higher prediction accuracy for the SZ group using sdFNC features. Since the feature used in this technique is the probability of occurrence of each state, we can infer that patients with schizophrenia tend to stay or transition to a certain group of states more often than healthy controls. A natural question is the identification of these predictable states and their differences with respect to states associated to a healthy group of subjects. In

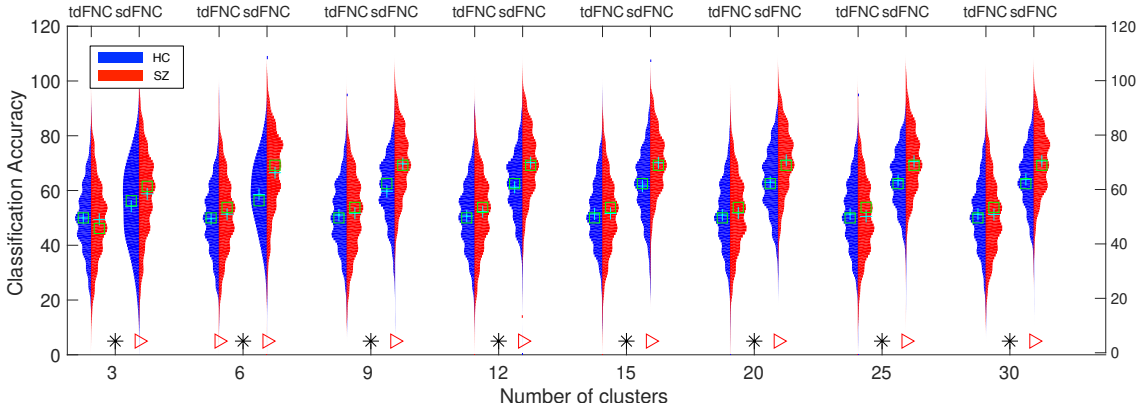


FIG. 7.7. Predictability results using Naïve Bayes classifier. Red color indicates the histogram of prediction accuracies obtained for the SZ group whereas blue indicates the histogram of prediction accuracies for the HC group. X-axis denotes the number of clusters, C used to cluster the features from tdFNC/sdFNC graphs. The green '+' sign denotes the mean value and '□' sign indicates the median value. The markers at the bottom show results from a permutation test to test for statistical differences ($p < 0.05$, corrected). A '$*$' denotes the accuracies are significantly higher using sdFNC features compared with tdFNC features. A '$\triangleleft$' denotes prediction accuracy for HC group is higher whereas '$\triangleright$' denotes higher prediction accuracy for SZ group. We observe a higher prediction accuracy using sdFNC features and a significantly higher accuracy for the patients group, for different number of clusters.

Section 7.4, we discuss the results obtained from the state-based analysis using the sdFNC matrices and identify the states that are associated with the patients and controls group.

We also compute the sensitivity and specificity of the prediction model obtained using sdFNC and tdFNC features. The true positives (TP) denote the percentage of SZ subjects that are correctly identified as SZ, true negatives (TN) denote the percentage of HC subjects that are correctly identified as HC, false negatives (FN) denote the percentage of SZ subjects incorrectly identified as HC, and false positives (FP) denote the percentage of HC subjects incorrectly identified as SZ. Sensitivity and specificity for each Monte Carlo subsampling is computed as follows,

$$\text{Sensitivity} = \frac{\text{TP}}{\text{TP} + \text{FN}}, \quad \text{Specificity} = \frac{\text{TN}}{\text{TN} + \text{FP}}.$$

Figure 7.8 shows the results of these measures computed for sdFNC and tdFNC features. Sensitivity and specificity values are higher using sdFNC features compared with the tdFNC features. A higher sensitivity for sdFNC features indicates that these features are better able to identify SZ subjects than HC subjects.

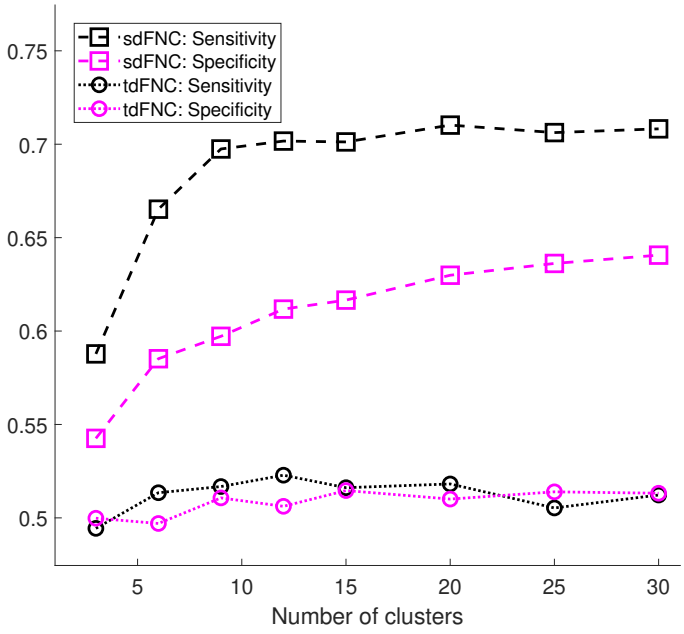


FIG. 7.8. Sensitivity and specificity of the prediction model trained using sdFNC and tdFNC features. The sensitivity and specificity values are averaged over 1000 Monte Carlo subsamplings. The results indicate that sensitivity and specificity is higher using sdFNC features compared with the tdFNC features. A higher sensitivity for sdFNC indicates a better prediction ability of these features to correctly identify SZ subjects.

## 7.4 Identification and analysis of states

Recent studies have shown that fluctuations in the brain networks in resting-state are not random but exhibit structured patterns that vary over time ([19, 34, 35]). In this study, we obtain these structured patterns or states using sdFNC matrices. In the first step towards identifying the states, we flatten the upper diagonal part of each correlation matrix, $\mathbf{R}^{[m,k]}$,

to obtain a feature vector of dimension $N(N-1)/2$ yielding $MK$ observations. For each subject, the standard deviation across the feature dimension is computed and a subset of FNC matrices are selected corresponding to the maximum standard deviation as subject exemplars. Thus the subject exemplars represent the features that are more informative, alternatively those with higher variability. Further $k$-means clustering is performed to cluster these subject exemplars into $C$ clusters using Pearson's correlation coefficient as the distance measure. The centroids resulting from clustering the subject exemplars are used as initial points to cluster the entire observation set. This two-step clustering process is performed in order to obtain a robust solution. The performance of $k$-means clustering assigns a cluster or state index to each observation resulting in a state vector for each subject. The state vector thus represents the evolution of the states over time. This vector is further analyzed to obtain the transition matrix, dwell time and fraction of time spent for each state and for each subject. The transition matrix denotes the number of transitions from state $i$ to state $j$, $i, j = \{1, \ldots, C\}$, the dwell time denotes the amount of time a subject remains in a particular state, and fraction of time spent denotes the probability of occurrence of a state.

We identify six distinct states using spatial dFNC matrices. The number of clusters is estimated as six using the silhouette criterion. We also compute the optimal number of clusters using other criteria available in the group ICA for fMRI toolbox. The estimated values are in the range 2-10, with the median value being six. Hence, we choose the final values as six for the optimal number of clusters. The group-specific states and features that demonstrate significant differences between HC and SZ group using sdFNC matrices are shown in Figure 7.9(A). The significantly different features within each state were identified by performing a permutation test between the HC group and the SZ group. The group-specific states show differences in the level of connectivity between pairs of components, which are reflected in the third row of Figure 7.9(A) that shows differences between the HC and SZ

group. The parietal component has high positive connectivity with the auditory, sensorimotor and frontal components in all states and indicates simultaneous activation of these regions. The parietal lobe plays a vital role in processing sensory information such as touch, sound and vision, which is obtained from different parts of the body. A subject in the scanner is exposed to scanner noise and hence the brain is involved in processing the auditory information, causing activation of parietal and auditory components. The parietal component also plays a role in receiving signals from sensory organs, which is then passed to motor-related regions, such as sensorimotor and frontal components, in order to control the body posture. Since a subject is asked to lay still in the scanner, the subject is focusing on balancing his/her body, causing the activation of these regions. An observed positive correlation between the sensorimotor and frontal component provides additional support towards the hypothesis. Cerebellum on the other hand, receives the sensory information from different parts of the body. Hence, a high negative correlation between the parietal and cerebellum component indicates simultaneous deactivation of one component while the other is active, suggesting a process of first receiving and then processing the sensory information. This might also help explain the observed negative correlation between cerebellum and motor-related components. These connections are observed in all states, indicating that these regions form a central hub at resting-state and play a vital role resting-state fMRI data.

We obtain the transition matrix, dwell times and fraction of time spent in each state for each subject. For each transition pair $\{i, j\}$, $i, j = 1, \ldots, 6$, we perform a permutation test to identify differences between the HC and the SZ group. Each significantly different pair denotes that one group transitioned from state $i$ to $j$ more frequently than the other group. Similarly, we perform a permutation test on the mean dwell time of each state and fraction of time spent in each state to test for differences between HC and SZ group. The results

for transition matrices (TM), mean dwell time (MDT) and fraction of time spent (FR) are shown in Figure. 7.9(B), Figure. 7.9(C) and Figure. 7.9(D) respectively. The transition matrix indicates that healthy controls tend to stay in State 1 more frequently, whereas patients with schizophrenia tend to transition more frequently from State 3 to State 4 and State 1 to State 5. State 3 and 4 differ in the level of positive correlation between cerebellum and auditory component, insular and parietal component, visual and parietal component and anterior DMN and visual component, whereas State 1 and 5 differ in the level of positive correlation within the visual network, and between the cerebellum and visual component. These states also differ in the level of negative correlation between the cerebellum and left fronto-parietal component. These connections are also observed in State 2 where patients demonstrate a significantly higher mean dwell time and fraction of time spent compared to controls. Hence patients with schizophrenia tend to reside in or switch to a state that has high positive correlation within the visual network and between the anterior DMN and frontal component, visual and parietal component, anterior DMN and frontal component, and cerebellum and visual component. The patients group also tend to reside in or switch to a state that has high negative correlation between the cerebellum and left fronto-parietal component. This suggests that patients with schizophrenia are associated to a hyperconnected brain network and studies have shown their tendency to engage more brain regions than healthy controls ([133, 135, 136]).

Since patients with schizophrenia demonstrate a significantly high mean dwell time and fraction of time spent in State 2, and controls show a high (although not significant) mean dwell time in State 1, we discuss these two states in detail. State 2 differs from State 1 in terms of high positive correlation within the visual network, between frontal and anterior DMN component, cerebellum and parietal component, cerebellum and visual component, and DMN and insular component. A high negative correlation is also observed between

the frontal and visual component, parietal and anterior DMN, DMN and anterior DMN. As discussed above, a high negative correlation between parietal and cerebellum component is due to the cognitive process of receiving and processing sensory information one at a time, a positive correlation between these components in State 2 suggests abnormal connectivity. A healthy brain has shown evidence of positive correlation between anterior and posterior DMN, and a deactivation in DMN due to an activated INS region ([90, 137]). However a high negative correlation between the anterior DMN and posterior DMN, and a high positive correlation between posterior DMN and insular region in State 2 of the SZ group also provides evidence of dysfunction in the DMN domain of schizophrenia, which is a common trait in this group ([137]). A high positive correlation between anterior DMN and frontal component might suggest the activation of both region due to their role in social behavior and impulse control. Patients with schizophrenia are known to have paranoia traits, causing them to be constantly aware of the surroundings and prone to impulse control disorder. This causes hyperactivity in the DMN and frontal components of schizophrenic patients ([138–140]). The bottom row of Figure 7.9 indicates the connections that demonstrated significant difference ($p < 0.05$, corrected) between the HC and SZ group. High absolute connectivity is SZ group is indicated by red while high absolute connectivity in the HC group is indicated by blue. State 2 shows most connections that have significantly high absolute correlation in the SZ group. Patients exhibit high correlation between the cerebellum and parietal component, posterior and anterior DMN component, posterior DMN and left fronto-parietal, auditory and DIC component, and cerebellum and DIC network. A significantly high correlation between these components in the SZ group suggest a hyperconnected DMN, which is a common trait of patients with schizophrenia ([141, 142]). A significantly higher connectivity between the anterior DMN and frontal component, and parietal and cerebellum component provides additional support to the hypothesis of para-

noia and abnormal behavior in schizophrenia patients.

## 7.5 Summary

In this chapter, we perform a post-analysis on the sdFNC and tdFNC patterns to study the benefits of assuming variability in the spatial domain, and analyze the potential use of sdFNC patterns and dynamic spatial networks. We propose two metrics to quantify the variability of dFNC and variability of spatial networks. Our analysis on quantifying variability of spatial networks reveals higher variability in the sensorimotor, fronto-parietal, medial visual and primary somatosensory cortex and low variability in the supramarginal gyrus for the SZ group. We also plot the spatial changes in the medial visual cortex of a healthy subject and patient with schizophrenia and observe deficits in the activation of the neurons in this region. A comparison of sdFNC and tdFNC patterns results in a higher sensitivity using sdFNC patterns, indicating their ability to correctly classify individuals in the SZ group. The analysis of time-varying spatial FNC reveals higher inter-cluster variability in the SZ group, and higher transitions to states with hyperconnected brain networks. This is due to the tendency of patients to engage more brain regions than HC.

In the next chapter, we summarize this thesis by discussing the main contribution and results. We also provide possible directions for future research.

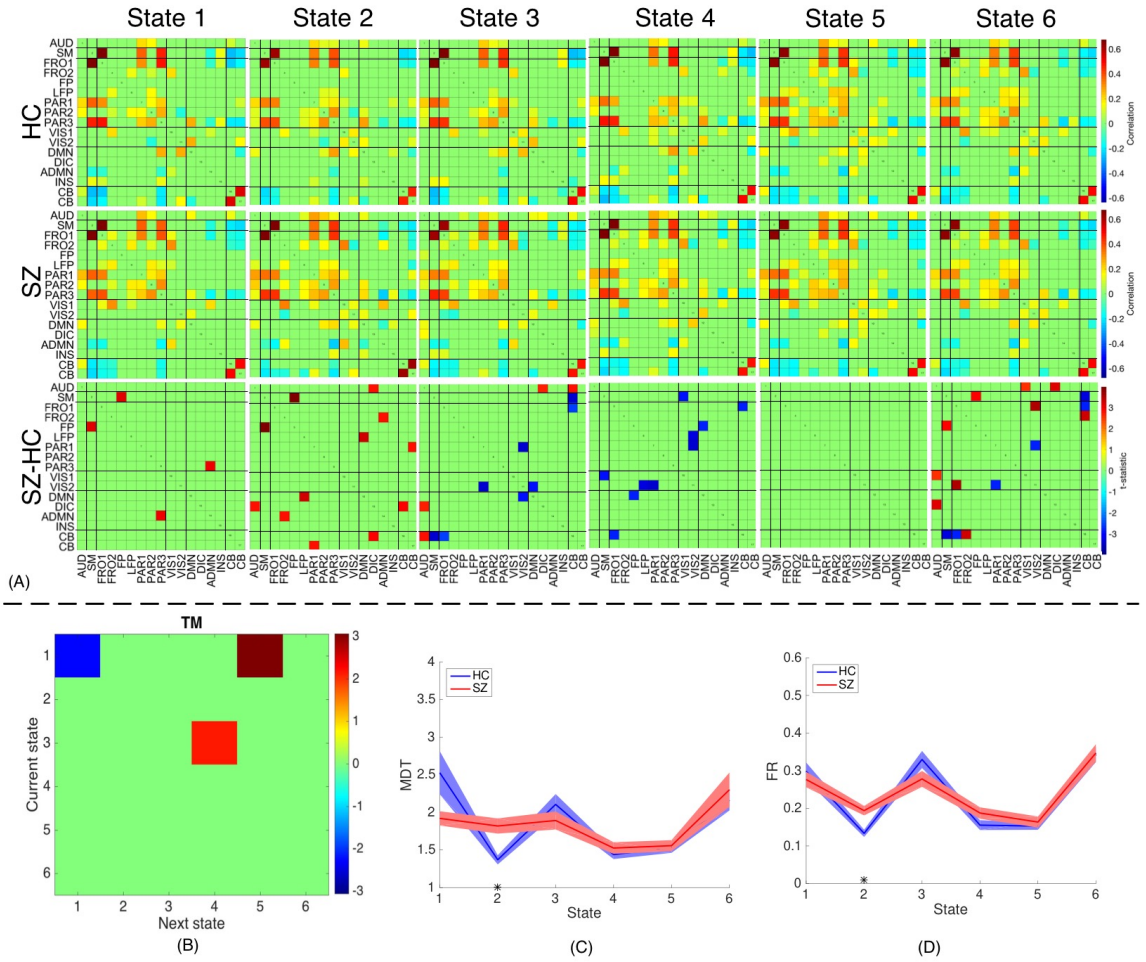


FIG. 7.9. (A) The top two rows shows the group-specific states obtained using sdFNC matrices. The bottom row corresponds to the features that demonstrated significant difference ($p < 0.05$, corrected) between HC and SZ group. Red indicates higher value for SZ whereas blue indicates higher value for HC. (B) Transition matrix (TM) with each element in the matrix showing transitions that are significantly ($p < 0.05$, corrected) different. Blue indicates HCs transitioned more frequently from current state to next state whereas red indicates SZs transitioned more frequently from current state to next state. (C) Mean dwell time of each state for the HC and SZ group. (D) Fraction of time spent (FR) in each state by the HC group and SZ group. Results indicate that SZ subjects tend to transition more frequently from State 3 to State 4 whereas those obtained using dsFNC graphs indicate that SZ subjects transition more frequently from State 1 to State 5. We also observe that SZ subjects tend to stay more in State 2.

Chapter 8

# CONCLUSION AND FUTURE WORK

The goal of this dissertation has been the development of a method that extracts meaningful, timev-varying, functionally relevant networks from large-scale fMRI data, while preserving the variability across individuals. Due to the high dimensionality effect of IVA, we have sought to the address issue of analyzing large-scale fMRI data by taking advantage of the known prior and expected outcome of a particular task. We have looked for an efficient way to incorporate that knowledge into our model, to drive our outcome towards the desired result in such a way that the decomposition is not affected by undesired variables. Due to the flexible nature of the proposed algorithm, it has applications far beyond the context of this dissertation and the datasets to which they were applied. In this chapter, we summarize our results and present possible directions for further research.

## 8.1 Conclusion

Extracting global signatures that provide a general view of the data and capturing the individual-specific aspects of the signatures that provide a detailed view of a group of individuals, modalities or condition, enables a better understanding of the function of the brain. IVA provides a flexible framework to estimate the underlying sources by making use of dataset-specific information that is dependent across datasets. It jointly decomposes multiple datasets into dataset-specific mixing matrix and source matrix such that the sources

within each dataset are maximally independent and sources across datasets are maximally dependent. However, the flexibility of IVA comes at a cost, that is for a fixed number of samples, its performance is affected by a number of aspects.

In Chapter 3 of this dissertation, we study the performance of IVA in terms of increasing number of datasets, number of sources and varying levels of correlation of sources across datasets. The use of more datasets that share a common attribute allows for the utilization of more information content for IVA to exploit the dependence structure across datasets. In fMRI analysis, individuals share the functional networks and the use of datasets from more individuals results in a more robust estimate of the functional networks. The performance of IVA is expected to improve with increase in number of individuals given that the number of samples, voxels in fMRI, are large enough. However, since the number of samples are fixed in fMRI, the improvement in performance is observed until a certain number of datasets, beyond which the performance begins to degrade. The limit of change in performance also depends on other aspects, namely, number of sources and level of correlation. For large number of sources this limit is observed at lower number of datasets. The use of a high model order, number of sources, is desirable for the analysis of fMRI data, due to the estimation of more relevant functional networks. Additionally, the effect of high dimensionality is more prominent in datasets that demonstrate low to moderate correlation among sources across datasets, which is similar to the case observed in fMRI datasets. These two factors, namely, the use of high model order and low correlated sources, increase the complexity even further for the analysis of large-scale fMRI data.

The knowledge of the desired outcome is available is most applications and in fMRI analysis, the use of the reference signals corresponding to functional networks provides a guidance in high dimensional scenarios. In Chapter 4, we propose a technique to adaptively incorporate reference information into the IVA framework in order to guide the search for a

meaningful solution. Although it may seem biased to use functional networks as references to extract functional networks, the idea of this approach is to use a global representation or a stationary representation of the functional networks to guide the estimation of individual-specific or window-specific functional networks. Additionally, selecting accurate global features is still essential and a difficult task since the impact of these functional networks on each individual's dataset is not known prior. The acIVA technique makes use of an adaptive tuning mechanism to control the effect of accurate and inaccurate reference signals, thus providing an efficient and meaningful decomposition.

Extraction of relevant functional networks in a data-driven yet robust manner from a large population group is a topic of interest in many research studies. The use of a high model order, number of functional networks, is well justified through a number of studies, due to the extraction of distinct and meaningful networks. This poses a great challenge for implementing IVA on fMRI data, since its performance degrades with high number of individuals and sources. Additionally the correlated networks across individuals are super-Gaussian distributed with a low degree of correlation, affecting the estimation performance in large-scale scenarios. In Chapter 5 we discuss the use of acIVA to extract meaningful individual-specific networks from large-scale fMRI data acquired from 164 females and 163 males. We propose the use of group-level ICs extracted from the entire population using gICA as reference signals in acIVA, which adaptively tunes the effect of each functional network on each individual's dataset. Our result indicates that the proposed method not only extracts networks that are similar to the reference but also other brain regions that are functionally correlated with the reference signal.

In Chapter 6 of this dissertation, we propose a method to extract time-varying spatio-temporal patterns from large-scale fMRI data, which assumes variability in both spatial and temporal domain. We propose a sliding-window based acIVA framework that uses the sta-

tionary representations of the functional networks as reference signals, in order to capture their window-specific representation. We apply the proposed method on fMRI data acquired from 91 healthy controls (HC) and 88 patients with schizophrenia (SZ). We perform post-analysis on the sdFNC and tdFNC patterns to study the benefits of assuming variability in the spatial domain, and analyze the potential use of sdFNC patterns and dynamic spatial networks. Our analysis on quantifying variability of spatial networks reveals higher variability in the sensorimotor, fronto-parietal, medial visual and primary somatosensory cortex and low variability in the supramarginal gyrus for the SZ group. Deficits in the medial visual cortex are also observed for a SZ patient. A comparison of sdFNC and tdFNC patterns results in a higher sensitivity using sdFNC patterns, indicating their ability to correctly classify patients. The analysis of time-varying spatial FNC reveals higher inter-cluster variability in the SZ group, and higher transitions to states with hyperconnected brain networks. This is due to the tendency of patients to engage more regions than HC for a certain brain function.

## 8.2 Future work

### 8.2.1 MEG + fMRI analysis

Unlike fMRI, which measures the neuronal activation in the brain using an indirect BOLD response, magnetoencephalography (MEG) is a non-invasive, functional neuroimaging technique that directly measures the magnetic fields produced by the electric currents of activated neurons, using sensitive magnetometers. MEG data is collected with a high temporal resolution, typically in milliseconds, using roughly 300-channel MEG system. The higher number of channels in MEG compared with electroencephalogram (EEG) data allows the use of source reconstruction techniques in order to reconstruct the 3D brain volume at each time instant, as shown in Fig. 8.1(a). Although the choice of technique for source localization in MEG analysis is a fairly new area and research topic in itself, the

analysis on the reconstructed results has shown interesting results in terms of identifying functional networks similar to fMRI [124, 143, 144].

Fusion of multiple sensors or modalities in order to understand the common aspects of multiple sensors and identify the unique contributions of each sensor is important in many applications [145–147]. However a primary issue in data fusion is identifying a common dimension in order to exploit the complementary information across modalities [145]. Since MEG data can be reconstructed to obtain a 3D volume similar to fMRI, fusion of these two modalities along the spatial dimension becomes possible and enables the use of data-driven techniques such as IVA. An individual analysis on fMRI and MEG data has revealed that these two modalities share networks that have a high betweenness centrality, *i.e.*, the networks forming central hubs in cognitive processes [144]. The common networks also correspond to low frequency bands, since fMRI captures low frequency fluctuations (0.01 to 0.15 Hz) and MEG captures a range of low to high frequency fluctuations (0.1 to 330 Hz) .

Through fusion of these modalities, we can study the common and distinct networks across different frequency bands in a data-driven manner. In neuroimaging studies, the frequency bands are commonly divided into delta (0.5 to 4 Hz), theta (4 to 7 Hz), alpha (8 to 12 Hz), beta (16 to 31 Hz) and gamma (32 to 100 Hz). In order to extract features from each modality, we propose to compute the average power using the temporal signatures at each voxel, within different frequency bands, namely, low frequency from fMRI (0.01 to 0.15 Hz), and delta, theta, alpha, beta and gamma bands from MEG, as shown in Fig. 8.1(b). The features within a frequency band obtained from all subjects can be grouped together to form datasets, $\mathbf{X}^{[k]}$, in IVA. The IVA model in Fig. 8.1(c) takes advantage of the dependence structure across different frequency bands and modalities. This model also allows identification of networks that demonstrate significant differences between two groups of

subjects, conditions, or between task-related vs resting-state data, or multiple groups, *e.g.*, eyes-open vs eyes-closed vs task, within each modality and frequency bands. Using this setup, an SCV corresponds to the components that are common across different frequency bands. The dependence structure of the estimated SCVs, thus, can be further analyzed to identify common, distinct networks and the networks that are common to a certain group of frequency bands using the method proposed in [148].

### 8.2.2 Application of decision trees to fill missing value and identify sub-groups

**Filling missing values** Handling missing data in datasets is a challenging task observed in many applications and can significantly affect the results. The causes of missing values can be from no response from the individual due to privacy constraints, human error while filling datasets, and dropout of individuals from a studies of longer duration. One way to handle missing data is to remove the entire observation with missing values. However, this results in loss of information and is not feasible in datasets with less observations to begin with. Other ways include filling the missing value with the mean or median value computed across the observations within a certain target group. Although this is a simpler approach, it might be biased and does not account for other feature values, *i.e.*, the missing value might depend on other features along with the target value.

In this work, we propose the use of decision trees to fill missing entries, as a possible future direction. Given a dataset, we train a decision tree using the observations with no missing entries. An example of a trained decision tree is shown in Fig. 8.2. The example shown in Fig. 8.2 is a simple example of predicting an individual's mood based on different features. The attributes contain categorical values in this example that can be easily distinguished, however in many cases the attributes contain continuous values, for which a decision tree computes a threshold based on the target classes, to obtain sub-trees.

As a first step towards filling a missing value for a observation, we traverse along the

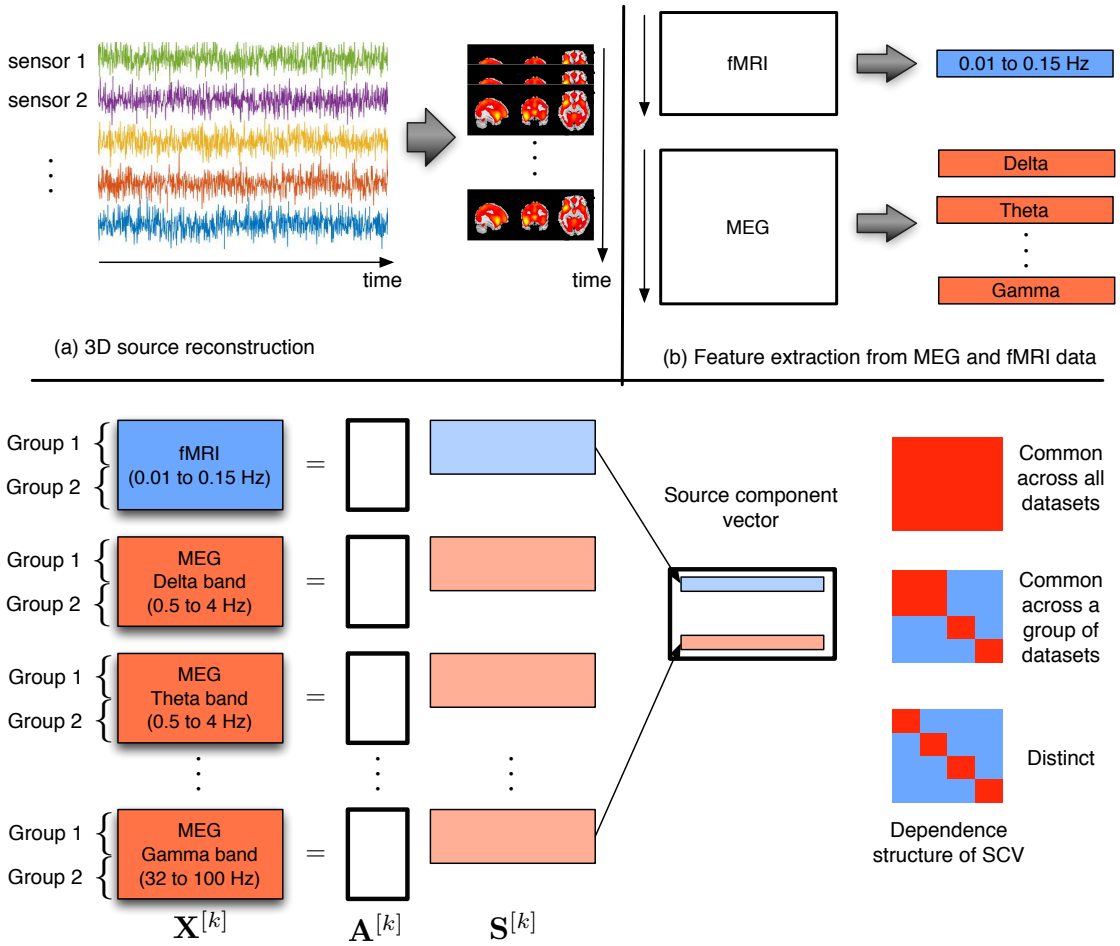


FIG. 8.1. IVA model for fusion of fMRI and MEG source reconstructed data. (a) The MEG data collected from sensors as a function of time, is reconstructed to obtain a 3D volume at each time instant, resulting in a high spatial and temporal resolution. (b) In order to extract features from each modality, we propose to compute the average power using the temporal signatures at each voxel, within different frequency bands, namely, low frequency from fMRI (0.01 to 0.15 Hz), and delta, theta, alpha, beta and gamma bands from MEG. (c) The features within a frequency band obtained from all subjects can be grouped together to form datasets, $\mathbf{X}^{[k]}$, in IVA. This model allows for the analysis of two groups within each dataset, *e.g.*, resting-state vs task, patients vs controls, eyes-open vs eyes-closed, or multiple groups, *e.g.*, eyes-open vs eyes-closed vs task. Applying IVA on this set up results in sources that are independent within each frequency band and dependent across frequency bands. The dependence structure across datasets can be further analyzed to identify common and distinct component.

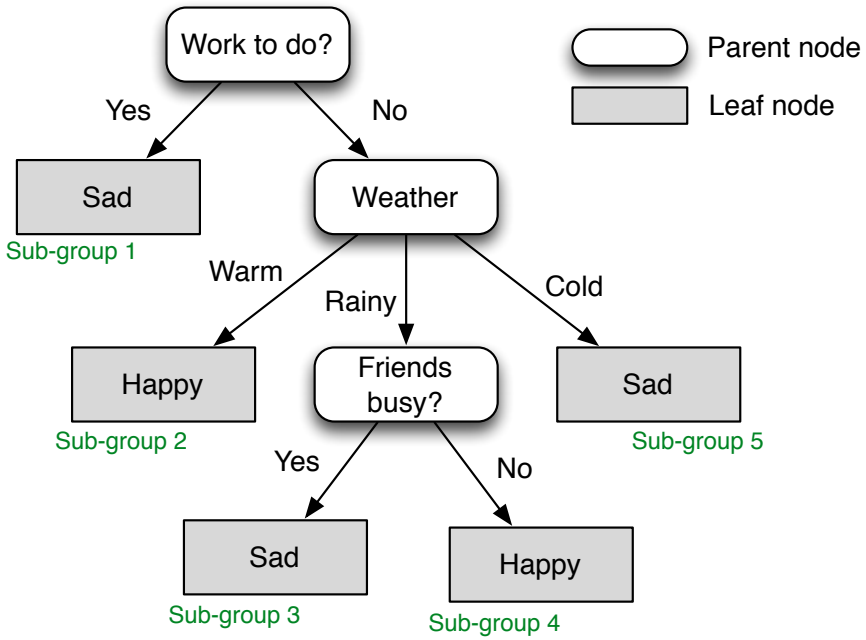


FIG. 8.2. Example of a decision tree for predicting the mood of an individual. The tree is trained on the observations with no missing values. All parent nodes represent an attribute and a leaf node represent the target value achieved.

tree to reach possible leaf nodes, as shown in Fig. 8.3(a). The idea behind this is to selected a set of possible leaf nodes we would have reached if we knew the value of the missing entry. Each leaf node is associated with a cluster consisting of similar observations, which are obtained from the training stage. Depending on the number of leaf nodes selected, we form equivalent number of clusters. Next, we fill the missing entry with the average, median or highest probable value within that cluster, as shown in Fig. 8.3(b). We obtain a new observation based on each cluster, labeled as observation 'A' and 'B' in Fig. 8.3(b). Finally, we compute the distance between each new observation and the cluster centroids in order to find the least distance. We select the observation that has the least distance to any of the cluster centroid. The advantage of this method is that it makes use of all the features to fill the missing value, which may result in a more accurate value.

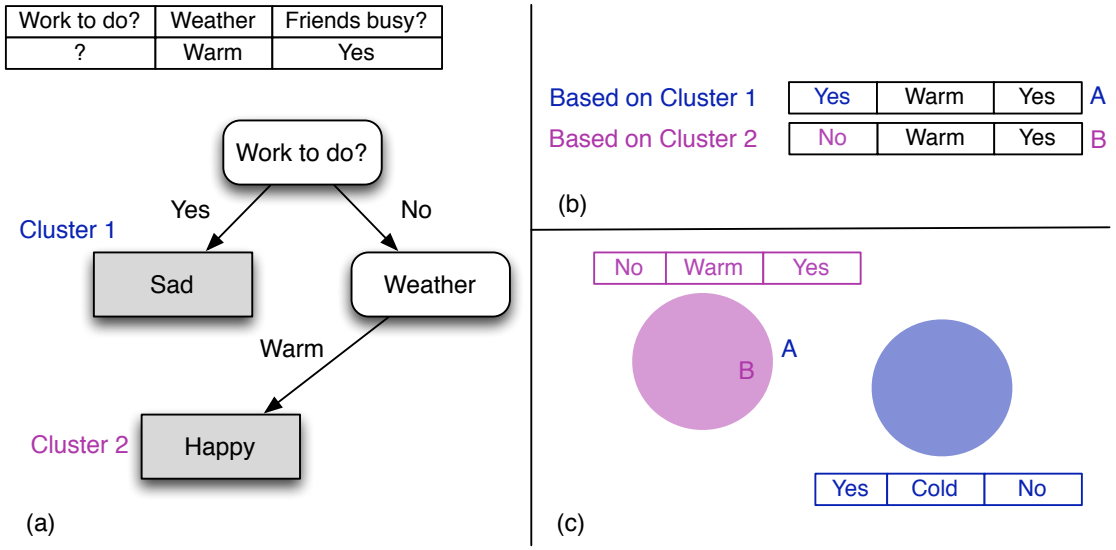


FIG. 8.3. Steps to fill the missing value. In this example, the observation has no value for the attribute 'Work to do?'. (a) As a first step, we traverse along the tree to reach possible leaf nodes. The possible leaf nodes are the nodes to which we would have reached if we knew the entry for the missing value. The observations at each leaf node are grouped into a cluster. (b) Fill the missing entry based on the median or highest occurring value in the missing attribute from each cluster. We thus obtain a new observation for each cluster, denoted as observation 'A' and 'B'. (c) Select the observation that is closest to any of the selected cluster from step (a). In this example, we fill the missing value with 'No' corresponding to observation 'A'.

**Identification of sub-groups** Studies have revealed sub-groups of patients with schizophrenia and there is a significant interest in identifying the attributes that distinguish the sub-types of patients. Decision trees can be used to identify sub-groups of subjects and for investigating the attributes that are common and distinct for each sub-group. From the example shown in Fig 8.2, we can say that sub-groups 1, 3 and 5 are part of a bigger group ('Sad'), however are separated into different leaf nodes due to differences in certain attributes. Sub-group 3 and 5 share a common attribute 'Work to do?', but need attributes 'Weather' and 'Friends busy?' to distinguish themselves. For identifying sub-groups of patients, we can form a decision tree using the clinical scores, subject covariations or a fusion

of the two, as attributes and subject class, such as healthy or patient, as target attribute. The resulting decision tree will then identify sub-groups of patients, and the attributes that are common and distinct.

### 8.2.3 Interpretation of Lagrange Multipliers

In this work, we propose the use of an augmented Lagrangian optimization framework to incorporate constraints into the IVA cost function. However, there are other simpler but powerful constrained optimization techniques to incorporate constraints such as penalty function method and method of Lagrange multipliers. While both techniques have their pros and cons, the use of method of Lagrange multipliers allows for analyzing the estimated Lagrange multiplers and studying different aspects of the problem. In order to understand the role of the Lagrange multiplier in the constrained optimization problem, consider the following example.

Given a function $f(x)$, we want to find the optimum value for $x$ that minimizes or maximizes the function subject to a constraint, $g(x) \leq \rho$. The cost function for the method of Lagrange multipliers can be written as,

$$\mathcal{L}(x) = f(x) - \mu\,(g(x) - \rho)$$

Let $x^*$ denote the optimum value of $f(x)$. It is natural to say that the optimum value depends on the constraint parameter, $\rho$, and hence we can write $x^*(\rho)$ as the optimum value of function $f(x)$ for a given value of $\rho$. The relation between the Lagrange multiplier, $\mu$ and function $f(x)$ is given as,

$$\frac{\partial f\,(x^*(\rho))}{\partial \rho} = \mu.$$

Hence, the value of $\mu$ indicates the rate of change of function $f$ for a change in the constraint parameter $\rho$. In other words, it indicates how sensitive the cost function is to

the given constraint. The Lagrange multipliers can have different interpretations in different applications, *e.g.*, in revenue maximization problem, the objective is to maximize revenue under a certain budget constraint. The interpretation of Lagrange multipliers in this problem is "how much more money we can get by changing the budget".

In the context of neuroimaging analysis, the Lagrange multipliers can be interpreted as how sensitive the ICA/IVA cost function is to a change in the constraint parameter for a particular functional network. Note that this formulation makes use of a fixed value for the constraint parameter, and hence makes an inherent assumption that the constraints are accurate. Hence given that the functional networks used as reference signals are accurate, the Lagrange multiplier computed for each constraint can be analyzed further for different groups of individuals or time windows. Since there is high variability among the functional networks across patients with schizophrenia, this variability might be reflected in the estimated value for the Lagrange multiplier.

# APPENDIX

## Appendix A1 : Correlation structures for generating $\mathbf{\Sigma}$

In this dissertation, we use three different structures for generating the correlation matrix, $\mathbf{\Sigma}$.

**AR-type correlation structure** The structure of an $K \times K$ AR-type correlation matrix follows a symmetric Toeplitz structure given as,

$$\mathbf{\Sigma} = \begin{bmatrix} 1 & \psi & \psi^2 & \dots & \psi^{|i-j|} \\ \psi & 1 & \psi & \dots & \psi^{|i-j|} \\ \psi^2 & \psi & 1 & \dots & \psi^{|i-j|} \\ \vdots & \vdots & \vdots & \ddots & \psi^{|i-j|} \\ \psi^{|i-j|} & \psi^{|i-j|} & \dots & \psi & 1 \end{bmatrix}, \tag{8.1}$$

where $i, j$ is the row and column index and $i, j = 1, \dots, K$. This type of structure is more common in analysis of time-series data. The use of this structure for generating a SCV results in sources that are highly correlated across adjacent datasets. This structure is useful in studying dynamics of fMRI data using IVA, where the entire scanning period is divided into subsets of overlapping or non-overlapping adjacent windows and each window forms a dataset in the IVA model. However, this structure must be used for smaller number of datasets and keeping in mind that for a large number of datasets, the elements in the correlation matrix become close to 0.

**Uniform correlation structure** Another form of the correlation structure is the uniform type correlation structure, where the off-diagonal elements are all equal to $\psi$, as fol-

lows,

$$\mathbf{\Sigma} = \begin{bmatrix} 1 & \psi & \psi & \dots & \psi \\ \psi & 1 & \psi & \dots & \psi \\ \psi & \psi & 1 & \dots & \psi \\ \vdots & \vdots & \vdots & \ddots & \psi \\ \psi & \psi & \psi & \dots & 1 \end{bmatrix}. \tag{8.2}$$

This structure can be used for the analysis of a large number of datasets, however the number of datasets, $K$, and choice of the correlation parameter, $\psi$, play an important role in defining the positive definiteness of the matrix.

A positive definite matrix is a matrix whose eigenvalues are non-negative. For a $K \times K$ correlation matrix defined by (8.2), the $K - 1$ eigenvalues are equal to $1 - \psi$ and one eigenvalue is equal to $1 + (K - 1)\psi$. For all eigenvalues to be greater than or equal to zero, we get $1 - \psi \geq 0$ and $1 + (K - 1)\psi \geq 0$. This defines a bound on $\psi$ with respect to $K$ given as,

$$-\frac{1}{K-1} \leq \psi \leq 1$$

We plot the lower bound for $\psi$ with respect to the number of datasets, $K$, in Fig.A4 Hence, for the uniform structure, one must be careful of negative correlation for a higher value of $K$.

**Random correlation structure** The random correlation structure guarantees the correlation structure is positive definite and can be used for large number of datasets. The correlation matrix is generated as $\mathbf{\Sigma} = \mathbf{Q}\mathbf{Q}^T$, where the elements of the matrix $\mathbf{Q}$, $q_{ij}$ are generated from a certain distribution. Depending on the choice of the distribution and the parameters for the distribution, the distribution of the elements in $\mathbf{\Sigma}$ varies. We use this structure for analysis of high dimensional datasets in Chapters 3 and 5. We use different

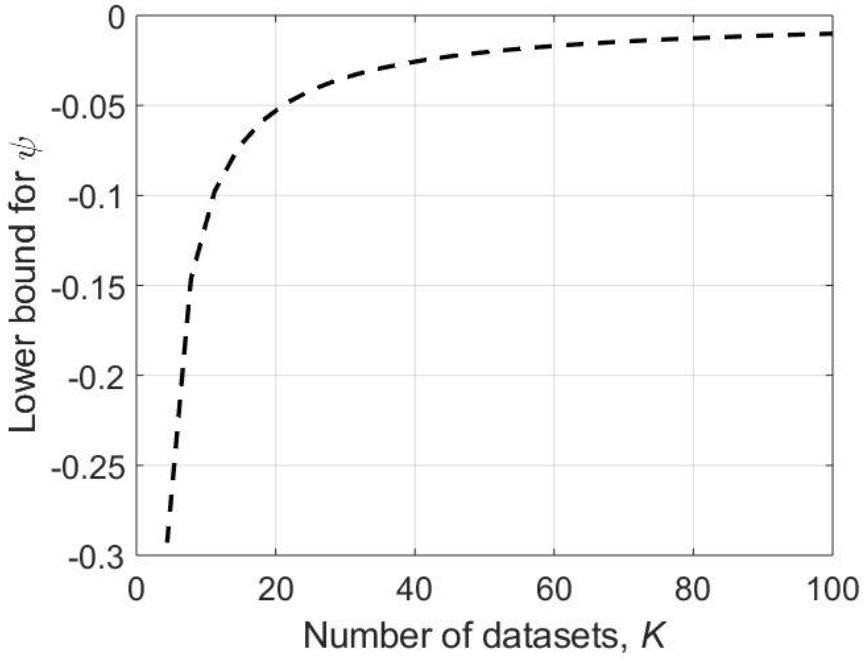


FIG. A4. Lower bound for $\psi$ for the correlation matrix to be positive definite.

distributions and parameters to generate the elements in **Q** and is discussed in detail in Chapters 3.

## Appendix A2 : Reference signal and estimated sources from large scale fMRI data

We select $L = 42$ group-level independent components corresponding to functionally relevant resting-state networks by visual inspection and these components are used as reference signals in acIVA. We apply acIVA on fMRI data from male and female group separately and compute the sources using the demixing matrices from the most consistent run. The $n$th SCV is obtained by grouping together the $n$th source from each dataset. We then perform a one-sample $t$-test across the subject dimension for each voxel and note the $t$-statistic of the significantly ($p < 0.05$) activated voxels. We then visually compared these thresholded maps with the reference signal. Out of the 42 components, 36 matched the reference signal while the remaining 6 components included motion artifacts. The thresholded maps and the corresponding reference signal for the 36 matched components are shown in Fig. A5 and Fig. A6, while 6 unmatched components are shown in Fig. A7.

As observed in Fig. A7, the estimated components included motion artifacts for either male or female groups (IC 3, 4 and 5) or both groups (ICA 1 and 2). However, the corresponding reference signal shows activation around the surface of the brain coinciding with the motion artifact, which affected the estimation performance.

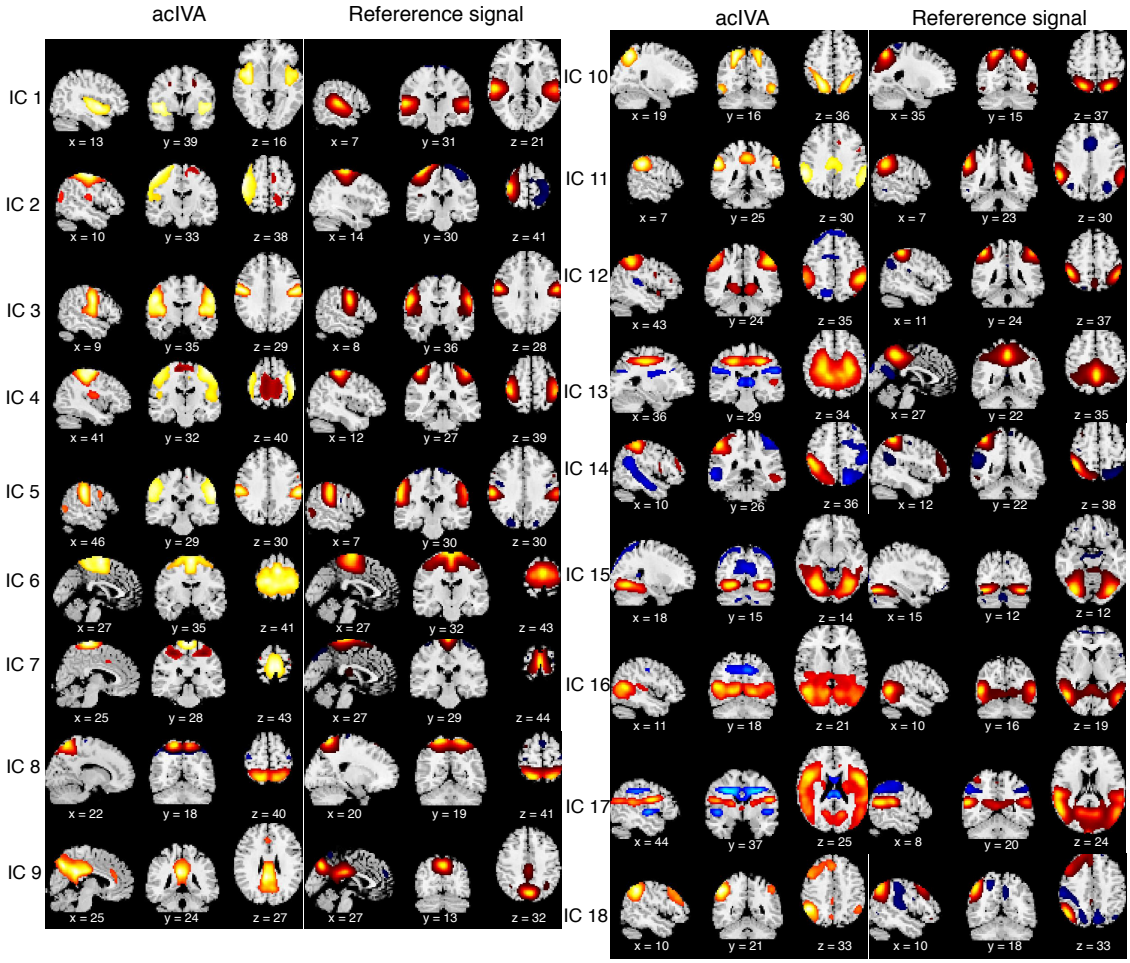


FIG. A5. 18 out of the total 36 matched component from acIVA and corresponding reference signal. The slices corresponding to the peak voxel co-ordinate across the sagittal, coronal and transverse planes,indicated by 'x', 'y', 'z' respectively.

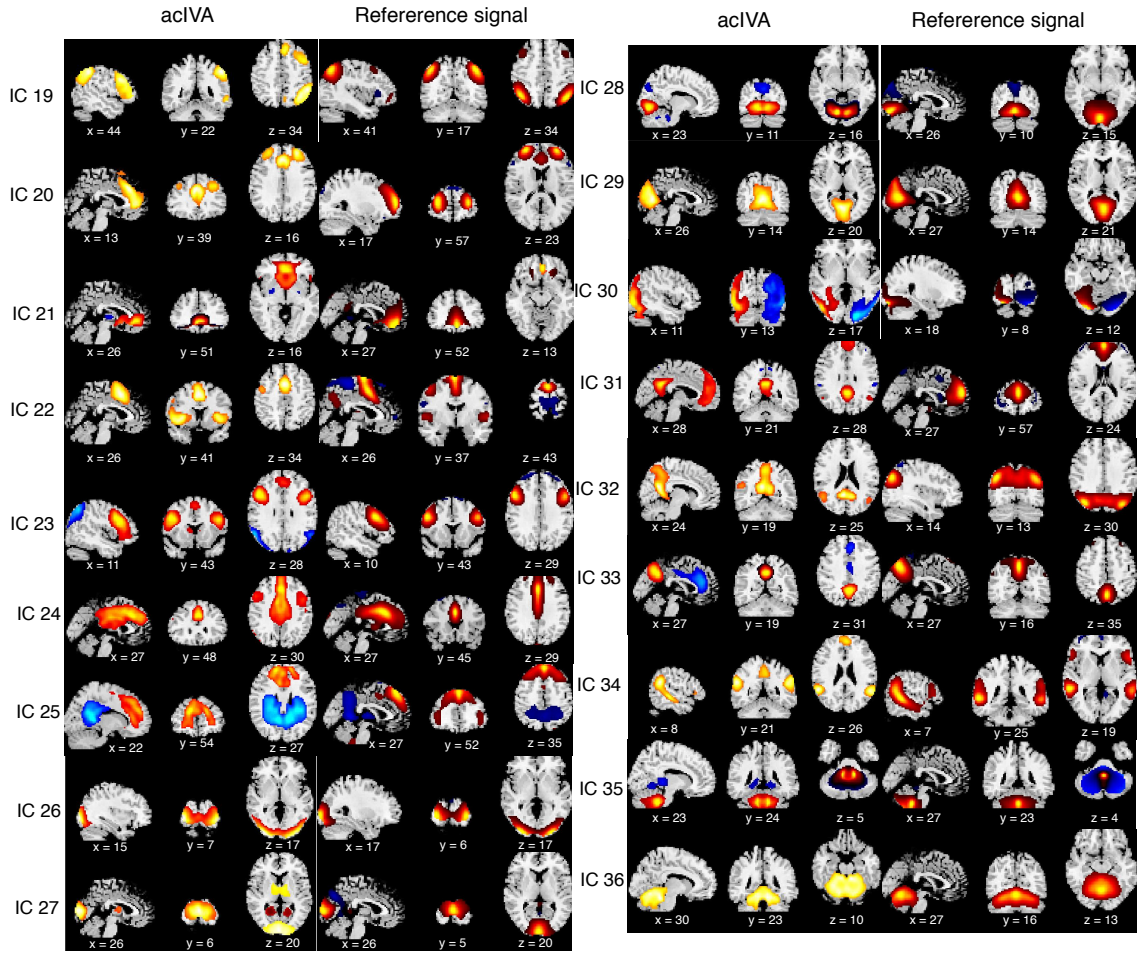


FIG. A6. Remaining 18 out of the total 36 matched components from acIVA and corresponding reference signal. The slices corresponding to the peak voxel co-ordinate across the sagittal, coronal and transverse planes,indicated by 'x', 'y', 'z' respectively.

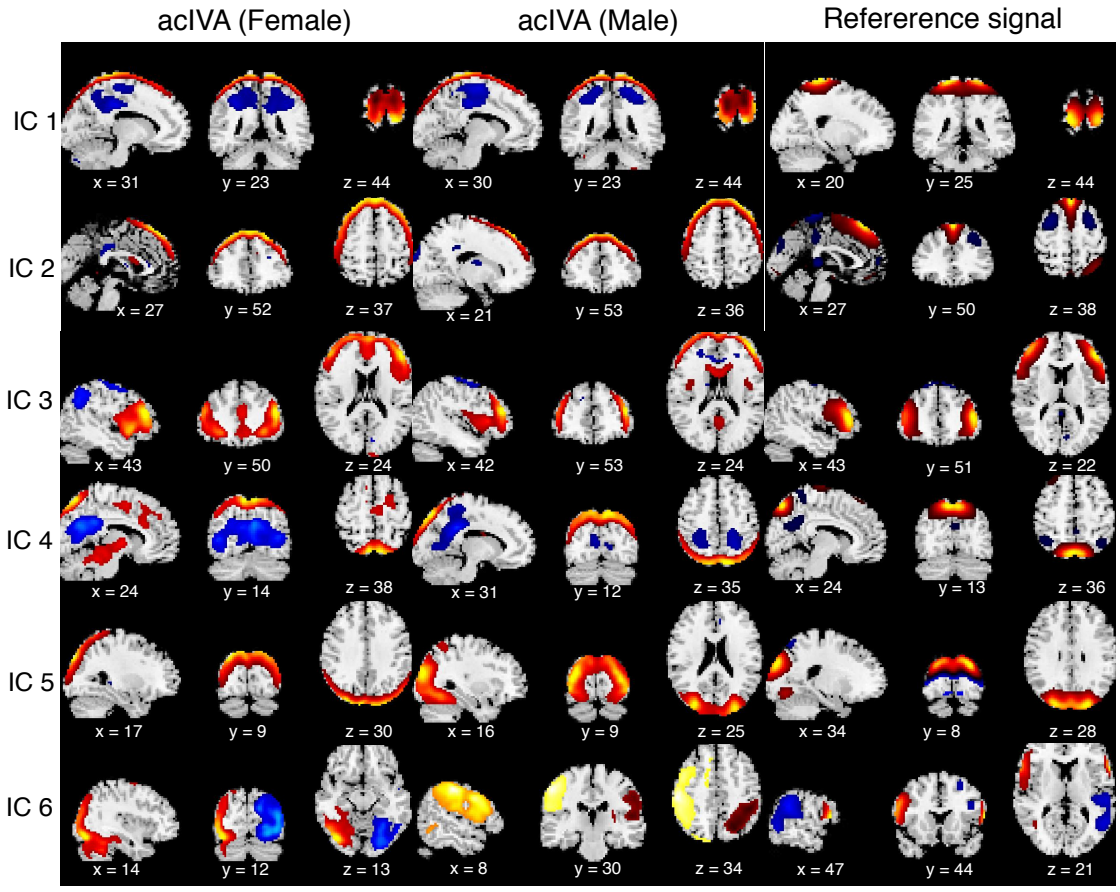


FIG. A7. Six unmatched components from acIVA for female and male groups, and the corresponding reference signal. The slices corresponding to the peak voxel co-ordinate across the sagittal, coronal and transverse planes,indicated by 'x', 'y', 'z' respectively. As observed, the estimated components consist of motion artifacts for either male or female group, or both.

# REFERENCES


[1] M. P. Van Den Heuvel and H. E. H. Pol, "Exploring the brain network: A review on resting-state fMRI functional connectivity," *European Neuropsychopharmacology*, vol. 20, no. 8, pp. 519–534, 2010.

[2] M. R. Arbabshirani and V. D. Calhoun, "Functional network connectivity during rest and task: Comparison of healthy controls and schizophrenic patients," in *Annual International Conference of the Engineering in Medicine and Biology Society (EMBC)*, pp. 4418–4421, IEEE, 2011.

[3] C. Sheng, M. Xia, H. Yu, Y. Huang, Y. Lu, F. Liu, Y. He, and Y. Han, "Abnormal global functional network connectivity and its relationship to medial temporal atrophy in patients with amnestic mild cognitive impairment," *PloS one*, vol. 12, no. 6, p. e0179823, 2017.

[4] M. Pievani, W. de Haan, T. Wu, W. W. Seeley, and G. B. Frisoni, "Functional network disruption in the degenerative dementias," *The Lancet Neurology*, vol. 10, no. 9, pp. 829–843, 2011.

[5] X. Wu, R. Li, A. S. Fleisher, E. M. Reiman, X. Guan, Y. Zhang, K. Chen, and L. Yao, "Altered default mode network connectivity in Alzheimer's disease — a resting functional MRI and Bayesian network study," *Human Brain Mapping*, vol. 32, no. 11, pp. 1868–1881, 2011.

[6] L. Cerliani, M. Mennes, R. M. Thomas, A. Di Martino, M. Thioux, and C. Keysers, "Increased functional connectivity between subcortical and cortical resting-state net-

works in autism spectrum disorder," *JAMA psychiatry*, vol. 72, no. 8, pp. 767–777, 2015.

[7] V. D. Calhoun and N. de Lacy, "Ten key observations on the analysis of resting-state functional MR imaging data using independent component analysis," *NeuroImaging Clinics*, vol. 27, no. 4, pp. 561–579, 2017.

[8] V. D. Calhoun and T. Adalı, "Multisubject independent component analysis of fMRI: A decade of intrinsic networks, default mode, and neurodiagnostic discovery," *IEEE Reviews in Biomedical Engineering*, vol. 5, pp. 60–73, 2012.

[9] V. D. Calhoun, T. Adalı, G. Pearlson, and J. Pekar, "Group ICA of functional MRI data: Separability, stationarity, and inference," in *Proc. Int. Conf. on ICA and BSS San Diego, CA. p*, vol. 155, 2001.

[10] V. D. Calhoun, T. Adalı, G. D. Pearlson, and J. Pekar, "A method for making group inferences from functional MRI data using independent component analysis," *Human Brain Mapping*, vol. 14, no. 3, pp. 140–151, 2001.

[11] J. Laney, K. P. Westlake, S. Ma, E. Woytowicz, V. D. Calhoun, and T. Adalı, "Capturing subject variability in fMRI data: A graph-theoretical analysis of GICA vs. IVA," *Journal of neuroscience methods*, vol. 247, pp. 32–40, 2015.

[12] A. M. Michael, M. Anderson, R. L. Miller, T. Adalı, and V. D. Calhoun, "Preserving subject variability in group fMRI analysis: Performance evaluation of GICA vs. IVA," *Frontiers in Systems Neuroscience*, vol. 8, p. 106, 2014.

[13] T. Adali, M. Anderson, and G.-S. Fu, "Diversity in independent component and vector analyses: Identifiability, algorithms, and applications in medical imaging," *IEEE Signal Processing Magazine*, vol. 31, no. 3, pp. 18–33, 2014.

[14] R. M. Hutchison, T. Womelsdorf, J. S. Gati, S. Everling, and R. S. Menon, "Resting-state networks show dynamic functional connectivity in awake humans and anesthetized macaques," *Human Brain Mapping*, vol. 34, no. 9, pp. 2154–2177, 2013.

[15] Ü. Sakoğlu, G. D. Pearlson, K. A. Kiehl, Y. M. Wang, A. M. Michael, and V. D. Calhoun, "A method for evaluating dynamic functional network connectivity and task-modulation: Application to schizophrenia," *Magnetic Resonance Materials in Physics, Biology and Medicine*, vol. 23, no. 5-6, pp. 351–366, 2010.

[16] A. Kucyi and K. D. Davis, "Dynamic functional connectivity of the default mode network tracks daydreaming," *NeuroImage*, vol. 100, pp. 471–480, 2014.

[17] L. Wang, C. Yu, H. Chen, W. Qin, Y. He, F. Fan, Y. Zhang, M. Wang, K. Li, Y. Zang, *et al.*, "Dynamic functional reorganization of the motor execution network after stroke," *Brain*, vol. 133, no. 4, pp. 1224–1238, 2010.

[18] V. D. Calhoun, R. Miller, G. Pearlson, and T. Adalı, "The chronnectome: Time-varying connectivity networks as the next frontier in fMRI data discovery," *Neuron*, vol. 84, no. 2, pp. 262–274, 2014.

[19] E. A. Allen, E. Damaraju, S. M. Plis, E. B. Erhardt, T. Eichele, and V. D. Calhoun, "Tracking whole-brain connectivity dynamics in the resting state," *Cerebral Cortex*, vol. 24, no. 3, pp. 663–676, 2014.

[20] E. Damaraju, E. A. Allen, A. Belger, J. Ford, S. McEwen, D. Mathalon, B. Mueller, G. Pearlson, S. Potkin, A. Preda, *et al.*, "Dynamic functional connectivity analysis reveals transient states of dysconnectivity in schizophrenia," *NeuroImage: Clinical*, vol. 5, pp. 298–308, 2014.

[21] B. Rashid, E. Damaraju, G. D. Pearlson, and V. D. Calhoun, "Dynamic connectivity states estimated from resting fMRI identify differences among Schizophrenia, bipolar disorder, and healthy control subjects," *Frontiers in Human Neuroscience*, vol. 8, p. 897, 2014.

[22] M. Assaf, K. Jagannathan, V. D. Calhoun, L. Miller, M. C. Stevens, R. Sahl, J. G. O'Boyle, R. T. Schultz, and G. D. Pearlson, "Abnormal functional connectivity of default mode sub-networks in autism spectrum disorder patients," *NeuroImage*, vol. 53, no. 1, pp. 247–256, 2010.

[23] Z. Fu, Y. Tu, X. Di, Y. Du, J. Sui, B. B. Biswal, Z. Zhang, N. de Lacy, and V. D. Calhoun, "Transient increased thalamic-sensory connectivity and decreased whole-brain dynamism in autism," *NeuroImage*, 2018.

[24] C. Jin, H. Jia, P. Lanka, D. Rangaprakash, L. Li, T. Liu, X. Hu, and G. Deshpande, "Dynamic brain connectivity is a better predictor of PTSD than static connectivity," *Human Brain Mapping*, vol. 38, no. 9, pp. 4479–4496, 2017.

[25] R. L. Bluhm, P. C. Williamson, E. A. Osuch, P. A. Frewen, T. K. Stevens, K. Boksman, R. W. Neufeld, J. Théberge, and R. A. Lanius, "Alterations in default network connectivity in post-traumatic stress disorder related to early-life trauma," *Journal of Psychiatry & Neuroscience: JPN*, vol. 34, no. 3, p. 187, 2009.

[26] A. Etkin, K. E. Prater, A. F. Schatzberg, V. Menon, and M. D. Greicius, "Disrupted amygdalar subregion functional connectivity and evidence of a compensatory network in generalized anxiety disorder," *Archives of General Psychiatry*, vol. 66, no. 12, pp. 1361–1372, 2009.

[27] N. de Lacy and V. D. Calhoun, "Dynamic connectivity and the effects of maturation

in youth with attention deficit hyperactivity disorder," *Network Neuroscience*, vol. 3, no. 1, pp. 195–216, 2018.

[28] X. Chen, H. Zhang, Y. Gao, C.-Y. Wee, G. Li, D. Shen, and A. D. N. Initiative, "High-order resting-state functional connectivity network for MCI classification," *Human Brain Mapping*, vol. 37, no. 9, pp. 3282–3296, 2016.

[29] L. Q. Uddin, K. S. Supekar, S. Ryali, and V. Menon, "Dynamic reconfiguration of structural and functional connectivity across core neurocognitive brain networks with development," *Journal of Neuroscience*, vol. 31, no. 50, pp. 18578–18589, 2011.

[30] S. Lefebvre, M. Demeulemeester, A. Leroy, C. Delmaire, R. Lopes, D. Pins, P. Thomas, and R. Jardri, "Network dynamics during the different stages of hallucinations in schizophrenia," *Human Brain Mapping*, vol. 37, no. 7, pp. 2571–2586, 2016.

[31] B. Jie, M. Liu, and D. Shen, "Integration of temporal and spatial properties of dynamic connectivity networks for automatic diagnosis of brain disease," *Medical Image Analysis*, vol. 47, pp. 81–94, 2018.

[32] A. Kottaram, L. Johnston, E. Ganella, C. Pantelis, R. Kotagiri, and A. Zalesky, "Spatio-temporal dynamics of resting-state brain networks improve single-subject prediction of schizophrenia diagnosis," *Human Brain Mapping*, 2018.

[33] J. M. Kunert-Graf, K. M. Eschenburg, D. J. Galas, J. N. Kutz, S. D. Rane, and B. W. Brunton, "Extracting reproducible time-resolved resting state networks using dynamic mode decomposition," *bioRxiv*, p. 343061, 2018.

[34] Z. Yang, R. C. Craddock, D. S. Margulies, C.-G. Yan, and M. P. Milham, "Common intrinsic connectivity states among posteromedial cortex subdivisions: Insights from analysis of temporal dynamics," *NeuroImage*, vol. 93, pp. 124–137, 2014.

[35] I. Cribben, R. Haraldsdottir, L. Y. Atlas, T. D. Wager, and M. A. Lindquist, "Dynamic connectivity regression: Determining state-related changes in brain connectivity," *NeuroImage*, vol. 61, no. 4, pp. 907–920, 2012.

[36] L. E. Mash, A. C. Linke, L. A. Olson, I. Fishman, T. T. Liu, and R.-A. Müller, "Transient states of network connectivity are atypical in autism: A dynamic functional connectivity study," *Human Brain Mapping*, vol. 40, no. 8, pp. 2377–2389, 2019.

[37] A. D. Barber, M. A. Lindquist, P. DeRosse, and K. H. Karlsgodt, "Dynamic functional connectivity states reflecting psychotic-like experiences," *Biological Psychiatry: Cognitive Neuroscience and Neuroimaging*, vol. 3, no. 5, pp. 443–453, 2018.

[38] V. Harlalka, R. S. Bapi, P. Vinod, and D. Roy, "Atypical flexibility in dynamic functional connectivity quantifies the severity in autism spectrum disorder," *Frontiers in Human Neuroscience*, vol. 13, p. 6, 2019.

[39] F. G. Hillary, C. A. Roman, U. Venkatesan, S. M. Rajtmajer, R. Bajo, and N. D. Castellanos, "Hyperconnectivity is a fundamental response to neurological disruption.," *Neuropsychology*, vol. 29, no. 1, p. 59, 2015.

[40] B. B. Biswal, M. Mennes, X.-N. Zuo, S. Gohel, C. Kelly, S. M. Smith, C. F. Beckmann, J. S. Adelstein, R. L. Buckner, S. Colcombe, *et al.*, "Toward discovery science of human brain function," *Proceedings of the National Academy of Sciences*, vol. 107, no. 10, pp. 4734–4739, 2010.

[41] S.-J. Kim, V. D. Calhoun, and T. Adalı, "Flexible large-scale fMRI analysis: A survey," in *2017 IEEE International Conference on Acoustics, Speech and Signal Processing (ICASSP)*, pp. 6319–6323, 2017.

[42] E. S. Finn, X. Shen, D. Scheinost, M. D. Rosenberg, J. Huang, M. M. Chun, X. Papademetris, and R. T. Constable, "Functional connectome fingerprinting: Identifying individuals using patterns of brain connectivity," *Nature Neuroscience*, vol. 18, no. 11, p. 1664, 2015.

[43] R. S. Desikan, F. Ségonne, B. Fischl, B. T. Quinn, B. C. Dickerson, D. Blacker, R. L. Buckner, A. M. Dale, R. P. Maguire, B. T. Hyman, *et al.*, "An automated labeling system for subdividing the human cerebral cortex on MRI scans into gyral based regions of interest," *NeuroImage*, vol. 31, no. 3, pp. 968–980, 2006.

[44] N. Tzourio-Mazoyer, B. Landeau, D. Papathanassiou, F. Crivello, O. Etard, N. Delcroix, B. Mazoyer, and M. Joliot, "Automated anatomical labeling of activations in SPM using a macroscopic anatomical parcellation of the MNI MRI single-subject brain," *NeuroImage*, vol. 15, no. 1, pp. 273–289, 2002.

[45] B. Thomas Yeo, F. M. Krienen, J. Sepulcre, M. R. Sabuncu, D. Lashkari, M. Hollinshead, J. L. Roffman, J. W. Smoller, L. Zöllei, J. R. Polimeni, *et al.*, "The organization of the human cerebral cortex estimated by intrinsic functional connectivity," *Journal of Neurophysiology*, vol. 106, no. 3, pp. 1125–1165, 2011.

[46] C. Baldassano, D. M. Beck, and L. Fei-Fei, "Parcellating connectivity in spatial maps," *PeerJ*, vol. 3, p. e784, 2015.

[47] L. Fan, H. Li, J. Zhuo, Y. Zhang, J. Wang, L. Chen, Z. Yang, C. Chu, S. Xie, A. R.

Laird, *et al.*, "The human brainnetome atlas: a new brain atlas based on connectional architecture," *Cerebral Cortex*, vol. 26, no. 8, pp. 3508–3526, 2016.

[48] E. M. Gordon, T. O. Laumann, B. Adeyemo, J. F. Huckins, W. M. Kelley, and S. E. Petersen, "Generation and evaluation of a cortical area parcellation from resting-state correlations," *Cerebral Cortex*, vol. 26, no. 1, pp. 288–303, 2014.

[49] A. J. Bell and T. J. Sejnowski, "An information-maximization approach to blind separation and blind deconvolution," *Neural Computation*, vol. 7, no. 6, pp. 1129–1159, 1995.

[50] A. Hyvarinen, "Fast and robust fixed-point algorithms for independent component analysis," *IEEE Transactions on Neural Networks*, vol. 10, no. 3, pp. 626–634, 1999.

[51] X.-L. Li and T. Adalı, "Independent component analysis by entropy bound minimization," *IEEE Transactions on Signal Processing*, vol. 58, no. 10, pp. 5151–5164, 2010.

[52] X.-L. Li and T. Adalı, "Blind spatiotemporal separation of second and/or higher-order correlated sources by entropy rate minimization," in *International Conference on Acoustics Speech and Signal Processing (ICASSP)*, pp. 1934–1937, IEEE, 2010.

[53] G.-S. Fu, R. Phlypo, M. Anderson, X.-L. Li, *et al.*, "Blind source separation by entropy rate minimization," *IEEE Transactions on Signal Processing*, vol. 62, no. 16, pp. 4245–4255, 2014.

[54] W. Du, H. Li, X.-L. Li, V. D. Calhoun, and T. Adalı, "ICA of fMRI data: Performance of three ICA algorithms and the importance of taking correlation information into account," in *2011 IEEE International Symposium on Biomedical Imaging: From Nano to Macro*, pp. 1573–1576, IEEE, 2011.

[55] Q. Long, S. Bhinge, Y. Levin-Schwartz, Z. Boukouvalas, V. D. Calhoun, and T. Adalı, "The role of diversity in data-driven analysis of multi-subject fMRI data: Comparison of approaches based on independence and sparsity using global performance metrics," *Human Brain Mapping*, vol. 40, no. 2, pp. 489–504, 2019.

[56] E. A. Allen, E. B. Erhardt, E. Damaraju, W. Gruner, J. M. Segall, R. F. Silva, M. Havlicek, S. Rachakonda, J. Fries, R. Kalyanam, *et al.*, "A baseline for the multivariate comparison of resting-state networks," *Frontiers in Systems Neuroscience*, vol. 5, p. 2, 2011.

[57] M. Anderson, T. Adalı, and X.-L. Li, "Joint blind source separation with multivariate Gaussian model: Algorithms and performance analysis," *IEEE Transactions on Signal Processing*, vol. 60, no. 4, pp. 1672–1683, 2012.

[58] X.-L. Li and X.-D. Zhang, "Nonorthogonal joint diagonalization free of degenerate solution," *IEEE Transactions on Signal Processing*, vol. 55, no. 5, pp. 1803–1814, 2007.

[59] T. Kim, T. Eltoft, and T.-W. Lee, "Independent vector analysis: An extension of ICA to multivariate components," in *International Conference on Independent Component Analysis and Signal Separation*, pp. 165–172, Springer, 2006.

[60] A. Scott, W. Courtney, D. Wood, R. De la Garza, S. Lane, R. Wang, M. King, J. Roberts, J. A. Turner, and V. D. Calhoun, "COINS: An innovative informatics and neuroimaging tool suite built for large heterogeneous datasets," *Frontiers in NeuroInformatics*, vol. 5, p. 33, 2011.

[61] R. L. Gollub, J. M. Shoemaker, M. D. King, T. White, S. Ehrlich, S. R. Sponheim, V. P. Clark, J. A. Turner, B. A. Mueller, V. Magnotta, *et al.*, "The MCIC collec-

tion: A shared repository of multi-modal, multi-site brain image data from a clinical investigation of schizophrenia," *Neuroinformatics*, vol. 11, no. 3, pp. 367–388, 2013.

[62] E. Gómez, M. Gomez-Viilegas, and J. Marin, "A multivariate generalization of the power exponential family of distributions," *Communications in Statistics-Theory and Methods*, vol. 27, no. 3, pp. 589–600, 1998.

[63] Q. Long, C. Jia, Z. Boukouvalas, B. Gabrielson, D. Emge, and T. Adalı, "Consistent run selection for independent component analysis: Application to fMRI analysis," in *International Conference on Acoustics, Speech and Signal Processing (ICASSP)*, pp. 2581–2585, IEEE, 2018.

[64] A. Zalesky, A. Fornito, and E. T. Bullmore, "Network-based statistic: Identifying differences in brain networks," *NeuroImage*, vol. 53, no. 4, pp. 1197–1207, 2010.

[65] E. Maris and R. Oostenveld, "Nonparametric statistical testing of EEG-and MEG-data," *Journal of Neuroscience Methods*, vol. 164, no. 1, pp. 177–190, 2007.

[66] M. Anderson, *Independent vector analysis: Theory, algorithms, and applications*. PhD thesis, 2013.

[67] S. Bhinge, R. Mowakeaa, V. D. Calhoun, and T. Adalı, "Extraction of time-varying spatio-temporal networks using parameter-tuned constrained IVA," *IEEE Transactions on Medical Imaging*, vol. 38, pp. 1715–1725, July 2019.

[68] V. Kiviniemi, T. Starck, J. Remes, X. Long, J. Nikkinen, M. Haapea, J. Veijola, I. Moilanen, M. Isohanni, Y.-F. Zang, *et al.*, "Functional segmentation of the brain cortex using high model order group PICA," *Human Brain Mapping*, vol. 30, no. 12, pp. 3865–3886, 2009.

[69] A. Abou-Elseoud, T. Starck, J. Remes, J. Nikkinen, O. Tervonen, and V. Kiviniemi, "The effect of model order selection in group PICA," *Human Brain Mapping*, vol. 31, no. 8, pp. 1207–1216, 2010.

[70] P. A. Rodriguez, M. Anderson, X.-L. Li, and T. Adalı, "General non-orthogonal constrained ICA," *IEEE Transactions on Signal Processing*, vol. 62, no. 11, pp. 2778–2786, 2014.

[71] S. Wein, A. Tomé, M. Goldhacker, M. Greenlee, and E. Lang, "Hybridizing EMD with cICA for fMRI Analysis of Patient Groups," in *41st Annual International Conference of the IEEE Engineering in Medicine and Biology Society (EMBC)*, pp. 194–197, IEEE, 2019.

[72] Q.-H. Lin, J. Liu, Y.-R. Zheng, H. Liang, and V. D. Calhoun, "Semiblind spatial ICA of fMRI using spatial constraints," *Human Brain Mapping*, vol. 31, no. 7, pp. 1076–1088, 2010.

[73] Y. Du, Z. Fu, J. Sui, S. Gao, Y. Xing, D. Lin, M. Salman, M. A. Rahaman, A. Abrol, J. Chen, *et al.*, "NeuroMark: An adaptive independent component analysis framework for estimating reproducible and comparable fMRI biomarkers among brain disorders," *medRxiv*, p. 19008631, 2019.

[74] V. D. Calhoun, T. Adali, M. Stevens, K. Kiehl, and J. J. Pekar, "Semi-blind ica of fmri: a method for utilizing hypothesis-derived time courses in a spatial ica analysis," *Neuroimage*, vol. 25, no. 2, pp. 527–538, 2005.

[75] Q.-H. Lin, Y.-R. Zheng, F. Yin, and H.-L. Liang, "Speech segregation using constrained ICA," in *International Symposium on Neural Networks*, pp. 755–760, Springer, 2004.

[76] C. J. James and O. J. Gibson, "Temporally constrained ICA: An application to artifact rejection in electromagnetic brain signal analysis," *IEEE Transactions on Biomedical Engineering*, vol. 50, no. 9, pp. 1108–1116, 2003.

[77] Z.-L. Sun and L. Shang, "An improved constrained ICA with reference based unmixing matrix initialization," *Neurocomputing*, vol. 73, no. 4-6, pp. 1013–1017, 2010.

[78] J.-X. Mi and Y. Xu, "A comparative study and improvement of two ICA using reference signal methods," *Neurocomputing*, vol. 137, pp. 157–164, 2014.

[79] W. Lu and J. C. Rajapakse, "ICA with reference," *Neurocomputing*, vol. 69, no. 16-18, pp. 2244–2257, 2006.

[80] Z.-L. Zhang, "Morphologically constrained ICA for extracting weak temporally correlated signals," *Neurocomputing*, vol. 71, no. 7-9, pp. 1669–1679, 2008.

[81] A. H. Khan, M. Taseska, and E. A. Habets, "A geometrically constrained independent vector analysis algorithm for online source extraction," in *International Conference on Latent Variable Analysis and Signal Separation*, pp. 396–403, Springer, 2015.

[82] S. Bhinge, Q. Long, Y. Levin-Schwartz, Z. Boukouvalas, V. D. Calhoun, and T. Adalı, "Non-orthogonal constrained independent vector analysis: Application to data fusion," in *International Conference on Acoustics, Speech and Signal Processing (ICASSP)*, pp. 2666–2670, March 2017.

[83] A. Cichocki, D. Mandic, L. De Lathauwer, G. Zhou, Q. Zhao, C. Caiafa, and H. A. Phan, "Tensor decompositions for signal processing applications: From two-way to multiway component analysis," *IEEE Signal Processing Magazine*, vol. 32, no. 2, pp. 145–163, 2015.

[84] Y. Levin-Schwartz, V. D. Calhoun, and T. Adalı, "Quantifying the interaction and contribution of multiple datasets in fusion: application to the detection of schizophrenia," *IEEE transactions on medical imaging*, vol. 36, no. 7, pp. 1385–1395, 2017.

[85] E. Acar, Y. Levin-Schwartz, V. D. Calhoun, and T. Adalı, "Tensor-based fusion of EEG and FMRI to understand neurological changes in schizophrenia," in *2017 IEEE International Symposium on Circuits and Systems (ISCAS)*, pp. 1–4, May 2017.

[86] G. Varoquaux, A. Gramfort, F. Pedregosa, V. Michel, and B. Thirion, "Multi-subject dictionary learning to segment an atlas of brain spontaneous activity," in *Biennial International Conference on Information Processing in Medical Imaging*, pp. 562–573, Springer, 2011.

[87] A. H. Phan and A. Cichocki, "PARAFAC algorithms for large-scale problems," *Neurocomputing*, vol. 74, no. 11, pp. 1970–1984, 2011.

[88] S. K. Suter, M. Makhynia, and R. Pajarola, "TAMRESH–tensor approximation multiresolution hierarchy for interactive volume visualization," in *Computer Graphics Forum*, vol. 32, pp. 151–160, Wiley Online Library, 2013.

[89] G.-S. Fu, M. Anderson, and T. Adalı, "Likelihood estimators for dependent samples and their application to order detection," *IEEE Transactions on Signal Processing*, vol. 62, no. 16, pp. 4237–4244, 2014.

[90] D. Sridharan, D. J. Levitin, and V. Menon, "A critical role for the right fronto-insular cortex in switching between central-executive and default-mode networks," *Proceedings of the National Academy of Sciences*, vol. 105, no. 34, pp. 12569–12574, 2008.

[91] V. Menon and L. Q. Uddin, "Saliency, switching, attention and control: a network model of insula function," *Brain Structure and Function*, vol. 214, no. 5-6, pp. 655–667, 2010.

[92] J. R. Andrews-Hanna, J. Smallwood, and R. N. Spreng, "The default network and self-generated thought: component processes, dynamic control, and clinical relevance," *Annals of the New York Academy of Sciences*, vol. 1316, no. 1, pp. 29–52, 2014.

[93] M. D. Fox, A. Z. Snyder, J. L. Vincent, M. Corbetta, D. C. Van Essen, and M. E. Raichle, "The human brain is intrinsically organized into dynamic, anticorrelated functional networks," *Proceedings of the National Academy of Sciences*, vol. 102, no. 27, pp. 9673–9678, 2005.

[94] C. Chang and G. H. Glover, "Time–frequency dynamics of resting-state brain connectivity measured with fMRI," *NeuroImage*, vol. 50, no. 1, pp. 81–98, 2010.

[95] M. H. Lee, C. D. Smyser, and J. S. Shimony, "Resting-state fMRI: A review of methods and clinical applications," *American Journal of Neuroradiology*, vol. 34, no. 10, pp. 1866–1872, 2013.

[96] M. G. Preti, T. A. Bolton, and D. Van De Ville, "The dynamic functional connectome: state-of-the-art and perspectives," *NeuroImage*, vol. 160, pp. 41–54, 2017.

[97] A. O. Hero and B. Rajaratnam, "Foundational principles for large-scale inference: Illustrations through correlation mining," *Proceedings of the IEEE*, vol. 104, no. 1, pp. 93–110, 2016.

[98] N. Leonardi and D. Van De Ville, "On spurious and real fluctuations of dynamic functional connectivity during rest," *Neuroimage*, vol. 104, pp. 430–436, 2015.

[99] R. M. Hutchison, T. Womelsdorf, E. A. Allen, P. A. Bandettini, V. D. Calhoun, M. Corbetta, S. Della Penna, J. H. Duyn, G. H. Glover, J. Gonzalez-Castillo, *et al.*, "Dynamic functional connectivity: Promise, issues, and interpretations," *NeuroImage*, vol. 80, pp. 360–378, 2013.

[100] X. Li, D. Zhu, X. Jiang, C. Jin, X. Zhang, L. Guo, J. Zhang, X. Hu, L. Li, and T. Liu, "Dynamic functional connectomics signatures for characterization and differentiation of PTSD patients," *Human Brain Mapping*, vol. 35, no. 4, pp. 1761–1778, 2014.

[101] S. D. Keilholz, M. E. Magnuson, W.-J. Pan, M. Willis, and G. J. Thompson, "Dynamic properties of functional connectivity in the rodent," *Brain Connectivity*, vol. 3, no. 1, pp. 31–40, 2013.

[102] R. Liégeois, E. Ziegler, C. Phillips, P. Geurts, F. Gómez, M. A. Bahri, B. T. Yeo, A. Soddu, A. Vanhaudenhuyse, S. Laureys, *et al.*, "Cerebral functional connectivity periodically (de) synchronizes with anatomical constraints," *Brain Structure and Function*, vol. 221, no. 6, pp. 2985–2997, 2016.

[103] V. D. Calhoun, K. A. Kiehl, and G. D. Pearlson, "Modulation of temporally coherent brain networks estimated using ICA at rest and during cognitive tasks," *Human Brain Mapping*, vol. 29, no. 7, pp. 828–838, 2008.

[104] S. Ma, V. D. Calhoun, R. Phlypo, and T. Adalı, "Dynamic changes of spatial functional network connectivity in healthy individuals and schizophrenia patients using independent vector analysis," *NeuroImage*, vol. 90, pp. 196–206, 2014.

[105] D. Cordes, V. M. Haughton, K. Arfanakis, J. D. Carew, P. A. Turski, C. H. Moritz, M. A. Quigley, and M. E. Meyerand, "Frequencies contributing to functional con-

nectivity in the cerebral cortex in resting-state data," *American Journal of Neuroradiology*, vol. 22, no. 7, pp. 1326–1333, 2001.

[106] R. Bluhm, P. Williamson, R. Lanius, J. Théberge, M. Densmore, R. Bartha, R. Neufeld, and E. Osuch, "Resting state default-mode network connectivity in early depression using a seed region-of-interest analysis: Decreased connectivity with caudate nucleus," *Psychiatry and Clinical Neurosciences*, vol. 63, no. 6, pp. 754–761, 2009.

[107] L. Q. Uddin, A. Clare Kelly, B. B. Biswal, F. Xavier Castellanos, and M. P. Milham, "Functional connectivity of default mode network components: Correlation, anticorrelation, and causality," *Human Brain Mapping*, vol. 30, no. 2, pp. 625–637, 2009.

[108] L. J. Larson-Prior, J. M. Zempel, T. S. Nolan, F. W. Prior, A. Z. Snyder, and M. E. Raichle, "Cortical network functional connectivity in the descent to sleep," *Proceedings of the National Academy of Sciences*, vol. 106, no. 11, pp. 4489–4494, 2009.

[109] Y. I. Sheline, J. L. Price, Z. Yan, and M. A. Mintun, "Resting-state functional MRI in depression unmasks increased connectivity between networks via the dorsal nexus," *Proceedings of the National Academy of Sciences*, vol. 107, no. 24, pp. 11020–11025, 2010.

[110] P. Lin, Y. Yang, J. Gao, N. De Pisapia, S. Ge, X. Wang, C. S. Zuo, J. J. Levitt, and C. Niu, "Dynamic default mode network across different brain states," *Scientific Reports*, vol. 7, p. 46088, 2017.

[111] S. Chiang, E. R. Vankov, H. J. Yeh, M. Guindani, M. Vannucci, Z. Haneef, and J. M. Stern, "Temporal and spectral characteristics of dynamic functional connectivity be-

tween resting-state networks reveal information beyond static connectivity," *PloS one*, vol. 13, no. 1, p. e0190220, 2018.

[112] X.-N. Zuo, C. Kelly, J. S. Adelstein, D. F. Klein, F. X. Castellanos, and M. P. Milham, "Reliable intrinsic connectivity networks: Test–retest evaluation using ICA and dual regression approach," *NeuroImage*, vol. 49, no. 3, pp. 2163–2177, 2010.

[113] V. G. van de Ven, E. Formisano, D. Prvulovic, C. H. Roeder, and D. E. Linden, "Functional connectivity as revealed by spatial independent component analysis of fMRI measurements during rest," *Human Brain Mapping*, vol. 22, no. 3, pp. 165–178, 2004.

[114] C. F. Beckmann, M. DeLuca, J. T. Devlin, and S. M. Smith, "Investigations into resting-state connectivity using independent component analysis," *Philosophical Transactions of the Royal Society B: Biological Sciences*, vol. 360, no. 1457, pp. 1001–1013, 2005.

[115] Y.-O. Li, T. Adali, W. Wang, and V. D. Calhoun, "Joint blind source separation by multiset canonical correlation analysis," *IEEE Transactions on Signal Processing*, vol. 57, no. 10, pp. 3918–3929, 2009.

[116] C. M. Crainiceanu, B. S. Caffo, S. Luo, V. M. Zipunnikov, and N. M. Punjabi, "Population value decomposition, a framework for the analysis of image populations," *Journal of the American Statistical Association*, vol. 106, no. 495, pp. 775–790, 2011.

[117] G. Zhou, A. Cichocki, Q. Zhao, and S. Xie, "Nonnegative matrix and tensor factorizations: An algorithmic perspective," *IEEE Signal Processing Magazine*, vol. 31, no. 3, pp. 54–65, 2014.

[118] T. H. Vu and V. Monga, "Fast low-rank shared dictionary learning for image classification," *IEEE Transactions on Image Processing*, vol. 26, no. 11, pp. 5160–5175, 2017.

[119] E. F. Lock, K. A. Hoadley, J. S. Marron, and A. B. Nobel, "Joint and individual variation explained (JIVE) for integrated analysis of multiple data types," *The Annals of Applied Statistics*, vol. 7, no. 1, p. 523, 2013.

[120] G. Zhou, A. Cichocki, Y. Zhang, and D. P. Mandic, "Group component analysis for multiblock data: Common and individual feature extraction," *IEEE Transactions on Neural Networks and Learning Systems*, vol. 27, no. 11, pp. 2426–2439, 2016.

[121] Z. Boukouvalas, Y. Levin-Schwartz, and T. Adalı, "Enhancing ICA performance by exploiting sparsity: Application to fMRI analysis," in *IEEE International Conference on Acoustics, Speech and Signal Processing (ICASSP)*, pp. 2532–2536, IEEE, 2017.

[122] Y.-O. Li, T. Adalı, and V. D. Calhoun, "Estimating the number of independent components for functional magnetic resonance imaging data," *Human Brain Mapping*, vol. 28, no. 11, pp. 1251–1266, 2007.

[123] W. Du, S. Ma, G.-S. Fu, V. D. Calhoun, and T. Adalı, "A novel approach for assessing reliability of ICA for fMRI analysis," in *International Conference on Acoustics, Speech and Signal Processing (ICASSP)*, pp. 2084–2088, IEEE, 2014.

[124] L. Sanfratello, J. M. Houck, and V. D. Calhoun, "Dynamic functional network connectivity in schizophrenia with magnetoencephalography and functional magnetic resonance imaging: Do different timescales tell a different story?," *Brain Connectivity*, vol. 9, no. 3, pp. 251–262, 2019.

[125] E. Allen, E. Damaraju, T. Eichele, L. Wu, and V. Calhoun, "EEG signatures of dynamic functional network connectivity states," *Brain Topography*, vol. 31, no. 1, pp. 101–116, 2018.

[126] M. Demirtaş, C. Tornador, C. Falcon, M. López-Solà, R. Hernández-Ribas, J. Pujol, J. M. Menchon, P. Ritter, N. Cardoner, C. Soriano-Mas, *et al.*, "Dynamic functional connectivity reveals altered variability in functional connectivity among patients with major depressive disorder," *Human Brain Mapping*, vol. 37, no. 8, pp. 2918–2930, 2016.

[127] Y. Du, G. D. Pearlson, D. Lin, J. Sui, J. Chen, M. Salman, C. A. Tamminga, E. I. Ivleva, J. A. Sweeney, M. S. Keshavan, *et al.*, "Identifying dynamic functional connectivity biomarkers using GIG-ICA: Application to schizophrenia, schizoaffective disorder, and psychotic bipolar disorder," *Human Brain Mapping*, vol. 38, no. 5, pp. 2683–2708, 2017.

[128] Y. Du, Z. Fu, and V. D. Calhoun, "Classification and prediction of brain disorders using functional connectivity: Promising but challenging," *Frontiers in Neuroscience*, vol. 12, 2018.

[129] M. S. Salman, Y. Du, D. Lin, Z. Fu, E. Damaraju, J. Sui, J. Chen, Q. Yu, A. R. Mayer, S. Posse, *et al.*, "Group ica for identifying biomarkers in schizophrenia:'adaptive'networks via spatially constrained ica show more sensitivity to group differences than spatio-temporal regression," *bioRxiv*, p. 429837, 2018.

[130] A. Zalesky, A. Fornito, L. Cocchi, L. L. Gollo, and M. Breakspear, "Time-resolved resting-state brain networks," *Proceedings of the National Academy of Sciences*, p. 201400181, 2014.

[131] K. P. Wylie and J. R. Tregellas, "The role of the insula in schizophrenia," *Schizophrenia research*, vol. 123, no. 2-3, pp. 93–104, 2010.

[132] R. W. Heinrichs and K. K. Zakzanis, "Neurocognitive deficit in schizophrenia: a quantitative review of the evidence.," *Neuropsychology*, vol. 12, no. 3, p. 426, 1998.

[133] S. Ma, T. Eichele, N. M. Correa, V. D. Calhoun, and T. Adalı, "Hierarchical and graphical analysis of fMRI network connectivity in healthy and schizophrenic groups," in *IEEE International Symposium on Biomedical Imaging: From Nano to Macro*, pp. 1031–1034, IEEE, 2011.

[134] L. Abel, S. Levin, and P. Holzman, "Abnormalities of smooth pursuit and saccadic control in schizophrenia and affective disorders," *Vision Research*, vol. 32, no. 6, pp. 1009–1014, 1992.

[135] S. Walther, K. Stegmayer, A. Federspiel, S. Bohlhalter, R. Wiest, and P. V. Viher, "Aberrant hyperconnectivity in the motor system at rest is linked to motor abnormalities in schizophrenia spectrum disorders," *Schizophrenia Bulletin*, vol. 43, no. 5, pp. 982–992, 2017.

[136] B. Ćurčić-Blake, L. van der Meer, G. H. Pijnenborg, A. S. David, and A. Aleman, "Insight and psychosis: Functional and anatomical brain connectivity and self-reflection in Schizophrenia," *Human Brain Mapping*, vol. 36, no. 12, pp. 4859–4868, 2015.

[137] T. Nekovarova, I. Fajnerova, J. Horacek, and F. Spaniel, "Bridging disparate symptoms of schizophrenia: a triple network dysfunction theory," *Frontiers in behavioral neuroscience*, vol. 8, p. 171, 2014.

[138] W. Guo, F. Liu, J. Chen, R. Wu, L. Li, Z. Zhang, H. Chen, and J. Zhao, "Hyperactivity of the default-mode network in first-episode, drug-naive schizophrenia at rest revealed by family-based case–control and traditional case–control designs," *Medicine*, vol. 96, no. 13, 2017.

[139] P. Fusar-Poli, O. Howes, P. Allen, M. Broome, I. Valli, M. Asselin, A. Montgomery, P. Grasby, and P. McGuire, "Abnormal prefrontal activation directly related to presynaptic striatal dopamine dysfunction in people at clinical high risk for psychosis," *Molecular psychiatry*, vol. 16, no. 1, p. 67, 2011.

[140] C. Zhou, M. Yu, X. Tang, X. Wang, X. Zhang, X. Zhang, and J. Chen, "Convergent and divergent altered patterns of default mode network in deficit and non-deficit schizophrenia," *Progress in Neuro-Psychopharmacology and Biological Psychiatry*, vol. 89, pp. 427–434, 2019.

[141] S. Whitfield-Gabrieli, H. W. Thermenos, S. Milanovic, M. T. Tsuang, S. V. Faraone, R. W. McCarley, M. E. Shenton, A. I. Green, A. Nieto-Castanon, P. LaViolette, *et al.*, "Hyperactivity and hyperconnectivity of the default network in schizophrenia and in first-degree relatives of persons with schizophrenia," *Proceedings of the National Academy of Sciences*, pp. pnas–0809141106, 2009.

[142] A. G. Garrity, G. D. Pearlson, K. McKiernan, D. Lloyd, K. A. Kiehl, and V. D. Calhoun, "Aberrant "default mode" functional connectivity in schizophrenia," *American Journal of Psychiatry*, vol. 164, no. 3, pp. 450–457, 2007.

[143] J. M. Houck, M. S. Çetin, A. R. Mayer, J. R. Bustillo, J. Stephen, C. Aine, J. Cañive, N. Perrone-Bizzozero, R. J. Thoma, M. J. Brookes, *et al.*, "Magnetoencephalographic and functional MRI connectomics in schizophrenia via intra-and inter-network connectivity," *NeuroImage*, vol. 145, pp. 96–106, 2017.

[144] M. Liljeström, C. Stevenson, J. Kujala, and R. Salmelin, "Task-and stimulus-related cortical networks in language production: Exploring similarity of MEG-and fMRI-derived functional connectivity," *NeuroImage*, vol. 120, pp. 75–87, 2015.

[145] T. Adalı, Y. Levin-Schwartz, and V. D. Calhoun, "Multimodal data fusion using source separation: Two effective models based on ICA and IVA and their properties," *Proceedings of the IEEE*, vol. 103, no. 9, pp. 1478–1493, 2015.

[146] C. Arndt and O. Loffeld, "Information gained by data fusion," in *Vision Systems: Sensors, Sensor Systems, and Components*, vol. 2784, pp. 32–40, International Society for Optics and Photonics, 1996.

[147] D. L. Hall and J. Llinas, "An introduction to multisensor data fusion," *Proceedings of the IEEE*, vol. 85, no. 1, pp. 6–23, 1997.

[148] Q. Long, S. Bhinge, V. D. Calhoun, and T. Adalı, "Independent vector analysis for common subspace analysis: Application to multi-subject fMRI data yields meaningful subgroups of schizophrenia," *Under Review*.